Computational Modeling of Primary Blast Effects on the Human Brain

by

Michelle K. Nyein

S.B., Chemistry, Massachusetts Institute of Technology (2004)
J.D., Harvard University (2007)
S.M., Aeronautics and Astronautics, Massachusetts Institute of Technology (2010)

Submitted to the Department of Aeronautics and Astronautics
in partial fulfillment of the requirements for the degree of

Doctor of Philosophy in Aeronautics and Astronautics

at the

MASSACHUSETTS INSTITUTE OF TECHNOLOGY

June 2013

Author . . . .
Department of Aeronautics and Astronautics
March 4, 2013

Certified by. . . . .
Raúl Radovitzky
Professor of Aeronautics and Astronautics
Thesis Supervisor

Certified by. . . . .
Dava J. Newman
Professor of Aeronautics and Astronautics

Certified by. . . . .
Laurence R. Young
Apollo Program Professor of Aeronautics and Astronautics

Certified by. . . . .
Simona Socrate
Principal Research Scientist, Institute for Soldier Nanotechnologies

Certified by. . . . .
David F. Moore
Attending Neurologist, Baylor University Medical Center

Accepted by . . . .
Eytan H. Modiano
Professor of Aeronautics and Astronautics
Chair, Committee on Graduate Students

Computational Modeling of Primary Blast Effects on the Human Brain

by

Michelle K. Nyein

Submitted to the Department of Aeronautics and Astronautics
on March 4, 2013, in partial fulfillment of the
requirements for the degree of
Doctor of Philosophy in Aeronautics and Astronautics

Abstract

Since the beginning of the military conflicts in Iraq and Afghanistan, there have been over 250,000 diagnoses of traumatic brain injury (TBI) in the U.S. military, with the majority of incidents caused by improvised explosive devices (IEDs). Despite the urgent need to understand blast-induced TBI in order to devise strategies for protection and treatment, much remains unknown about the mechanism of injury, the effects of personal protective equipment (PPE) such as helmets, and injury metrics and thresholds. In order to help address these gaps, this thesis has four objectives: 1) to present a comprehensive computational framework for investigating the mechanical response of the human head to blasts that includes blast-structure interaction codes, a detailed, three-dimensional model of a human head generated from high-resolution medical imaging data, and an experimentally-validated constitutive model for brain tissue; 2) to validate the framework against a broad range of experiments, including free-field blast tests involving physical human head surrogates and laboratory-scale shock tube tests involving animals and human cadavers; 3) to use the computational framework to investigate the effect of PPE on the propagation of stress waves within the brain following blast events and evaluate their blast protection performance; and 4) to develop interspecies scaling laws for the blast response of the brain that would allow translation of injury metrics from animals to humans.

Thesis Supervisor: Raúl Radovitzky
Professor of Aeronautics and Astronautics

Committee Member: Dava J. Newman
Professor of Aeronautics and Astronautics

Committee Member: Laurence R. Young
Apollo Program Professor of Aeronautics and Astronautics

Committee Member: Simona Socrate
Principal Research Scientist, Institute for Soldier Nanotechnologies

Committee Member: David F. Moore
Attending Neurologist, Baylor University Medical Center

Acknowledgments

providing experimental data for our validation efforts.

I would like to express my appreciation to Professor John Joannopoulos for participating in my thesis proposal defense and providing financial support through ISN, and to Professor Wes Harris for allowing me to take Unified Engineering when I was in my third year of law school.

I would also like to thank the wonderful Aero-Astro administrators. I am truly grateful to Barbara Lechner, Beth Marois, and Marie Stuppard for their assistance throughout my graduate career.

Of course, my grad school experience would not have been the same without the members, past and present, of the RR Group. Special thanks to Dr. Antoine Jerusalem for teaching me how to do pretty much everything when I first started grad school. Also, I would be remiss if I did not thank Li Yu, Amira guru and designer extraordinaire, for developing the computational pig head model, and Amanda Jason, Ansys expert, for developing the face shield model. I would also like to acknowledge Lei Qiao, Andy Seagraves, Mike Tupek, and Brandon Talamini for their friendship and support through many, many years of navigating through classes, quals, research, paperwork, and information security trainings together.

Thank you also to Bob and Jan Randolph for being such wonderful housemasters and to everyone at Bexley for providing a unique, colorful home for me and David for four years.

Deepest and most heartfelt thanks to my amazing husband, Dr. David Carpenter, who has been by my side through every step of my journey through law school and grad school. He has brought so much joy and love into my life, and we have experienced such wonderful adventures over our 9.5 years together – I cannot wait to see what the future holds in store for us. Thanks also to our cat, Truffle, for providing much-needed amusement and fluffiness over the last 4.5 years.

Contents

List of Figures

List of Tables

Chapter 1

Introduction

Since Operation Enduring Freedom (OEF) began in Afghanistan in October 2001 and Operation Iraqi Freedom (OIF) began in Iraq in May 2003 (subsequently becoming Operation New Dawn (OND) in September 2010), U.S. service members have been widely exposed to explosive munitions such as improvised explosive devices (IEDs), and blast-induced traumatic brain injury (bTBI) has become a significant cause of death and disability among warfighters. According to the U.S. Department of Defense (DoD), there have been 262,065 medical diagnoses of TBI in the U.S. military from 2000 to the third quarter of 2012, with 94.8% of the cases involving non-penetrating TBI [82]. The threat to U.S. service members has steadily increased over the years, with the annual number of TBI diagnoses rising from 12,470 in 2002 to 33,149 in 2011 [82]. Assuming that most of the TBI diagnoses in 2011 resulted from combat-related incidents in Iraq or Afghanistan, and given that the peak number of U.S. troops reported deployed to Iraq or Afghanistan that year was 203,800, we can estimate the incidence of blast-induced TBI in 2011 to be 16.3%. This is consistent with a wide number of studies on OEF/OIF veterans that have reported overall TBI incidences of 12-23% [78, 125, 58, 116]. Among those who have been wounded in theater, the proportion that has suffered a TBI is predictably higher, with reported ranges of 30-80% [129, 26]. Due to this high incidence among U.S. service members deployed to Iraq and Afghanistan, TBI has been labeled the signature injury of OEF and OIF/OND [58].

For active duty military personnel in war zones, blasts are the primary cause of TBI [122]. 68% of the OEF/OIF soldiers at Walter Reed Army Medical Center (WRAMC) who screened positive for TBI had been injured by a blast [135], and data collected from March to September 2004 from Navy-Marine Corps medical facilities in Iraq found that IEDs were responsible for 62% of combat-related TBIs [46]. Another study of 2,898 TBI hospitalizations of U.S. Army soldiers deployed to Iraq and Afghanistan from September 2001 to September 2007 found that 62.7% of the TBIs were caused by explosions [139].

One reason blasts have become such a significant cause of military-related TBI is that the conflicts in Iraq and Afghanistan involve battling insurgents who favor cheap, easily concealed explosive weapons capable of producing a large number of human casualties. As a result, approximately 60% of total combat casualties [73] and 67% of Army war zone evacuations [134] have been attributed to explosive blasts. The IED in particular has become the most common explosive weapon [73], accounting for about 40% of all casualties [122]. In one U.S. Army Brigade Combat Team in Iraq, 87.4% of casualties were caused by explosions, with 77.7% of all casualties caused by IEDs [16]. IEDs can be manufactured from materials ranging from 155 mm artillery shells to plastic explosives to barrels of gasoline [4]; they have evolved from relatively crude devices detonated by simple mechanisms to sophisticated devices capable of penetrating the armor of an M-1 Abrams tank [122]. Exposure to these blasts often leads to head and neck injuries. For example, 97% of the injuries in one Marine unit in Iraq were due to explosions (65% to IEDs), with 53% of those injuries involving the head and neck [121], and a study of 4,831 patients at a U.S. Army echelon II medical facility in Iraq between October 1, 2003, and June 30, 2004, found that 88% of the patients treated had been injured by IEDs or mortars, with up to 47% of those injuries involving the head [89]. One study of 4,122 soldiers in a U.S. Army Brigade Combat Team deployed to Iraq for 15 months during "The Surge" phase of OIF found that 36.2% of injuries were to the head or neck, compared to 21% in World War II, 21.4% in Korea, and 16.0% in Vietnam [16]. That study also found that 95.9% of the head/neck injuries were caused by IEDs [16]. It is likely that a significant number

of the head injuries caused by explosions included TBIs. One study of 4,623 combat explosion episodes in Iraq from March 2004 to December 2007 found that mild TBI (mTBI) was the most frequent type of injury, occurring 10.8% of the time [42].

Blast-related TBI has also gained visibility because U.S. service members are now able to survive blasts that previously would have been fatal due to advances in military medicine and personal protective equipment (PPE). In the current conflicts, the survival rates are dramatically higher than in previous conflicts. While 30% of wounded U.S. soldiers died in World War II and 24% of wounded U.S. soldiers died in the Vietnam conflict, only about 10% of wounded U.S. soldiers have died in Afghanistan and Iraq [49]. In one U.S. Army Brigade Combat Team that was deployed during OIF, the case fatality ratio was only 7.7% [16]. The high survival rate can be attributed in part to significant advances in military medicine, including deployment of leaner, more mobile surgical teams far forward on the battlefield and rapid medical evacuation from combat zones — the average time from battlefield to arrival in the United States is now less than 4 days, compared to 45 days during the Vietnam conflict [49]. There have also been important advances in TBI treatment in theater, including early decompressive craniectomy, neurocritical care, cerebral angiography, transcranial Doppler, hypertonic saline, and TBI clinical management guidelines [73]. The high survival rate can also be attributed in part to significant advances in the performance of PPE [97]. However, the improved protective gear does not necessarily prevent blast-related TBI; PPE is designed to protect against ballistic and other impact loads, not blasts. Blast protection has not been a primary objective in the design of PPE, and any secondary blast protection provided has been fortuitous; the low incidence of blast lung injury nowadays, for example, suggests that Kevlar vests are effective in preventing those types of injuries. The effect of the Advanced Combat Helmet (ACH), which is reported to be worn by 69-79% of TBI patients at the time of injury [139, 46], is unknown.

Given its prevalence among U.S. service members in recent years, blast-induced TBI has become a major concern of the U.S. government, and a number of initiatives have been launched to study and combat it. In 2006, a DoD directive established the

Joint IED Defeat Organization (JIEDDO), which focuses on reducing the effects of IED detonations, interrupting the insurgent IED network, and training U.S. troops in blast mitigation strategies. Also in the 2006, the DoD Blast Injury Research Program was established pursuant to a Congressional mandate to coordinate medical research on the prevention, mitigation, and treatment of blast injuries. In order to assess the state of the art in computational modeling of blast-induced TBI and to integrate DoD research efforts, the DoD Blast Injury Research Program established the DoD Brain Injury Computational Modeling Expert Panel. Overall, from fiscal year 2007 to fiscal year 2010, DoD activities for the treatment and research of psychological health and traumatic brain injury received more than $2.7 billion [21]. Blast injuries have also attracted international attention; Canada has assembled a Canadian Forces Health Services Advisory Panel on Management of Mild Traumatic Brain Injury in Military Operational Settings, and in 2011 the North Atlantic Treaty Organization (NATO) held a symposium titled "A Survey of Blast Injury Across the Full Landscape of Military Science."

It is therefore clear that blast-induced TBI has become one of the leading challenges in the battlefield for the U.S. military. Despite the importance of understanding bTBI, there is much that remains unknown about the mechanism and thresholds of injury and therefore about how to develop strategies for protection and treatment. For example, it is uncertain to what extent blast-induced TBI shares characteristics with closed head and penetrating TBI. One clinical study of 56 U.S. service members who sustained a mild TBI during OEF/OIF found that blast and non-blast groups performed similarly on neurocognitive measures, although those in the blast group were somewhat more likely to suffer from depression and stress [69]. However, other studies suggest that bTBI may have unique features; for example, diffuse axonal injury (DAI) following blast exposure may be distinct from DAI following concussive impact [80]. The mechanism of bTBI also remains in dispute, with proposed mechanisms including direct transmission of stress waves into the intracranial cavity [87], rotational acceleration of the head, skull flexure [88], and a vascular mechanism [23].

In this thesis, we aim to begin addressing some of these gaps through computa-

tional modeling of the blast response of the human brain. To begin, we first provide background on bTBI and on existing work in the literature on computational modeling of bTBI.

1.1 Traumatic Brain Injury

1.1.1 Definition

In 1995, the Centers for Disease Control and Prevention (CDC) published Guidelines for Surveillance of Central Nervous System Injury, which defined TBI in terms of ICD-9-CM (International Classification of Diseases, Ninth Revision, Clinical Modification) diagnostic codes [128]. To summarize, TBI was defined as an occurrence of head injury that is associated with decreased level of consciousness, amnesia, other neurological or neuropsychological abnormalities, skull fracture, diagnosed intracranial lesions, or death [127]. TBIs may be classified by severity as mild, moderate, or severe. The American Congress of Rehabilitation Medicine has defined mild TBI (mTBI) as a head injury resulting in at least one of the following: (1) loss of consciousness (LOC) for approximately 30 minutes or less; (2) post-traumatic amnesia (PTA) for less than 24 hours; (3) any alteration in mental state at the time of the accident; and (4) focal neurological deficit(s) that may or may not be transient, with a Glasgow Coma Scale (GCS) score of 13 or greater 30 minutes after injury [85, 90]. Moderate TBI is typically associated with a presenting GCS score of 9-13, and severe TBI with a GCS score of 8 or lower [73]. A new classification specific to blast-related TBI has been proposed, in which a mild bTBI would be characterized by LOC for less than 1 hour and PTA for less than 24 hours following exposure to an explosive blast, a moderate bTBI would be characterized by LOC for 1-24 hours and PTA for 1-7 days, and severe bTBI would be characterized by LOC for more than 24 hours and PTA for more than 7 days [73].

The vast majority of TBIs in the military population are mild. In the U.S. military, 76.4% of the TBIs diagnosed since 2000 have been mild, with 17.4% moderate and

1% severe, as shown in Figure 1-1 [82]. We therefore focus on mild TBI in this thesis.
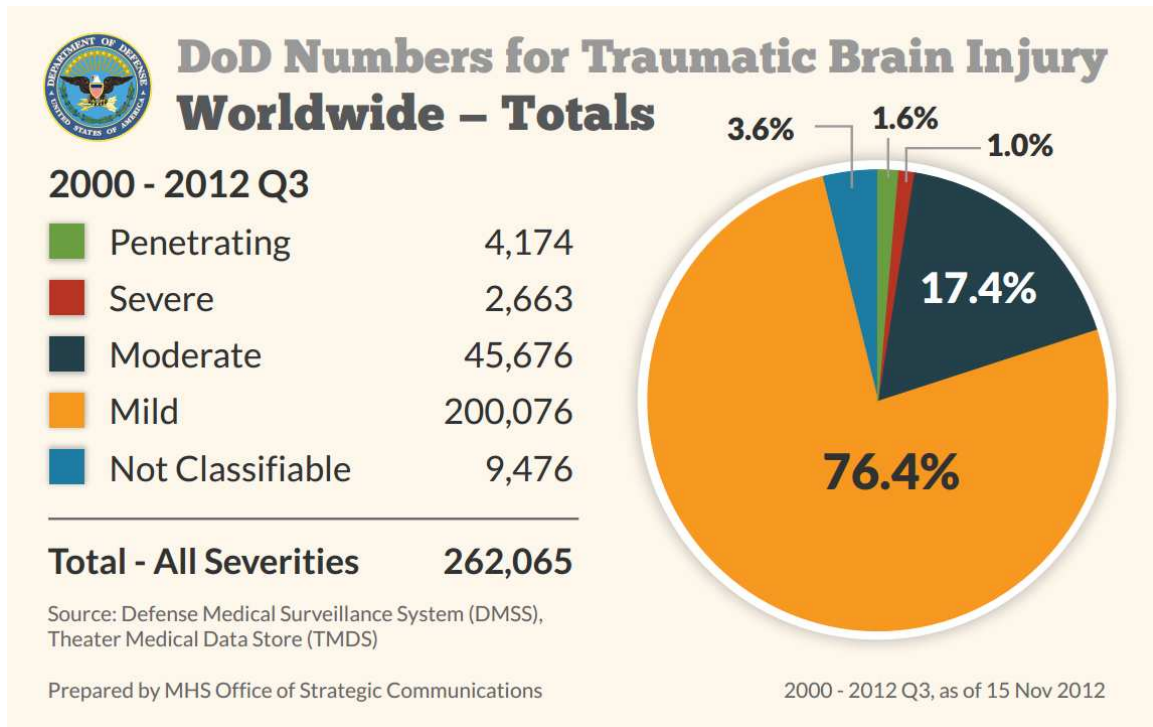
Figure 1-1: Department of Defense Numbers for Traumatic Brain Injury (from 2000 to November 2012). Source: Defense and Veterans Brain Injury Center (http://www.dvbic.org/dod-worldwide-numbers-tbi)

1.1.2 Screening, Symptoms, and Treatment

Screening

Accurate screening for mild blast-induced TBI is challenging because often there are no visible signs of abnormality on computed tomography (CT) or magnetic resonance (MR) images [97]. However, technologies such as diffusion tensor imaging (DTI), positron emission tomography (PET), magnetoencephalography (MEG), and transcranial Doppler (TCD) may be useful in identifying cases of blast-induced TBI. For example, in a recent study of 63 U.S. service members who had a clinical diagnosis of mild blast-induced TBI but no detectable injury on CT images, DTI scanning within 90 days of injury found abnormalities consistent with traumatic axonal injury in two or more brain regions in 18 subjects [77]. The imaging abnormalities were persistent;

in follow-up scans conducted on 47 of the subjects 6-12 months after enrollment, 11 out of 12 subjects who had abnormalities in the original scans were found to still exhibit abnormalities. In the initial scans, the abnormalities observed were consistent with axonal injury, cellular inflammatory response, and cerebral edema; in the follow-up scans, however, the abnormalities observed were consistent with persistent axonal injury and resolution of the cellular inflammation and edema. These results demonstrate that DTI can detect axonal injury in some blast-induced mTBI patients. Another study of 25 OEF/OIF veterans who had experienced a blast-induced mTBI an average of 2-5 years prior to the study and 33 veterans without mTBI found that blast-induced mTBI was associated with a diffuse, global pattern of reduced white matter integrity [31]. The data suggested that the long-term effects of blast-induced mTBI on white matter integrity consist of subtle, widespread disruptions rather than damage to specific tracts that are consistent across individuals. They also found that individuals with more than one blast mTBI tended to have a larger number of low fractional anisotropy voxels than individuals with a single blast mTBI, but there was no independent effect due to civilian, non-blast mTBI; this suggests that the effects observed are unique to blast-induced mTBI. The diffuse nature of the effects of blast exposure on white matter may provide one explanation why a separate study of 37 OEF/OIF veterans who had sustained a blast-induced mild or moderate TBI while serving in Iraq or Afghanistan found that DTI scans an average of 871.5 days post-injury did not reveal any differences between the TBI group and a control group [71].

In addition to DTI, imaging techniques such as PET scans, MEG, and TCD may be useful in assessing various complications of blast-induced mTBI, such as persistent postconcussive syndrome (PCS). For example, a study that conducted PET scans on 12 OIF veterans who reported one or more blast exposures and met the criteria for mTBI and PCS found that the veterans exhibited decreased cerebral metabolic rate of glucose in the cerebellum, vermis, pons, and medial temporal lobe, and that the veterans experienced subtle impairments in complex information processing, with mild reductions in verbal fluency, cognitive processing speed, attention, and working

memory [100]. The findings suggest that regional brain hypometabolism may constitute a neurobiological substrate for PCS [100]. Another study demonstrated the ability to use MEG to detect abnormalities in TBI patients and correlate the abnormalities with PCS [43]. Studying a population of 45 mTBI and 10 moderate TBI patients with ongoing PCS an average of 8.2 months post-injury, they were able to detect abnormal low-frequency magnetic activity in 87% of the mTBI patients and 100% of the moderate TBI patients [43]. Among the blast-induced mTBI patients, they detected MEG abnormalities in 96% of the patients. They also found that the number of regions generating abnormal slow-waves correlated with PCS scores in the TBI patients. Another technique, transcranial Doppler ultrasound, may be used to detect other complications of combat-related TBI, such as vasospasm and intracranial hypertension [7].

An alternative and complementary approach to screening for injury after blast exposure is to equip service members with dosimeters that could indicate when a service member has been exposed to a dangerous level of blast overpressure. For example, the U.S. military has begun equipping soldiers with helmet-mounted blast dosimeters that collect acceleration and pressure data. Another alternative is a colorimetric sensor developed by Cullen et al. [29]. The photonic crystal sensor, which changes color following a tunable level of blast exposure due to changes in nanostructure, is small, lightweight, durable, and requires no power; it appears as an array of small colored stickers that may be affixed to uniforms or helmets. An experimental study involving rats demonstrated the ability of the sensors to change colors following exposure to 120-140 kPa blasts, which were sub-lethal and associated with subtle brain pathologies, including neuronal degeneration and reactive astrocytosis.

Symptoms

Common symptoms of TBI include a variety of cognitive, behavioral, and physical/somatic changes. Cognitive changes may include disturbances in attention, memory, language, or executive functioning, such as poor planning, organizing, or sequencing, and/or impaired judgment and impulse control [97, 67, 108]. Behavioral changes

may include mood changes, depression, anxiety, impulsiveness, emotional outbursts, irritability, or inappropriate laughter [97, 63]. Physical or somatic symptoms may include headaches, fatigue, sleep disturbances, dizziness, problems with motor skills, and sensitivity to light and noise [97, 63]. In addition, 12-51% of TBI patients develop psychiatric disorders, such as major depression, anxiety disorders, and psychosis [52, 108], and up to 50% of TBI patients suffer from impaired neuroendocrine function, particularly growth hormone deficiency [63]. For blast-induced TBI patients in particular, depending on the severity of injury, common symptoms include subdural hematoma, headache, blurring of vision, transient deafness, and psychoneuroses [70]. Blast-injured patients are also more likely than other TBI patients to report neurological disorders such as insomnia, impaired concentration, memory loss, and hypervigilance [70, 134].

Most patients with mild TBI recover fully in 4-12 weeks [63, 2], although mTBI patients with more severe injuries, such as those who experienced LOC lasting more than 10 minutes or PTA lasting more than 4-6 hours, may require months to years to recuperate [2]. In addition, 15-35% of mTBI patients develop PCS, experiencing persistent cognitive, behavioral, and/or somatic symptoms [116, 2, 56, 127]. It is not known why some patients develop PCS, although some explanations have included high levels of preexisting emotional stress, severe pain, and genetic predisposition to poor TBI outcome [2, 63]. One study found that the strongest symptoms that predicted PCS included anxiety and noise sensitivity [36]. Repeated exposure to blasts has also been found to lead to PCS and generally worsen TBI symptoms [1, 121]. One study of 126 veterans with a history of blast-induced mTBI found that of the 63% of veterans who had residual impairments on neurological or neuropsychological examinations, 91% had reported multiple episodes of loss of consciousness [114].

Studies of OEF/OIF veterans who have sustained a blast-induced TBI have found varying long-term outcomes. One study that surveyed 3,098 members of the Florida National Guard, 1,443 of whom had been deployed, found that combat-related TBI was associated with depression, anxiety, post-traumatic stress disorder (PTSD), and PCS, with the associations increasing with multiple TBIs [130]. Another study that

compared 37 OEF/OIF veterans who had sustained a combat-related bTBI with 15 veterans who had not sustained a TBI found that members of the TBI group were more likely to experience PCS, PTSD, distress, and depression, but there were no group differences in physical or mental functioning, aside from verbal memory being less efficient in the TBI group [71]. A separate study that conducted structured interviews with 104 OEF/OIF veterans, 18 of whom had a blast-induced mild TBI and did not have a co-morbid psychiatric disorder, found only subtle cognitive impairment in the late stage of injury [91]. It is not clear if the long-term clinical symptoms of blast-induced mTBI are different from those of penetrating or closed-head TBI. One study of 56 U.S. service members who sustained an mTBI during OEF/OIF found that blast and non-blast groups performed similarly on neuropsychological evaluations given an average of 4.4 months post injury, although those in the blast group were somewhat more likely to experience depression and stress [69]. Similarly, another clinical study of 298 blast and 92 non-blast mTBI patients found that the mechanism of injury did not account for a significant amount of variance in PCS reporting [14].

Many mild TBI symptoms overlap with PTSD symptoms, and a number of patients suffer from both disorders [97]. Overlapping symptoms include cognitive problems such as impaired learning, forgetfulness, attention and concentration difficulties, slower processing speed, a sense of being overwhelmed with once simple tasks, and changes in personality such as impulsiveness, reduced insight, rigid thinking, and reduced motivation [63]. Studies have shown that PTSD is strongly associated with mild TBI; one survey of soldiers from two U.S. Army combat infantry brigades 3-4 months after returning from a year-long deployment in Iraq found that 32.6% of soldiers with mild TBI met the criteria for PTSD [58], and another survey of OIF/OEF veterans from all branches of the military found that 39.6% of respondents with mTBI had PTSD [116]. Another study found that the highest rates of PTSD (33-39%) are reported among OEF/OIF soldiers with a history of mTBI [17]. It has been suggested that the strong association between mild TBI and PTSD can be explained by the fact that the life-threatening, traumatic events that lead to combat-related mTBI are also likely to result in PTSD, or by the possibility that symptoms associated with PTSD

may be a manifestation of brain injury [58, 116]. For example, it has been suggested that the same brain regions that are commonly affected by TBI are also involved in PTSD and that increased risk of PTSD may be attributed to TBI-related neuronal damage that compromises the neural circuitry critical for regulation of fear following trauma [17]. In addition, it has been suggested that PTSD can modify the effects of mTBI [58, 116], and in particular, exacerbate cognitive symptoms of mTBI [63]. Studies have also found that PTSD is strongly associated with persistent postconcussive symptoms following mTBI. In the Hoge et al. study, it was found that while soldiers with mild TBI were significantly more likely to report poor general health, missed workdays, medical visits, and a high number of somatic and postconcussive symptoms, after adjustment for PTSD and depression, the association between mTBI and poor physical health outcomes disappeared, except for headache; the poor physical health outcomes occurred almost exclusively in soldiers with PTSD, and among those soldiers with PTSD, the proportion with poor physical health symptoms did not significantly differ according to type of injury [58]. In the Schneiderman et al. study, it was found that 35% of respondents with mild TBI reported persistent postconcussive symptoms, but 66% of respondents with both mild TBI and PTSD reported persistent postconcussive symptoms [116]. The association between mTBI, PTSD, and physical health problems remains under investigation, but one thing is clear — soldiers who reported mTBI events were at very high risk for physical and mental health problems [58, 116].

Treatment

Many of the symptoms of TBI are currently treated by pharmaceuticals. For example, stimulants such as methylphenidate or dextroamphetamine are commonly used to treat problems with attention or information processing, selective serotonin-reuptake inhibitor antidepressants are sometimes prescribed for irritability or angry outbursts, and valproate is often prescribed for migraines and behavioral symptoms [97]. However, there is still no broad-based cure for TBI, in large part due to the heterogeneous nature of TBI. Similarly, no single biomarker of TBI has yet been identified, although

it has been suggested that a combination of markers, such as S-100β, neuron specific enolase, glial fibrillary acid protein, myelin basic protein, αII-spectrin breakdown products, N-methyl-D-aspartate (NMDA) receptor fragments, and anti-inflammatory cytokines could effectively detect TBI and predict outcomes [120]. One study of pigs exposed to blasts found that levels of serum neurofilament heavy chain (NF-H) increased in a unique, rapid manner following blast injury, peaking at 6 hours post-injury in animals with poor clinical and pathological outcomes, suggesting that serum NF-H levels could be a useful diagnostic tool [55].

1.1.3 Pathophysiology

Although the primary focus of this thesis is the mechanical response, rather than the biological response, of the human head to blasts, for completeness we summarize current research on the pathophysiology of traumatic brain injury. While the majority of this research has been conducted on civilian populations and has therefore focused on impact-related and penetrating TBI, the findings may nevertheless provide insight into the course of blast-induced TBI.

Overall, TBI comprises two phases of injury: primary and secondary. Primary injury encompasses direct, unavoidable injury that occurs during the initial insult, including contusions, lacerations, hemorrhages, and axonal shearing. Secondary injury follows from the primary injury and occurs through biochemical processes in the hours and days following the initial insult.

Primary Injury

A mechanical insult to the head may cause blood vessels to rupture, leading to contusions, hemorrhages, and hematomas. Cerebral contusions, or bruises, are caused when capillaries bleed into the brain tissue. They are commonly located within the gray matter or at the gray-white matter interface, particularly in the frontal and temporal lobes due to their proximity to bony protuberances on the inside surface of the skull [67, 121, 101, 63]. The contusions can directly disrupt function in cortical

30

and sub-cortical regions [67], contributing to local necrotic and apoptotic neuronal deaths [101]. Some studies have linked focal cortical contusions in the anterior frontal and temporal lobes to impairments in executive functioning, working memory, memory encoding and retrieval, higher order attenuation, and behavior modulation, and contusions in the posterior temporal lobe to language disorders [101]. Rupture of blood vessels can also lead to hemorrhages, such as subarachnoid hemorrhage, which involves bleeding in the space between the arachnoid membrane and the pia mater. Presence of subarachnoid hemorrhage typically indicates a more severe injury and often heralds acute severe cerebral edema and hyperemia, as well as delayed vasospasm [73]. In addition, contusions and hemorrhages can lead to hematomas, or collections of blood outside blood vessels. Subdural hematoma, for example, is caused by bleeding from the veins that run between the dura mater and the brain, and epidural hematoma is caused by bleeding between the dura mater and the skull. Hematomas can be dangerous because they can compress the brain and raise intracranial pressure, leading to cerebral ischemia, which contributes to about 90% of deaths after closed head injuries [132].

A mechanical insult to the head can also cause DAI, in which axons are damaged by shearing forces, leading to degeneration of some axons' distal projections and diffuse loss of synaptic terminals [98, 97]. Occurring in all severities of TBI, it has been increasingly recognized as central to a patient's outcome, causing at least one-third of the poor outcomes of TBI [98]. It can commonly be found in the gray-white matter junction, internal capsule, deep gray matter, rostral brainstem, and corpus callosum [121, 93, 67]. Damage to these regions is associated with high mortality because the sites serve as neural relay stations and as centers for vital functions; for example, trauma to the brainstem occurs in 70% of head injuries with survival times of less than 48 hours [5]. Loss of neural connections may lead to many of the symptoms associated with brain injuries [97], with deeper lesions and involvement of the corpus callosum or upper brain stem corresponding to more severe injuries and greater disability [101]. One study demonstrated that moderate and severe TBI subjects had reduced white matter integrity in 13 distinct regions, including the corpus callosum and corona

radiata, and mild TBI subjects had reduced white matter integrity in 3 regions — the superior longitudinal fasciculus, sagittal stratum, and corticospinal tract [67].

Secondary Injury

Secondary injury mechanisms are the physiological responses to primary injury [73]. Following the initial insult, primary injuries can trigger secondary injury through a number of mechanisms, including excitotoxicity, oxidative stress, and inflammation.

Excitotoxicity, for example, can lead to neuronal and axonal death. Primary injury typically leads to excessive extracellular concentrations of the excitatory neurotransmitters (and excitotoxins) glutamate and aspartate [98, 132, 63]. Animal studies have demonstrated significant increases in extracellular glutamate and aspartate adjacent to the trauma site, with the increases being proportional to the severity of the injury [44]. The glutamate and aspartate act on NMDA receptors to alter cell wall permeability, allowing increases in intracellular calcium and sodium [132, 98]. The excess calcium and sodium activate cysteine proteases such as calpains and caspases that can degrade a variety of proteins, including cytoskeletal proteins, membrane receptors, and signal transduction enzymes [133]; this leads to necrotic and apoptotic cell death [98, 101]. In axons, for example, where mechanical forces associated with injury can also trigger focal alterations in axolemmal permeability that allow influx of calcium [101], the calpains and caspases degrade proteins responsible for shape and transport, ultimately leading to axonal disconnection [98, 132]. In humans, this process can take several hours or days post injury [101]. Following axonal damage and disconnection, the axon undergoes Wallerian degeneration, a several month process in which the portion of the axon separated from the neuron's nucleus disintegrates [101]. Some data suggest that this sets the stage for intact nerve fibers to sprout, leading to recovery of synaptic input [101], while other data suggest that glial scars may form in the spaces left by degenerating axons, obliterating pathways for axonal growth or actively inhibiting axonal growth. Preliminary studies have shown that the neuronal cell bodies linked to traumatically damaged axons do not progress to rapid cell death, but rather undergo perturbation of neuronal protein translation that

persists for several days and is followed by cellular recovery [101].

Excitotoxicity can also lead to oxidative stress, a secondary injury mechanism that involves reactive oxygen species inducing oxidative damage [98, 33]. For example, excessive NMDA receptor activity can increase production of nitric oxide, while excess intracellular calcium can increase production of superoxide; the nitric oxide and superoxide react to produce peroxynitrite, a highly reactive oxidant that can produce nitration of amino acid aromatic rings, lipid peroxidation, and DNA fragmentation, all of which rapidly lead to cell death [98]. In general, reactive oxygen species can cause considerable damage to proteins, lipids, and DNA through peroxidation of cellular and vascular structures, DNA damage, protein oxidation, lipid/protein nitration, and inhibition of the mitochondrial electron transport chain, leading to initiation of necrotic and apoptotic cell death cascades [33, 136]. One rat study found levels of oxidative stress to be increased within a few hours of insult, with a return to normal levels by 5 days post injury [33].

Additional secondary responses include neuroinflammation, reduced cerebral metabolic and energetic states, and cholinergic deficits. For example, primary brain injury can trigger cellular and humoral inflammatory responses that can last hours to days [132, 1]. Following primary injury, concentrations of pro-inflammatory cytokines such as interleukin-6 are increased [132, 1], and microglia, the resident immune cells of the central nervous system, are activated, releasing various chemokines and cytokines that can act as pro-inflammatory factors [1]. These processes act to eliminate injured and adjacent tissue, replacing them with newly synthesized scar tissue [136]. In addition to inflammation, primary insults can lead to a reduction in cerebral metabolic and energetic states. TBI has been found to lead to a sharp reduction in intracellular free magnesium [44]. Since intracellular magnesium regulates many processes responsible for cellular metabolism and bioenergetics, cerebral metabolic and energetic states are frequently reduced after TBI, with degree of metabolic failure related to severity of the primary insult [136]. Some researchers have found a correlation between reduced cerebral metabolic rate in the brainstem, thalamus, and cerebellum and level of consciousness in patients recovering from TBI [101]. Primary insults can also lead to a

decrease in acetylcholine, a neurotransmitter considered critical for arousal and attention, declarative memory, and executive function; cholinergic deficit is thought to be the neurochemical basis for cognitive deficits following TBI [63].

A number of secondary outcomes are particularly common sequelae of blast-induced TBI. For example, severe bTBI frequently results in vasogenic or cytotoxic cerebral edema [1]. Cerebral edema, or swelling of the brain due to water imbalance, is dangerous because it can rapidly develop and lead to intracranial hypertension, hypoxia, ischemia, and necrotic and apoptotic neuronal cell death [1, 75, 4]. Vasogenic edema, which is seen primarily in cerebral white matter, occurs rapidly as the inflammatory response breaks down the blood-brain barrier and allows for transfer of ions and proteins from the intravascular to the extracellular brain compartments [4, 1, 136]. In contrast, cytotoxic edema is seen primarily in gray matter and develops slowly as excitotoxins cause accumulation of intracellular calcium and sodium, leading to an osmotic gradient that draws in water [4, 1]. Military neurosurgeons have noted the common presence of diffuse cerebral edema among severe bTBI patients [73].

Another particularly common secondary outcome of blast-induced TBI is vasospasm, a condition in which blood vessels spasm, leading to vasoconstriction and possible ischemia and necrosis [136]. Vasospasm indicates severe damage to the brain, and it is worse with higher injury severity [136, 73]. Vasospasm can be caused by chronic depolarization of vascular smooth muscle due to reduced potassium channel activity, release of endothelin along with reduced availability of nitric oxide, cyclic GMP depletion of vascular smooth muscle, potentiation of prostaglandin-induced vasoconstriction, or free radical formation; onset varies from the 2nd to 15th day post-injury, and hypoperfusion occurs in 50% of patients developing vasospasm [136, 73]. Often it is the cause of delayed neurological deterioration [73]. It has been reported that vasospasm occurs in more than 1/3 of patients with TBI [136], and one study found signs of mild, moderate, and severe vasospasm in 29, 23.5, and 17.6% of bTBI patients respectively [7]. Vasospasm is more prevalent when traumatic subarachnoid hemorrhage is also present acutely [73, 115].

Cerebral edema and vasospasm can both lead to cerebral ischemia, or restriction in blood supply, which is associated with poor neurological outcome — i.e., death or vegetative state [136]. Cerebral ischemia may occur through morphological injury as a result of mechanical displacement, hypotension in the presence of autoregulatory failure, inadequate availability of nitric oxide or cholinergic neurotransmitters, or vasoconstriction [136]. Ischemia can lead to brain tissue hypoxia, or deprivation of oxygen supply, which can cause infarction of neuronal tissue and thus poor outcome [136, 33, 132]. Additionally, hyperemia, or increase in blood flow, may follow post-traumatic ischemia, leading to increases in cerebral blood volume and intracranial pressure [136]. Severe bTBI patients have been known to develop delayed increased intracranial pressure 14-21 days after the initial insult [73]. Both ischemia and hyperemia refer to mismatch between cerebral blood flow and cerebral metabolism; following TBI, cerebral blood flow autoregulation is impaired in most patients [136]. It has been claimed that the presence of hypotension is the single most important predictor of mortality [33].

1.2   Blast Injury Mechanisms

Having discussed the definition, symptoms, and pathophysiology of mTBI in general, we now turn our attention to the mechanisms by which a blast might induce a traumatic brain injury. First, when an explosive device detonates, a chemical reaction occurs that rapidly releases gas and heat. The gas radially expands as a supersonic, high-pressure blast wave, and the leading edge of the blast wave compresses the host medium to create a shock front. For an ideal free-field explosion in air, the blast wave can be modeled as a Friedlander waveform, which is characterized by a rapid rise to peak pressure immediately followed by an exponential decay of the overpressure and a relatively prolonged underpressure [11]. If the blast wave encounters a solid object, such as a wall or other structure, it is significantly modified as it reflects from the object and diffracts around it; assuming that air behaves as an ideal gas, which is reasonable for the range of blast intensities relevant to bTBI, the overpressure of

the reflected wave can be up to 8 times greater than the overpressure of the incident wave. The three-dimensional fluid flow field characterizing an explosion can thus be very complex, and there is considerable room for variability in military-associated blast exposure.

Blasts can result in four types of injury: 1) primary blast injury, which results from direct interaction of the blast wave with body tissue; 2) secondary blast injury, which results from the impact of debris and shrapnel; 3) tertiary injury, which results from individuals being displaced by blast wind and impacting stationary objects; and 4) quaternary blast injury, which encompasses all other explosion-related injuries, including burns, inhalation injuries, crush injuries, and asthma [35, 34, 22]. Primary blast injury, which is unique to blast injury, is not well understood, particularly as it relates to TBI. The organs most susceptible to primary blast injury are the air-filled organs such as the ears, lungs, and gastrointestinal (GI) tract [41], with the most common injury being rupture of the tympanic membranes [92]. Although research efforts in prior decades focused on blast lung injuries, such injuries have occurred only infrequently during OEF/OIF, probably due to advances in body armor, and blast-related GI tract injuries have been even rarer [73]. Now, with soldiers surviving higher intensity blasts that previously would have been fatal due to lung or GI tract injury, focus has shifted to blast-induced brain injury. The brain, residing in a fluid-filled cavity, is vulnerable to blasts [41], but little is known about how blasts affect the brain. Here, focusing solely on primary blast injury, we investigate the effects of blast waves on the human brain.

A number of animal studies have demonstrated that blasts can result in various manifestations of brain damage. Studies subjecting rats to blasts with overpressures ranging from 20 kPa to 12.5 MPa have observed varying degrees of brain injury. For example, one study found that rats subjected to 20 kPa blasts experienced cortical neuron degeneration and significant impairment of performance on tests of coordination, strength, and startle response [86]. Another study found that exposing rats to blasts with overpressures ranging from 130 to 260 kPa resulted in mild injury, with impaired function in a beam walk test and downregulation of genes involved in neu-

rogenesis and synaptic transmission but no evidence of structural damage [110], and a different study found that rats subjected to 147 kPa air blasts suffered from prominent areas of cortical loss, gliosis, and infiltration, as well as hemorrhage and extensive necrosis [75]. Studies also found that application of 241 kPa blasts to rats resulted in multifocal axonal degeneration indicative of DAI, particularly in the cerebellar and brainstem white matter tracts, mild multifocal neuronal death, and increased blood-brain barrier permeability [48], application of 1 MPa shock waves resulted in mild morphological changes in neurons, and application of 12.5 MPa shock waves resulted in cerebral contusional hemorrhage associated with neuronal apoptosis [62].

A number of rat studies have also noted recovery following blast-induced neurotrauma. For example, one study found that while exposure of rats to a 77.3 kPa blast resulted in darkened, shrunken neurons, TUNEL-positive cells in white matter, and narrowed vasculature one day post injury, the effects had largely disappeared by 7 days post injury [105]. They also found that blast exposure resulted in transient changes in gene expression; while the expression of 5,786 genes showed significant changes following blast exposure, by 7 days post injury, most of the genes had returned to a baseline level of expression. They concluded that blast exposure can result in an acute transient ischemic cerebral environment that can recover with time after injury.

Studies of larger animals have also observed blast effects on the brain. For example, a porcine study found that exposure to free air explosions with peak overpressure of 237 kPa resulted in transient flattening of the electroencephalogram (EEG) and short-lasting apnea, indicating a blast wave-induced effect on the brainstem or higher controlling center [119]. One early study of 18 rhesus monkeys trained to perform certain tasks found that exposure to shock tube blasts of 207, 276, and 345 kPa resulted in mild, transient performance decrement [18], and a recent study of 14 macaque monkey subjected to blasts at either 80 or 200 kPa found structural changes in the brain – Purkinje neurons in the cerebellum were darkened, and pyramidal neurons in the hippocampus were shrunken and condensed – that correlated well with observed functional changes [76]. For example, one monkey found to have a lesion in the cere-

37

bellum exhibited drastically impaired motor coordination, and another monkey with degeneration in the hippocampal neurons was found to have mild memory deterioration [76]. Demyelination, activation of microglial cells, and apoptosis involving astrocytes and oligodendrocytes were also observed [76].

The animal studies also demonstrate that the threshold for fatality due to blast-induced brain injury is higher than that for fatality due to blast lung injury; this is expected since the lungs, as air-filled organs, are particularly vulnerable to blasts. For example, a study exposing rabbits to blasts with overpressures of 600 kPa, which is considered lethal for pulmonary injury, found that three out of five specimens that had their thorax enclosed survived the blasts [106]. More explicitly, when Rafaels et al. subjected 12 rabbits to shock tube blasts with overpressures ranging from 168.5 to 1084.6 kPa and established a human survival risk function, they found that the 50th percentile pressure for brain fatality is 750 kPa, which is more than double the 50th percentile pressure for pulmonary fatality of 305 kPa [106].

Despite the reasonably large number of animal studies that have begun investigating blast-induced TBI, the mechanism by which blasts result in brain damage remains in dispute. One proposed mechanism suggests that shock waves could directly propagate through the cranial cavity as stress waves, which travel around the speed of sound with high amplitude and can injure tissue through spalling, implosion, and pressure differentials [70]. A 1961 study exposing rhesus monkeys to air blasts found a large fraction of the pressure was transmitted into the brain through the skull, while little was transmitted from the torso to the brain [70]. Studies of rats and rabbits exposed to blasts also demonstrated that pressure waves could be transmitted directly to the brain with only slight change in amplitude [70]. Alternatively, it has been suggested that the central nervous system (CNS) could be injured by blasts through the cerebral vasculature via a thoracic mechanism [27]. Studies have shown that ballistic pressure waves, which are generated when a projectile enters a viscous medium, can cause remote injuries; for example, studies have found that shooting pigs in the thigh can result in apnea, EEG suppression, microscopic neuronal damage, and elevated pressures within the brain [27]. Similarly, studies have shown that behind

armor trauma, which results when impacts to body armor transmit sufficient force to tissue behind the armor, can result in EEG suppression and death [27]. These studies demonstrate that localized trauma can lead to remote injuries, and they provide some support for the hypothesis that blast waves can be transmitted from the torso to the brain through the vasculature. However, a recent rat study observed no rise in blood pressure or fall in heart rate during the first 15-30 s following blast exposure, suggesting the absence of a vascular surge leading to brain injury [68]. Also, it has been suggested that acceleration of the head can lead to coup-contrecoup injury akin to that observed in impact-related TBI [33]. However, one rat study found no evidence of cortical contusions following blast exposure, arguing against coup injury from acceleration [68]. Finally, it has been suggested that skull flexure following blast exposure can lead to brain injury [88]. In one rat study, researchers found that exposure to shock waves causes deflections in the skull, with greater deflections resulting from higher intensity shock waves, and they suggested that skull flexure could cause ICP gradients within the rat brain [19]. However, another rat study observed no inward flexure of the skull, or any type of injury or weakening of the bones or sutures, following exposure to blasts with overpressures ranging from 262 to 1372 kPa [68]. It still remains unknown which mechanism, or combination of mechanisms, accounts for blast-related TBI.

1.3 Computational Models of Blast-Induced TBI

Since blast experiments cannot be conducted on humans, numerical simulations are critical to furthering our understanding of blast-induced TBI. The first simulations that used a biofidelic human head model to study the interaction of blast waves with the head were presented in [87]. In that study, and in work presented in [94], we established that direct propagation of blast waves into the brain occurs, and we further found that blast intensities corresponding to the pulmonary injury threshold could lead to stresses in the brain that exceeded the stresses resulting from concussive impact. That work suggested that blasts were a plausible cause of TBI. Since then, a

number of computational studies of blast-induced TBI have emerged. Some of these studies have used grossly simplified models that fail to capture the physics involved. Moss and King, for example, conducted blast simulations in which the human head was represented as an ellipsoid; a viscoelastic brain was surrounded by a layer of cerebrospinal fluid (CSF) and a layer of linear elastic skull [88]. Using ALE3D, an arbitrary Lagrangian-Eulerian multi-physics code, they subjected the ellipsoidal model to a 100 kPa blast wave and reported a skull flexure mechanism. However, the results are unreliable due to the complete lack of anatomical structures in the head model and the use of very basic constitutive models; the simulations failed to capture any of the effects of the human head's complex geometry on blast wave mitigation or to accurately represent the mechanical behavior of the head tissues.

Other studies have used more realistic head models. For example, Grujicic et al. [53] used a commercial human head model with Abaqus/Explicit to replicate the simulations we described in [87]. Using the material models and blast conditions from [87], they obtained results that were consistent with those reported in [87]. In another study, Chafi et al. developed a coarse, 27,971-element head model consisting of a brain, CSF, skull, falx and tentorium, dura mater, pia mater, and scalp [24]. The brain tissue was modeled using a hyperelastic Mooney-Rivlin model combined with a linear viscoelastic model, the skull, scalp, and membranes were modeled as linear elastic materials, and the CSF was represented by linear elastic elements with a fluid option. Using LS-DYNA, an explicit, non-linear finite element code, simulations were conducted with incident overpressures of 243.18, 618.08, and 881.53 kPa. For all three blast scenarios, peak pressures exceeded a proposed concussion threshold of 235 kPa at the coup site, and peak average maximum shear stresses exceeded a proposed injury threshold of 16.5 kPa at the coup and contrecoup sites. Additionally, it was found that the 618.08 kPa condition resulted in shear stresses exceeding the proposed injury threshold in the brainstem, and the 881.53 kPa condition resulted in shear stresses exceeding the threshold in the brainstem, cerebellum, and corpus callosum. The study thus suggested that blasts with overpressures ranging from 243.18 to 881.53 kPa could lead to concussion and axonal injury at various locations within the brain.

Some studies have also been conducted with anatomically correct head models that are based on medical imaging data. For example, Taylor and Ford constructed a head model consisting of white matter, gray matter, skull, and CSF from high-resolution photographs of a cryogenically frozen human female available from the Visible Human Project (VHP) [123]. The skull was represented by a compressible, linear elastic, perfectly plastic constitutive model with a damage model to capture fracture, the white and gray matter were represented by an elastic compressible equation of state model for the volumetric response and a three-term Maxwell viscoelastic model for the deviatoric response, and the CSF was modeled using a nonlinear tabular equation of state. Using the shock physics wave code CTH, the head model was subjected to a 1.3 MPa blast from anterior, posterior, and lateral directions. For all blast orientations, it was found that maximum pressures, which reached 3-4 MPa, occurred at the coup site, and maximum volumetric tension, which reached 0.8 MPa, occurred at the contrecoup site. It was also found for all blast orientations that high shear stresses occurred in the subfrontal regions and brain stem; for the anterior and posterior blasts, it was further found that high shear stresses occurred in the temporal lobes and cortical area, and for the lateral blast it was found that elevated shear stresses were diffusely distributed in the right hemisphere and concentrated in focal areas in the left hemisphere. This study thus demonstrated that blasts could lead to the development of significant levels of pressure, volumetric tension, and shear stress in focal areas on a short time scale and that stress patterns are dependent on the orientation of the blast wave and the complex geometry of the skull, brain, and tissue interfaces. The U.S. Army Aeromedical Research Laboratory (USAARL) and CFD Research Corporation (CFDRC) have also developed a computational head model based on the VHP and subjected that model to a blast with overpressure of 1.6 MPa using CoBi, their multiphysics software tool [104]. And recently, the Wayne State University Head Injury Model (WSUHIM), a high-resolution finite element human head model that has been extensively used in impact studies, has been used in blast simulations [117]. The model, which has over 330,000 elements, consists of a scalp, skull with an outer table, diploe, and inner table, dura, falx cerebri, tentorium,

sagittal sinus, transverse sinus, bridging veins, CSF, arachnoid membrane, pia mater, hemispheres with distinct white and gray matter, cerebellum, brainstem, lateral ventricles, third ventricles, facial bones, nasal cartilage, teeth, temporal mandibular joint, ligaments, flesh and skin. Using LS-DYNA, this detailed head model was subjected to front, side, and back blasts with overpressures of 0.21-0.61 MPa and durations of 1-4 ms. The blasts were found to result in peak brain pressures of 0.7-1.8 MPa in the cortex and peak brain strains of 2-11%.

Some groups have begun efforts to validate their computation models against data from experiments involving physical head surrogates. For example, Ganpule et al. has compared surface pressure measurements from shock tube experiments involving a physical surrogate based on the Hybrid III dummy head with simulations conducted using a three-dimensional human head model developed using VHP data [47]. The computational model consisted of skin, skull, and subarachnoid space, which were modeled as linear, elastic, isotropic materials, and brain, which was modeled using an elastic volumetric response and a viscoelastic shear response. They found good agreement between the surface pressure profiles from the experiments and simulations at five locations on the surface of the head following exposure to a frontal blast. From the simulations, they found that the intracranial pressure profiles reflected a coup-countercoup pattern, with a compressive wave front propagating from the incident blast side and a tensile wave front propagating from the opposite side. They further noted that while at a frontal location, peak pressure was due to direct transmission of the blast wave into the brain, at other locations, pressure profiles were governed by a combination of a stress wave in the skull, a pressure wave in the brain, wave reflections from tissue interfaces, and the surface pressure wave. They also noted that the flow field around the head was governed by the geometry of the head.

Some recent studies have also begun efforts to link mechanical response to functional response. For example, Kraft et al. has combined a finite element human head model with structural connectome-based analysis to predict structural network degradation following head impact [66]. In their study, Kraft et al. obtained T1 and diffusion tensor MR images from an individual. The T1 images were used to construct

a three-dimensional, biofidelic finite element volume mesh, and the DTI images were used to construct a fiber tractography representing the location of axonal bundles. They then assembled the structural connectome, which consisted of nodes representing 83 regions of interest connected by edges that represented pathways that the DTI tractography traverses. Using the finite element model, which consisted of 1.39 million tetrahedral elements, they conducted impact simulations in which a force was applied to the forehead in the anteroposterior direction. The input force-time curve had a peak force of 7 kN at 2.75 ms. From the finite element simulation, they obtained mechanical stress and strain in the direction of the axonal fiber bundles. They then used a damage model based on data from rat experiments to predict cellular death based on axonal strain and strain rate, and they degraded the edges of the structural network based on the computed cellular death levels. They found that the temporal and occipital regions had the largest values of axonal strain and thus the highest amount of cellular death. 96 hours post injury, 19.7% of the network edges were fully degraded, but no network nodes were completely disconnected. By that time, network measures of global and local efficiency were significantly reduced. This type of analysis, which has not yet been applied to investigation of blast-induced injury, offers a promising route to connect biomechanical response to neurophysiological insight.

In addition to computational studies examining the effects of blast exposure on the human head, there have been some computational studies involving animal head models. For example, Teland et al. conducted a numerical and experimental investigation into the effects of low-level blast exposure on pigs [124]. Using a two-dimensional pig head model that consisted of a skull modeled as an elliptical surface and a brain modeled as a solid ellipse, simulations were conducted in which the ellipsoidal model was exposed to blasts with peak overpressures of 20-45 kPa. They found reasonable agreement with experimental results, and they also found that the blast wave propagates directly through the skull, that the orientation of the head is important, and that the presence of an opening in the skull has minimal influence on intracranial pressures. Another study constructed a more accurate computational pig model con-

sisting of skull, brain, CSF, dura, and pia using CT and MRI data [145]. The skull was modeled as a linearly elastic material, the brain tissues and CSF were modeled using a viscoelastic constitutive relation, and the pia and dura mater were modeled as thin shell elements and were assumed to be linearly elastic. In a joint numerical and experimental investigation, pigs were subjected to side blasts from a shock tube using 0.48 and 0.61 kg TNT. Comparing the intracranial pressures at rostral, caudal, and medial locations in the brain, they found that the simulated intracranial pressures were within 12% of the experimental values. From the simulations, they also observed that there were higher pressures in the frontal and occipital regions, possibly due to wave reflection at the skull/brain interface. Examining strain, they found that the highest strains of 1.7% were in the brainstem, and the lowest strains of 0.2% were in the center of the brain. They also found that strains within the skull were two orders of magnitude lower than the strains within the brain and that the maximum deflection of the skull was less than 0.5 mm.

Another animal head model was developed by Zhu et al. [144]. Using a rat head model that included cerebral gray matter, corpus callosum, brainstem, cerebellum, lateral ventricle, 3rd ventricle, 4th ventricle, internal capsule, external capsule, olfactory bulb, the cephalic end of the spinal cord, and the skull, they conducted simulations exposing the rat head model to a frontal blast with an incident overpressure of 85 kPa and compared the simulation results with experimental results. They found that the simulations predicted pressure-time histories at the cortex and lateral ventricle that were in reasonable agreement with experimental results, with the peak pressures from the simulation lower than those from the experiments by 2-7%. From the simulations, they also observed that the overpressures in the anterior and posterior regions were 50% higher than those in the vertex and central regions, indicating a higher possibility of injuries in the coup and contrecoup sites. They also found that shear stresses and principal strains remained low, suggesting that they are not the main mechanism causing injury.

1.4 Thesis Overview

This thesis aims to further our understanding of blast-induced TBI through computational modeling. Simulations provide a uniquely practical means of investigating the mechanical effects of blast waves on the human head, given that blast injury experiments cannot be conducted on humans. In Chapter 2, we describe a detailed computational framework for investigating the mechanical response of the human head to blasts that includes blast-structure interaction codes, a three-dimensional, biofidelic human head model generated from high-resolution medical imaging data, and an experimentally-validated constitutive model for brain tissue. Using this framework, we can obtain spatially and temporally resolved descriptions of relevant mechanical fields, such as stress, strain, and acceleration, following blast exposure, and we can identify anatomical regions that experience the highest intensities of injury-relevant metrics. This, in turn, can be instrumental in the development of blast mitigation strategies.

In order to assess the ability of this computational framework to describe the blast response of mechanical and biological bodies, we conduct a collaborative validation effort. At the International State-of-the-Science Meeting on Non-Impact, Blast-Induced Mild Traumatic Brain Injury that was held in 2009, the lack of validated computational models was identified as a key knowledge gap that needed to be filled [61]. To that end, we pursue the validation of our computational framework by comparing simulation results with data from a broad range of experiments. For example, we compare simulation results with data from free-field blast tests involving physical human head surrogates that were conducted at the Naval Surface Warfare Center, Carderock Division, Chapter 3. In addition, to evaluate whether our framework is able to capture the mechanical response of biological tissue to blast loading, we compare simulation results with data from laboratory-scale shock tube tests involving pigs and human cadavers, Chapter 4.

Given the widespread exposure of U.S. service members to blasts from IEDs, it is critical that we understand how current equipment affects the propagation of blast

waves in the human brain. It is also essential to begin investigating strategies to protect against blast effects, such as by adding a face shield to the ACH. Although there are no bTBI criteria to provide a solid basis for PPE modifications to increase protection, demonstrating mitigation of the physical effects of blasts on brain tissue is still a critical step in developing mitigation strategies. To that end, in Chapter 5 we use our modeling framework to evaluate the potential blast-mitigating effects of the ACH, which is currently used by the U.S. Army, as well as to investigate possible modifications that might improve blast mitigation. The work described in Chapter 5 represents a first step in evaluating the blast protection performance of current PPE and developing blast mitigation strategies.

We also use the modeling framework to tackle another important identified gap in bTBI research [61]. In recent years, an increasing number of animal blast experiments has been conducted in an effort to improve our understanding of the effects of blast waves on the central nervous system. However, in the absence of interspecies scaling laws, it is difficult to apply results from those experiments to humans. To help address this need, we conduct simulations using mouse, pig, and human head models, and we develop relations that allow us to translate measures of blast intensity across species, Chapter 6. Finally, Chapter 7 contains conclusions and comments on future work.

Chapter 2

Modeling Framework

2.1 Computational Framework

The blast simulations were conducted using an extension of the Virtual Test Facility (VTF), a suite of computational fluid dynamics (CFD) and computational solid dynamics (CSD) solvers that can be coupled through an integration framework that facilitates simulations of blast-wave loading of solids on high performance massively parallel computing platforms [30, 32]. In the blast simulations, a Lagrangian finite element solid solver was used in combination with AMROC (Adaptive Mesh Refinement in Object-Oriented C++), an Eulerian fluid solver. Constitutive models describing the mechanical response of various tissues and biological structures have been added to the solid solver, and a point source model that accurately describes blast wave initialization has been integrated into AMROC. Both the solid solver and AMROC have been implemented in parallel, as described in [32].

2.1.1 Solid Mechanics of Deforming Tissues

The solid solver is based on a conventional Lagrangian formulation for describing large deformations of solids [32]. Here we briefly outline the continuum framework and numerical formulation.

Continuum Framework

The motion of a reference body B_0 can be described by the deformation mapping $\mathbf{x} = \varphi(\mathbf{X}, t)$, where $\mathbf{X}$ gives the coordinates of points in B_0 and $\mathbf{x}$ gives the positions of material particles $\mathbf{X}$ at time t; velocity and acceleration are given by $\dot{\varphi}(\mathbf{X}, t)$ and $\ddot{\varphi}(\mathbf{X}, t)$ respectively. Local deformation is described by the deformation gradient:

$$\mathbf{F} = \nabla_0 \varphi(\mathbf{X}, t) \tag{2.1}$$

where ∇_0 is the material gradient defined over B_0. The determinant of $\mathbf{F}$, $J = \det(\mathbf{F}(\mathbf{X}, t))$, is the Jacobian of the deformation and a measure of the ratio of deformed to undeformed volume. The motion of the body is subject to conservation of linear momentum, which is given by:

$$\nabla_0 \cdot \mathbf{P} + \rho_0 \mathbf{B} = \rho_0 \ddot{\varphi} \tag{2.2}$$

where $\mathbf{B}(\mathbf{X}, t)$ is the body force, $\mathbf{P}(\mathbf{X}, t)$ is the first Piola-Kirchhoff stress tensor, and $\rho_0(\mathbf{X})$ is the mass density. The symmetric Cauchy stress tensor σ can be obtained from the first Piola-Kirchhoff stress tensor $\mathbf{P}$ through the relation:

$$\sigma = J^{-1} \mathbf{P} \mathbf{F}^T \tag{2.3}$$

We can additively decompose $\mathbf{P}$ into an equilibrium part $\mathbf{P}^e$ and a viscous part $\mathbf{P}^v$:

$$\mathbf{P} = \mathbf{P}^e + \mathbf{P}^v \tag{2.4}$$

In materials without strength, $\mathbf{P}^e$ reduces to:

$$\mathbf{P}^e = -Jp\mathbf{F}^{-T} \tag{2.5}$$

where p is the hydrostatic pressure obtained from an equation of state. We adopt the fluids convention and regard compressive pressure as positive and tensile pressure as

negative. We also assume Newtonian viscosity, where the viscous Cauchy stress σ^v is given by:

$$\sigma^v = 2\eta_h(\text{sym}\dot{\mathbf{F}}\mathbf{F}^{-1})^{\text{dev}} \tag{2.6}$$

η_h is the Newtonian viscosity coefficient, and sym and dev denote the symmetric and deviatoric components of a tensor respectively. $\mathbf{P}^v$ can then be obtained:

$$\mathbf{P}^v(\dot{\mathbf{F}}, \mathbf{F}) = J\sigma^v\mathbf{F}^{-T} \tag{2.7}$$

The boundary conditions for the problem are formulated by partitioning the boundary ∂B_0 into a Dirichlet boundary ∂B_{01} and a Neumann boundary ∂B_{02}. The boundary conditions are then given by:

$$\varphi = \bar{\varphi} \quad \text{on} \quad \partial B_{01} \tag{2.8}$$

$$\mathbf{P} \cdot \mathbf{N} = \bar{\mathbf{T}} \quad \text{on} \quad \partial B_{02} \tag{2.9}$$

where $\bar{\varphi}$ is the prescribed deformation mapping on ∂B_{01}, $\mathbf{N}$ is the unit outward normal to ∂B_{02}, and $\bar{\mathbf{T}}$ are the prescribed tractions on ∂B_{02}. We can then obtain the weak form of the field equations. Starting from:

$$\nabla_0 \cdot \mathbf{P} + \rho_0\mathbf{B} = \rho_0\ddot{\varphi} \quad \text{in} \quad B_0 \tag{2.10}$$

$$\mathbf{P} \cdot \mathbf{N} = \bar{\mathbf{T}} \quad \text{on} \quad \partial B_{02} \tag{2.11}$$

we enforce the governing equations weakly:

$$\int_{B_0} (\nabla_0 \cdot \mathbf{P} + \rho_0\mathbf{B} - \rho_0\ddot{\varphi})\, \mathbf{v}\, d\Omega + \int_{\partial B_{02}} (\mathbf{P} \cdot \mathbf{N} - \bar{\mathbf{T}})\, \mathbf{v}\, dS = 0 \tag{2.12}$$

for all $\mathbf{v}$ in the space of admissible displacements V. Integrating by parts and applying the boundary conditions, we arrive at the principle of virtual work:

$$\int_{B_0} \rho_0\mathbf{B} \cdot \mathbf{v}\, d\Omega - \int_{B_0} \mathbf{P} : \nabla_0\mathbf{v}\, d\Omega + \int_{\partial B_{02}} \bar{\mathbf{T}} \cdot \mathbf{v}\, dS = \int_{B_0} \rho_0\ddot{\phi} \cdot \mathbf{v}\, d\Omega \tag{2.13}$$

Numerical Formulation

The continuum framework is then implemented using a time discretization of the momentum and constitutive equations and a finite element discretization of the solid. We first consider finite element interpolations of the form:

$$\varphi_h(\mathbf{X}) = \sum_{a=1}^{N} x_a N_a(\mathbf{X}) \tag{2.14}$$

where φ_h is the deformation mapping interpolant, x_a is the current position at node a, N_a are the displacement shape functions, and a ranges over N nodes. In the simulations, we use 10-noded quadratic tetrahedral elements. We can then write the principle of virtual work as:

$$\int_{B_0} \rho_0 \mathbf{B} N_a \, d\Omega + \int_{\partial B_0} \bar{\mathbf{T}} N_a \, dS - \int_{B_0} \mathbf{P} : \nabla_0 N_a \, d\Omega = \int_{B_0} \rho_0 N_a N_b \, d\Omega \, \ddot{x}_b \tag{2.15}$$

This can also be written as $\mathbf{f}_a^{ext} - \mathbf{f}_a^{int} = \mathbf{f}_a^{inert}$, where:

$$\mathbf{f}_a^{ext} = \int_{B_0} \rho_0 \mathbf{B} N_a \, d\Omega + \int_{\partial B_0} \bar{\mathbf{T}} N_a \, dS \tag{2.16}$$

$$\mathbf{f}_a^{int} = \int_{B_0} \mathbf{P} : \nabla_0 N_a \, d\Omega \tag{2.17}$$

$$\mathbf{f}_a^{inert} = \int_{B_0} \rho_0 N_a N_b \, d\Omega \, \ddot{x}_b \simeq \mathbf{M}_{ab} \ddot{x}_b \tag{2.18}$$

$\mathbf{f}_a^{ext}$, $\mathbf{f}_a^{int}$, and $\mathbf{f}_a^{inert}$ are the external, internal, and inertial forces respectively, and $\mathbf{M}$ is the diagonal lumped mass matrix.

For the temporal discretization, we use a Newmark time-stepping algorithm:

$$\mathbf{x}_a^{n+1} = \mathbf{x}_a^n + \Delta t \dot{\mathbf{x}}_a^n + \Delta t^2 \left[\left(\frac{1}{2} - \beta \right) \ddot{\mathbf{x}}_a^n + \beta \ddot{\mathbf{x}}_a^{n+1} \right] \tag{2.19}$$

$$\dot{\mathbf{x}}_a^{n+1} = \dot{\mathbf{x}}_a^n + \Delta t [(1 - \gamma) \ddot{\mathbf{x}}_a^n + \gamma \ddot{\mathbf{x}}_a^{n+1}] \tag{2.20}$$

$$\ddot{\mathbf{x}}_a^{n+1} = \mathbf{M}_{ab}^{-1} [\mathbf{f}^{ext} - \mathbf{f}^{int}]_b^{n+1} \tag{2.21}$$

where β and γ are Newmark parameters. In the simulations, we use $\beta = 0$ and $\gamma = \frac{1}{2}$, which results in an explicit, second-order accurate time integration scheme.

Artificial Viscosity

An artificial viscosity scheme was implemented to avoid numerical oscillations in the propagation of waves [72]. The addition of artificial viscosity spreads the shock front over several grid points without affecting key aspects of shock dynamics, such as shock speed, and without introducing artifacts such as spurious oscillations in the shock profile [72]. We assume the viscosity coefficient comprises two terms:

$$\eta_h = \eta + \Delta\eta \tag{2.22}$$

where η is the physical viscosity coefficient of the material and $\Delta\eta$ is the added artificial viscosity [72]. At a given Gauss quadrature point, the artificial viscosity coefficient $\Delta\eta$ is given by:

$$\Delta\eta = \begin{cases} \max(0, -\frac{3}{4}h\rho(c_1\Delta u - c_L a) - \eta) & \Delta u < 0 \\ 0 & \Delta u \geq 0 \end{cases} \tag{2.23}$$

where h is a measure of the element size, Δu is a measure of the velocity jump across the element, c_1 and c_L are coefficients, a is the characteristic sound speed, and $\rho = \rho_0/J$ is the mass density per unit deformed volume [72]. To ensure that the artificial viscosity formulation is material frame indifferent, we use the following relation for Δu:

$$\Delta u = h\frac{\partial \log J}{\partial t} \tag{2.24}$$

where $h = (Jd!|K|)^{1/d}$, d is the dimension of space, and $|K|$ is the volume of element K in its reference configuration [72]. The velocity jump is approximated as:

$$\Delta u_{n+1} = h_{n+1}\frac{\log J_{n+1} - \log J_n}{\Delta t} \tag{2.25}$$

51

This artificial viscosity is deviatoric, and parameter values were obtained through calibrations using simple shock applications. Typically, the value of c_1 is close to 1, while the value of c_L is in the range of 0.1 to 1 [72].

2.1.2   AMROC

AMROC, the Eulerian fluid solver used in the blast simulations, is a complex, multi-level simulation code that has the capability to simulate flows with strong shocks, fluid mixing, and highly coupled fluid-structure interaction (FSI) problems [32]. It utilizes a time-explicit finite volume discretization that achieves a proper upwinding in all characteristic fields. In order to efficiently obtain the necessary temporal and spatial resolution, the structured adaptive mesh refinement method is adopted; following a patch-oriented approach, cells flagged by various error indicators are clustered into non-overlapping rectangular grids. Refinement grids are derived recursively from coarser ones, constructing a hierarchy of successively embedded levels. A more detailed description of AMROC is given in [32].

To initialize blasts, a point source blast initialization code based on calculations in [96] has been incorporated into AMROC [10]. The point source blast initialization is based on the released explosive energy, as determined by the type and mass of the explosive, and the distance between the explosion and the target structure. The model assumes that blast waves are produced by an ideal explosion source — that is, by the instantaneous deposition of a fixed quantity of energy at an infinitesimal point in a uniform atmosphere — and thus that the energy produced depends only on the total source energy. The solver uses a finite difference scheme to solve for the flow parameters and obtain the solution for the fully formed blast wave; excellent agreement has been found between results using the initialization code and results from air blast experiments.

The advantage of this approach is that it provides a full-field description of a fully-formed blast wave at any location without having to model the detonation process and the propagation of the blast wave until reaches the target; for example, using this blast initialization code, we can rapidly and accurately simulate blast waves with long

positive durations with minimal computational expense. A more detailed explanation of the point source model and the validation of the blast initialization code is available in [10].

2.1.3 Fluid-Structure Interaction

In the VTF, a loosely coupled approach to fluid-structure interaction is applied [32]. The fluid and solid domains are assumed to be disjoint, with interaction taking place only at the fluid-solid interface, allowing the use of a Lagrangian solid solver and an Eulerian fluid solver. The information exchange is reduced to communicating the velocities and geometry of the solid surface to the Eulerian fluid and imposing the hydrostatic pressure onto the Lagrangian solid as a force acting on its exterior. A temporal splitting method is applied to update the position and velocity of the boundary between time steps. To represent the evolving surface geometry on the Eulerian fluid mesh, a "ghost fluid" approach is used in which some interior cells are used to directly enforce the embedded boundary conditions in the vicinity of the solid surface. As the solid deforms, the solid-fluid boundary is represented implicitly in the fluid solver with a level set function that is constructed on-the-fly from the solid surface mesh. Block-structured mesh adaptation with time step refinement in the fluid allows for the efficient consideration of disparate fluid and solid time scales.

2.2 Mesh Generation

The geometry for a full human head was provided by Dr. David Moore, a neurologist and former TBI Scientific Advisor to the Director of the Defense and Veterans Brain Injury Center (DVBIC). Dr. Moore downloaded high-resolution T1 magnetic resonance (MR) images from the Montreal Neurological Institute at an isotropic voxel dimension of 1 x 1 x 1 mm. The MR images were then merged with bone-windowed computed tomography (CT) images of the head, allowing skull reconstruction using a mutual information algorithm. The volume set of images was semi-automatically segmented into topological closed regions of interest and exported as VRML (Virtual

Reality Modeling Language) files. The segmentation was performed using Amira, an imaging software analysis suite that allows structured regional labeling of image data as well as filtering and co-registration. The images were segmented into 11 distinct head structures: cerebrospinal fluid (CSF), eyes, glia, ventricles, venous sinus, air sinus, muscle, skull, skin/fat, white matter, and gray matter. The VRML files obtained from Dr. Moore were then imported into Ansys ICEM CFD, a meshing software capable of importing CAD models of high topological and geometrical complexity and producing volumetric conformal computational meshes. The software provides mesh decimation, refinement, and smoothing algorithms that can be used to optimize the mesh for computational efficiency. An unstructured finite element mesh was constructed using the Delaunay tetrahedral mesh generation algorithm, and the software's built-in smoothing and decimation functions were used to optimize and coarsen the mesh to obtain a variety of computational meshes with different resolutions. It was determined that meshes with fewer than 700,000 elements were too coarse to describe the intricate topology of some human head anatomical structures relevant for blast injury analysis. Thus, computational meshes ranging from 700,000 to 5,000,000 elements were produced. To balance mesh resolution and computational requirements, a mesh with 743,341 elements was used in the simulations described. The mesh was then further optimized by eliminating bad quality tetrahedra using the HealMesh optimization library. This model is referred to as the DVBIC/MIT Full Head Model (FHM). Figure 2-1 displays views of the skin/fat, gray matter, and white matter meshes from the FHM. Figure 2.2 shows the FHM with cuts in the sagittal, coronal, and axial planes.

The FHM was extended to include the Advanced Combat Helmet (ACH). A computational model of the ACH was developed from a computer-aided design (CAD) model of the actual ACH shell provided by the Natick Soldier Research, Development, and Engineering Center. The CAD model was imported into Ansys ICEM CFD, and geometries of the pads in the standard configuration were constructed and added to the model of the ACH shell. A finite element mesh of the helmet and padding was then generated from the geometries using the Delaunay tetrahedral mesh generation

(a) Skin/Fat   (b) Gray Matter   (c) White Matter
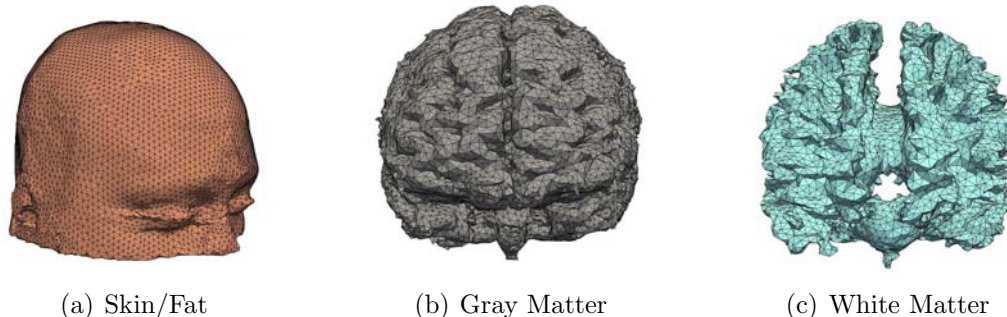
Figure 2-1: Detailed views of the skin/fat, gray matter, and white matter structures in the FHM

algorithm, and the meshes of the helmet and padding were added to the DVBIC/MIT FHM to create the ACH-FHM. The full head-helmet mesh, which consists of 922,852 tetrahedral elements, is shown in Fig. 2.2.

The MIT/DVBIC FHM and ACH-FHM have been made publicly available at http://web.mit.edu/isn/research/model_download.html. In addition to these human head models, computational models of pig and mouse heads were developed for use in simulations. Further details about the pig and mouse head models are provided in Chapters 4 and 6 respectively.

2.3 Material Models and Properties

In order to describe the mechanical response of the various head structures and protective equipment in the blast simulations, three distinct material models were used.

2.3.1 Neo-Hookean Model

The neo-Hookean model extended to the compressible range is a hyperelastic material model; the strain energy density for an incompressible neo-Hookean material is given by:

$$W(C) = \frac{\mu}{2}(I_1 - 3) \tag{2.26}$$

where μ is the shear modulus, C is the right Cauchy-Green deformation tensor, and I_3 is the first invariant of C. Extended to the compressible range, the strain energy

(a)   (b)

(c)
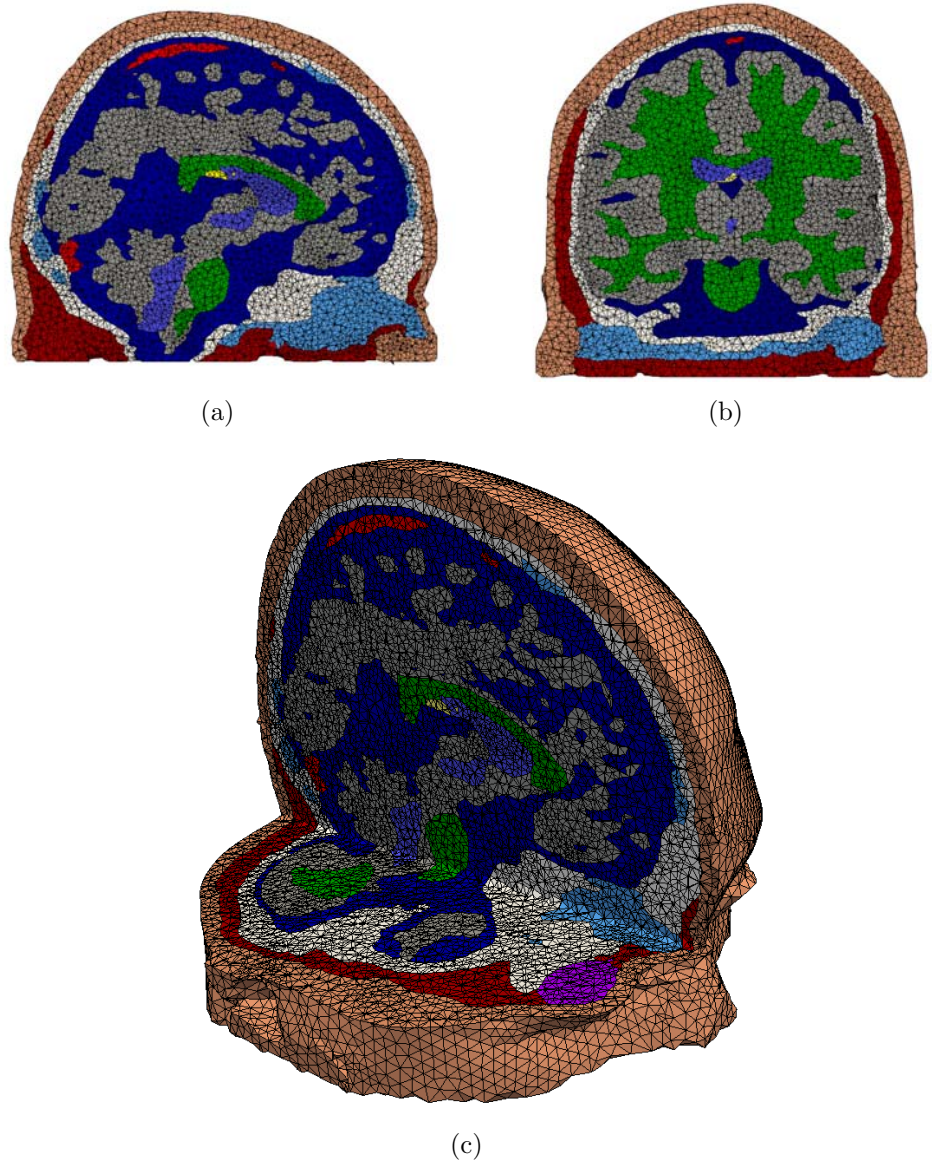
Figure 2-2: Full head model: sagittal cut 2-2(a), coronal cut 2-2(b), and combined sagittal and axial cut showing detail of the full mesh 2-2(c)

(a) FHM with ACH padding   (b) FHM with ACH shell
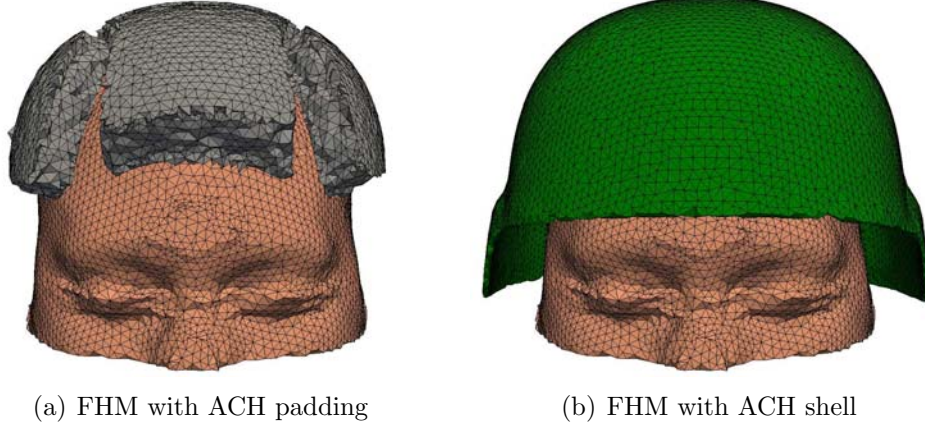
Figure 2-3: Computational head-helmet mesh

becomes:

$$W(C) = \frac{\lambda}{2}\log^2 J - \mu\log J + \frac{\mu}{2}(I_1 - 3) \tag{2.27}$$

where λ is the first Lamé constant. The second Piola-Kirchhoff tensor can then be computed:

$$S_{IJ} = 2\frac{\delta W}{\delta C_{IJ}} = 2\lambda\log J\frac{1}{J}\frac{\delta J}{\delta C_{IJ}} - \frac{2\mu}{J}\frac{\delta J}{\delta C_{IJ}} + \mu\delta_{IJ} \tag{2.28}$$

Given that $\frac{\delta J}{\delta C_{IJ}} = \frac{J}{2}C_{IJ}^{-1}$, we arrive at:

$$S_{IJ} = \lambda\log J C_{IJ}^{-1} + \mu(\delta_{IJ} - C_{IJ}^{-1}) \tag{2.29}$$

Using the relation $\sigma_{ij} = J^{-1}S_{IJ}F_{iI}F_{jJ}$, we obtain the following expression for the Cauchy stress components:

$$\sigma_{ij} = \frac{1}{J}\left[\lambda\log J\delta_{ij} + \mu(b_{ij} - \delta_{ij})\right] \tag{2.30}$$

where $b = FF^T$ is the left Cauchy-Green deformation tensor. For infinitesimal strains, the expression reduces to:

$$\sigma_{ij} \sim \lambda\epsilon_{kk}\delta_{ij} + 2\mu\epsilon_{ij} \tag{2.31}$$

which is the familiar stress-strain relation resulting from Hooke's law, $\sigma = C\epsilon$.

This extended neo-Hookean model was used to describe the protective equipment used in the simulations detailed in Chapters 3 and 5. Given the intensity of the

blast waves under consideration in these simulations, the response of the engineering materials used in the protective structures was expected to stay well within the elastic regime. Consequently, the use of a neo-Hookean nonlinear elastic model for these materials was justified.

2.3.2 Simple Viscoelastic Model

A material model that was used to describe all the head structures except the brain consisted of a volumetric response described by an equation of state and a deviatoric response described by the neo-Hookean model. In the simulations discussed in this thesis, the Hugoniot and Tait equations of state were used.

Hugoniot Equation of State

The Hugoniot equation of state was used to describe the volumetric response of the skull under high strain rate conditions. The shock response of many solid materials is well described by the Hugoniot relation $U_s = C_0 + sU_p$ between the shock wave velocity U_s and the material velocity U_p [38, 84, 140]. C_0 and s are material parameters that can be obtained from experiments. Combining this relation with conservation of mass and momentum, we arrive at the following equation of state:

$$p = \frac{\rho C_0^2 (1 - J)}{[1 - s(1 - J)]^2} \tag{2.32}$$

Tait Equation of State

The Tait equation of state, which is commonly used to model fluids under large pressure variations, is given by:

$$p = B\left[\left(\frac{\rho}{\rho_0} \right)^{\Gamma_0 + 1} - 1 \right] \tag{2.33}$$

where B and Γ_0 are constants [126]. The Tait equation of state provides a reasonable representation of the volumetric response of soft tissues embedded in a fluid medium, and it was therefore employed to describe the tissue response of all the head structures

except the skull and brain. Γ_0 was taken to be the value for water, 6.15. Appropriate bulk modulus values K were selected from the literature, and B was computed for each structure from Γ_0 and K using the relation $K = B(\Gamma_0 + 1)$.

Linear Viscosity

To complete the constitutive description of the head structures, a linear viscosity model was added to both the deviatoric and volumetric response, furnishing a final expression for the Cauchy stress components:

$$\sigma_{ij} = \sigma_{ij}^{\text{e,vol}} + \sigma_{ij}^{\text{e,dev}} + 2\mu_v d_{ij}^{\text{dev}} + \kappa d_{ii}\delta_{ij} \tag{2.34}$$

The shear viscosity term is $2\mu_v d_{ij}^{\text{dev}}$, where d is the symmetric part of the velocity gradient tensor and μ_v is the shear viscosity parameter. The bulk viscosity term is $\kappa d_{ii}\delta_{ij}$, where κ is the bulk viscosity parameter. The volumetric elastic component is given by $\sigma_{ij}^{\text{e,vol}} = -p\delta_{ij}$, where p is obtained from the appropriate equation of state, and the deviatoric elastic component is given by $\sigma_{ij} = \frac{\mu}{J}b_{ij}$, as derived above.

2.3.3   Socrate Brain Tissue Constitutive Model

The mechanical response of the brain was described using the brain tissue constitutive model presented by Prevost et al. [102]. This model, which we refer to as the Socrate model, has been shown to successfully capture observed complexities of brain tissue response in loading, unloading, and relaxation, including nonlinearities, hysteresis, time dependence, volumetric compliance, and rate dependence. Here, we summarize the formulation of the model.

The model is based on a multiplicative decomposition of the total deformation gradient $\mathbf{F}$:

$$\mathbf{F} = \mathbf{F}_A \cdot \mathbf{F}_B \tag{2.35}$$

where $\mathbf{F}_A$ represents the instantaneous elastic component and $\mathbf{F}_B$ represents the viscoelastic component. The viscoelastic response, which is captured by the combination

of a nonlinear short-term viscous element B and a linear viscoelastic backstress network CDE, can be further decomposed:

$$\mathbf{F}_B = \mathbf{F}_C \cdot \mathbf{F}_D \tag{2.36}$$

where the linear viscous element D models the long-term relaxation of the backstress contribution.

The total Cauchy stress can be additively decomposed into its hydrostatic and deviatoric components:

$$\sigma = \sigma_h + \sigma_d \tag{2.37}$$

The volumetric response is described by an equation of state:

$$\sigma_h = K \cdot \ln\left[\frac{J - f_1}{1 - f_1}\right] \cdot \mathbf{1} \tag{2.38}$$

where K represents the bulk modulus of the compressible fraction and $f_1 \approx 0.8$ represents the incompressible tissue fraction. The deviatoric component σ_d is adapted from the freely-jointed 8-chain model developed for macromolecular elastic networks [8]:

$$\sigma_d = \frac{\mu_0}{J} \cdot \frac{\lambda_L}{\lambda} \cdot \mathcal{L}^{-1}\left(\frac{\lambda}{\lambda_L}\right) \cdot (\bar{\mathbf{B}}_A - \lambda^2 \mathbf{1}) \tag{2.39}$$

where μ_0 and λ_L are material properties, $\bar{\mathbf{B}}_A = J^{-2/3} \cdot \mathbf{F}_A \cdot \mathbf{F}_A^T$ is the deviatoric Almansi strain tensor, $\lambda = \left[\frac{1}{3}\text{tr}(\bar{\mathbf{B}}_A)\right]^{1/2}$ is the network stretch, and $\mathcal{L}$ is the Langevin function $\mathcal{L}(\beta) = \coth(\beta) - \frac{1}{\beta}$.

The time-dependent deformation is defined via the evolution of the velocity gradient $\mathbf{L}$:

$$\mathbf{L} = \dot{\mathbf{F}} \cdot \mathbf{F}^{-1} = \dot{\mathbf{F}}_A \cdot \mathbf{F}_A^{-1} + \mathbf{F}_A \cdot \mathbf{L}_B \cdot \mathbf{F}_A^{-1} = \mathbf{L}_A + \tilde{\mathbf{L}}_B \tag{2.40}$$

$\tilde{\mathbf{L}}_B$ can be further decomposed into:

$$\tilde{\mathbf{L}}_B = \tilde{\mathbf{D}}_B + \tilde{\mathbf{W}}_B \tag{2.41}$$

where $\tilde{\mathbf{D}}_B$ denotes the rate of viscous stretch and $\tilde{\mathbf{W}}_B$ denotes the rate of viscous spin. Specifying $\tilde{\mathbf{W}}_B = 0$, the evolution of $\mathbf{F}_B$ reduces to:

$$\dot{\mathbf{F}}_B = \mathbf{F}_A^{-1} \cdot \tilde{\mathbf{D}}_B \cdot \mathbf{F} \tag{2.42}$$

The viscous stretching tensor $\tilde{\mathbf{D}}_B$ is obtained using the relation:

$$\tilde{\mathbf{D}}_B = \dot{\gamma}_0 f_R \left(\frac{\sqrt{\sigma'_B : \sigma'_B}}{\sqrt{2}\sigma_0} \right)^n \cdot \frac{\sigma'_B}{\sqrt{\mathrm{tr}(\sigma'^2_B)}} \tag{2.43}$$

where the reptation factor f_R, which accounts for increasing resistance to viscous flow for increasing levels of viscous deformation, is given by:

$$f_R = \frac{\alpha^2}{(\alpha + \sqrt{\mathrm{tr}(\mathbf{F}_B \mathbf{F}_B^T)/3} - 1)^2} \tag{2.44}$$

The driving stress for the short-term non-linear viscous element B is given by:

$$\sigma_B = \sigma_A - \sigma_C = \sigma_A - \frac{1}{J} \cdot \mathbf{F}_A \cdot \mathbf{S}_C \cdot \mathbf{F}_A^T \tag{2.45}$$

where the 2$^{\mathrm{nd}}$ Piola-Kirchhoff stress in the elastic element C of the backstress network is given by:

$$\mathbf{S}_C = 2G_0 \mathbf{E}_C = 2G_0 \ln \mathbf{V}_C = 2G_0 \ln(\mathbf{F}_C \mathbf{F}_C^T)^{1/2} \tag{2.46}$$

The driving stress for the long-term linear viscous element D is given by the difference between $\mathbf{S}_C$ and $\mathbf{S}_E$, the long-term backstress in elastic element E:

$$\mathbf{S}_D = \mathbf{S}_C - \mathbf{F}_C \cdot \mathbf{S}_E \cdot \mathbf{F}_C^T \tag{2.47}$$

where $\mathbf{S}_E$ is given by:

$$\mathbf{S}_E = 2G_\infty \mathbf{E}_D = 2G_\infty \ln(\mathbf{V}_D) = 2G_\infty \ln(\mathbf{F}_D \mathbf{F}_D^T)^{1/2} \tag{2.48}$$

The evolution of element D is described using the stretching tensor $\tilde{\mathbf{D}}_D$:

$$\tilde{\mathbf{D}}_D = \frac{1}{\sqrt{2}\eta} \cdot \mathbf{S}_D \tag{2.49}$$

where the viscosity η is a material parameter.

2.3.4 Material Properties

The material properties used in the simulations are given in Tables 2.1, 2.2, 2.3, and 2.4. The following sections briefly explain how the material properties for each structure were selected.

Material	ρ (kg/m^3)	E (Pa)	ν
Kevlar	1440	1.24×10^9	0.36
Foam	136	8×10^6	0.2

Table 2.1: Neo-Hookean Model Parameters for Protective Equipment

Material	ρ (kg/m^3)	K (Pa)	G (Pa)	C_0	s
Skull	1412	3.86×10^9	2.664×10^9	1850.0	0.94

Table 2.2: Hugoniot Equation of State and Deviatoric Elasticity Parameters

Material	ρ (kg/m^3)	K (Pa)	G (Pa)	κ (Pa · s)	μ (Pa · s)	Γ_0	c_1	c_L
CSF	1040	2.19×10^9	4.38×10^2	1000	1000	6.15	0.4	0.4
Eyes	1040	2.19×10^9	2.253×10^4	1000	1000	6.15	0.6	0.4
Muscle	1100	1.35×10^5	1.397×10^4	1000	1000	6.15	0.6	1.0
Air Sinus	1040	2.19×10^9	4.38×10^2	1000	1000	6.15	0.4	0.4
Skin/Fat	1100	3.479×10^7	5.88×10^6	1000	1000	6.15	0.6	0.6
Venous Sinus	1040	2.19×10^9	4.38×10^2	1000	1000	6.15	0.4	0.4
Ventricle	1040	2.19×10^9	4.38×10^2	1000	1000	6.15	0.4	0.4

Table 2.3: Tait Equation of State and Deviatoric Elasticity Parameters

ρ (kg/m^3)	G_0 (Pa)	K (Pa)	n	σ_0 (Pa)	λ_L	μ_0 (Pa)	η (kPa · s)	G_∞ (Pa)
1000	6000	1.0×10^7	0.3	2.0×10^3	1.03	1.0×10^4	1.0×10^3	2.0×10^3

Table 2.4: Socrate Model Parameters for the Brain

Protective Equipment

The ACH is constructed out of ballistic fibers such as Kevlar and Twaron; in our models, we used Young's modulus and Poisson's ratio values for Kevlar that were obtained from the literature [6]. The material properties of the foam pads used with the ACH were obtained from the manufacturer, Team Wendy.

Skull

The skull, which is considered a single structure in the FHM, is composed of two types of bone: cortical, or compact bone, and trabecular, or cancellous bone. While cortical bone, which forms the surface of bones, is hard and dense, trabecular bone, which forms the bulk of the interior of most bones, is spongy; Table 2.6, which lists some cortical bone material properties reported in the literature, and Table 2.7, which lists some trabecular bone material properties reported in the literature, demonstrate the differences between the material properties for cortical and trabecular bone. For cortical bone, values for the bulk modulus range from 4 to 8.62 GPa, and values for the shear modulus range from 2.4 to 6.15 GPa. For trabecular bone, values for the bulk modulus range from 0.47 to 3.4 GPa, and values for the shear modulus range from 0.215 to 2.32 GPa. For a skull consisting of both cortical and trabecular bone, some examples of material properties reported in the literature are given in Table 2.5. Values for the bulk modulus range from 3.96 to 7.12 GPa, and values for the shear modulus range from 2.73 to 3.47 GPa. In the FHM, the material properties for the skull, $\rho = 1412 \, \text{kg/m}^3$, K = 3.89 GPa, G = 2.664 GPa, which were all obtained from Dr. David Moore, fall between the literature values for cortical and trabecular bone.

Source	$\rho \, (\text{kg/m}^3)$	K (Pa)	G (Pa)	E (Pa)	ν
Nishimoto (1998) [93]	1456	7.12×10^9	3.47×10^9	8.75×10^9	
Gilchrist (2001) [50]	1410			6.65×10^9	0.22
Taylor (2009) [123]	1412	4.82×10^9			0.22
Chafi (2010) [24]	1800			1.5×10^{10}	0.21

Table 2.5: Skull (Cortical and Trabecular Bone) Material Properties from the Literature

Source	$\rho\,(\mathrm{kg/m^3})$	K (Pa)	G (Pa)	E (Pa)	ν
Ruan (1994) [112]	3000	7.3×10^9	5.0×10^9		
Zhang (2001) [142]	2100			6.0×10^9	0.25
Kleiven (2002 [65]	2000			1.5×10^{10}	0.22
Horgan (2003) [59]	2000			1.5×10^{10}	0.22
Willinger (2003) [138]	1900	6.2×10^9		1.5×10^{10}	0.21
Belingardi (2005) [15]	1800			1.5×10^{10}	0.21
Raul (2006) [109]	1800			1.5×10^{10}	0.21
Ho (2007) [57]	2000			1.5×10^{10}	0.22
Gong (2008) [51]	3000	7.3×10^9			0.22

Table 2.6: Cortical Bone Material Properties from the Literature

Source	$\rho\,(\mathrm{kg/m^3})$	K (Pa)	G (Pa)	E (Pa)	ν
Ruan (1994) [112]	1750	3.4×10^9	2.32×10^9		0.22
Zhang (2001) [142]	1000			5.6×10^8	0.30
Kleiven (2002) [65]	1300			1.0×10^9	0.24
Horgan (2003) [59]	1300			1.0×10^9	0.24
Willinger (2003) [138]	1500	2.3×10^9		4.6×10^9	0.05
Belingardi (2005) [15]	1500			4.5×10^9	0.01
Raul (2006) [109]	1500			4.5×10^9	0.0
Ho (2007) [57]	1300			1.0×10^9	0.24
Gong (2008) [51]	1744	3.4×10^9			0.22

Table 2.7: Trabecular Bone Material Properties from the Literature

CSF

Cerebrospinal fluid (CSF), a Newtonian fluid similar to water in density and viscosity, was modeled as a nearly incompressible solid in the simulations. The bulk modulus, density, and Tait equation of state parameters for water were used, and to stabilize the simulations, a small shear modulus was added. The values selected, $\rho = 1040\,\mathrm{kg/m^3}$, $K = 2.19 \times 10^9$ Pa, and $G = 4.38 \times 10^2$ Pa, fall well within the range of values used for CSF in the literature, some of which are listed in Table 2.8.

Material properties for CSF vary widely in the literature, and in general little explanation is given for how the values were selected. Bulk modulus values in particular span a wide range, from 2.0×10^5 to 2.19×10^{10} Pa, since the bulk modulus, when calculated from the Young's modulus E and Poisson's ratio ν, is extremely sensitive to small variations in ν for virtually incompressible materials with Poisson's ratios near 0.5. In a number of studies in the literature, material property values were selected based on qualitative characteristics of CSF. Gong, for example, used a Poisson's ratio close to 0.5 in order to capture the incompressible fluid behavior of CSF [51], Horgan used the bulk modulus of water and a very low shear modulus due to the fluid nature of CSF [60], and Zhang used the bulk modulus of water and a very low shear modulus to accommodate the pressure gradient and relative movement of the brain [143]. Nishimoto assigned the bulk modulus of the CSF to be $\frac{1}{100}$ that of brain tissue because the dilatation of CSF was considered to be greater than that of brain tissue [93], and Ruan assigned the CSF lower shear and bulk moduli values than the brain in order to allow the brain to move within the skull [112]. Only Willinger even partially used experimental results, finding the value of E through modal analysis [138]; that value was adopted by Raul [109] and Belingardi [15]. However, even using the same E and ν values, Belingardi calculated a bulk modulus value of 2.0×10^5 Pa [15], while Willinger decided to use a bulk modulus value of 2.19×10^{10} Pa [138]. Thus, we can see that significant variation exists in the CSF material property values used in numerical modeling in the literature, and the values appear to be largely based on qualitative assessments of the nature of CSF.

Since the CSF resides in the subarachnoid space and the cerebral ventricular system, the material properties for CSF were applied to both the CSF and ventricle domains of the FHM. Belingardi similarly applied the material properties of CSF to the ventricles [15], while Zhang used the properties of CSF, but with a lower shear modulus, for the ventricles [142]. Additionally, the air sinuses, which are air-filled cavities within the skull and facial bones, were assigned the material properties of CSF as a first approximation; this approximation was also made by Ho [57] and Kleiven and Hardy [64]. The venous sinuses were also assigned the material properties of CSF. The venous structures in the FHM correspond to the dural venous sinuses, which are venous channels located between layers of dura mater in the brain. The venous structures can be modeled as the blood flowing through the dural venous sinuses, which has similar material characteristics to CSF.

Source	$\rho\,(\text{kg/m}^3)$	K (Pa)	G (Pa)	E (Pa)	ν
Ruan (1994) [112]	1040	2.19×10^7	5.0×10^5		0.489
Nishimoto (1998) [93]	1040	2.19×10^7	5.2×10^5		
Gilchrist (2001) [50]				1.485×10^5	0.499
Zhang (2001) [143]	1004	2.19×10^9	5.0×10^2		
Kleiven (2002) [64]	1000	2.1×10^9			0.5
Willinger (2003) [138]	1040	2.19×10^{10}		1.2×10^4	0.49
Horgan (2004) [60]	1000			Water	0.5
Belingardi (2005) [15]	1040	2.0×10^5		1.2×10^4	0.49
Raul (2006) [109]	1040			1.2×10^4	0.49
Ho (2007) [57]	1000	2.1×10^9			0.5
El Sayed (2008) [40]	1004	2.19×10^6	5.0×10^2		
Gong (2008) [51]	1040	2.19×10^6			0.489
Taylor (2009) [123]	1000	1.96×10^9			0.50
Chafi (2010) [24]	1000	2.19×10^9			0.50

Table 2.8: CSF Material Properties from the Literature

Skin/Fat

For the skin/fat, the bulk and shear modulus values were obtained from the E and ν values in the literature for scalp, which consists of skin and underlying fat and muscle. The Young's modulus and Poisson's ratio values in the literature were obtained from experimental data from Zhou and were adopted by Willinger, Belingardi, Raul, Ho,

and Chafi [138, 15, 109, 57, 24].

Source	Type	$\rho\,(\mathrm{kg/m^3})$	E (Pa)	ν
Zhang (2001) [142]	Soft tissue	1100	1×10^6	0.45
Kleiven (2002) [65]	Scalp	1130	16.7×10^6	0.42
Willinger (2003) [138]	Scalp	1000	16.7×10^6	0.42
Belingardi(2005) [15]	Scalp	1200	16.7×10^6	0.42
Raul (2006) [109]	Scalp	1200	16.7×10^6	0.42
Ho (2007) [57]	Scalp	1130	16.7×10^6	0.42
Chafi (2010) [24]	Scalp	1200	16.7×10^6	0.42

Table 2.9: Skin-Related Material Properties from the Literature

Brain Tissue

The Socrate constitutive model for brain tissue includes eight material parameters: K for the overall volumetric response; μ_0 and λ_L for the elastic shear response of network A; G_0, G_∞, and η for the linear viscoelastic backstress network (CDE); and σ_0 and n for the reptation-based short-term viscous response. We adopt the parameter values that Prevost et al. obtained by fitting the model to experimental data from in vitro porcine cortical tissue tests conducted at strain rates up to 3000 s^{-1}. Details of the calibration process are given in Prevost et al. [102].

2.4   Summary

The computational framework presented in this chapter depicts a full environment for describing the mechanics of blast-head interactions. The DVBIC/MIT FHM is a detailed, biofidelic human head model generated from high-resolution medical imaging data, and the material response of each of the 11 structures in this model is described using either an advanced constitutive brain tissue model or conventional models of elastic and viscoelastic response. The material properties for each structure, which were derived from values provided by Dr. Moore, high strain rate brain tissue experiments, and values found in the literature, all fall within the range of values reported in the literature. Overall, this provides a comprehensive tool for simulating blasts, fluid-structure interactions, and the mechanical response of the human head to blasts.

Chapter 3

Validation: Physical Surrogate Tests

3.1 Introduction

In order to evaluate the accuracy with which a computational framework can model a physical system, results obtained using the framework must be compared against experimental results. Recently, a number of studies have begun comparing results from simulations and experiments that expose physical head surrogates to blasts. Some of these studies have used spherical or ellipsoidal physical surrogates to represent the head. For example, Zhu et al. conducted a joint experimental and numerical investigation in which a small, egg-shaped polyethylene shell filled with silicone gel was exposed to shock wave loading [146]. Comparing experimental and numerical pressure histories at the center of the egg-shaped surrogate, they found that the simulation underpredicted the peak positive pressure and overpredicted the peak negative pressure by approximately 4%. In a similar study, Varas et al. conducted experiments and simulations subjecting a polyurethane sphere filled with ballistic gelatin to shock-tube-generated shock waves with a peak overpressure of 40 kPa and a positive duration of 6 ms [131]. They found that in the simulations, pressure histories in the ballistic gelatin had a high-frequency component that corresponded to reflections of the pressure wave against the sphere's boundaries. When the high-frequency

69

component, which was not observed in the experiments, was filtered out, the experimental and simulated pressure histories in the gelatin appeared to be relatively similar. Comparing strains in the skull, they found similar amplitudes in the simulations and experiments, although the vibration period in the simulations was slightly longer. Although both Zhu et al. and Varas et al. found reasonable agreement between pressure histories from experiments and simulations, the simple models used in the investigations failed to capture the effects of the human head's complex geometry. The importance of geometry was evident even from tests involving these extremely simplified models; Zhu et al., for example, found that changing the orientation of the egg-shaped surrogate model, thereby altering the curvature of the fluid-structure interface relative to the shock wave, significantly affected peak pressure values and pressure distribution throughout the model.

Some studies have involved surrogate heads with more biofidelic geometries. In a recent study, a Hybrid III dummy, which was developed for automobile impact tests, was subjected to free-field blasts from 5 kg C4 charges at 3-4 m [74]. Simulations of the experiments were conducted using a simplified human body model and a commercial finite element code. They found the peak linear accelerations from the simulations and experiments to be in good agreement, but the simulations generally overpredicted the Head Injury Criterion (HIC), a measure of the likelihood of head injury due to impact that is calculated from acceleration. Another study that also used a surrogate head based on the Hybrid III dummy head compared results from experiments subjecting the surrogate head to frontal blast loading from a compression-driven air shock tube with simulation results [47]. In the experiments, the surrogate head consisted of a polyurethane skull and attached neck without any intracranial contents, and in the simulations, the three-dimensional human head model was generated using MRI data from the Visible Human Project. Comparing pressure profiles at five locations on the surface of the surrogate head, they found good agreement between the experiments and simulations in terms of peak pressures, nonlinear decay, and positive phase duration, and they found that the simulations were able to capture many of the features of the experimental profiles, including shock front rise time, peaks and

valleys, and secondary reflections.

In another recent study, Roberts et al. obtained a human head finite element model that had previously been developed for automobile crash studies, added a Hybrid III neck, and then fabricated a physical head surrogate model from the solid model files of the computational model [111]. The physical model consisted of a glass/epoxy skull, Sylgard gel brain, and silicone skin, and the computational model consisted of a face, skull, brain, brain stem, and neck. The physical and computational models were subjected to shock tube tests at driver pressures of 517, 690, and 852 kPa, and intracranial pressures, relative brain-skull displacements, and head rotations from the experiments and simulations were compared. They found that the differences in peak intracranial pressures were within about 25%, although they noted that using an elastic model for the skull in the simulations resulted in flexural waves that caused ringing and underdamping. When a viscoelastic model was used for the skull instead, the pressure oscillations decreased. For the peak relative brain-skull displacements, the percent difference between the experiments and simulations ranged from 3 to 68%, and for the head rotations, it was found that the peak rotations in the experiments and simulations occurred at about the same time and were of the same sign.

The work presented in this chapter represents an effort to validate the computational framework described in Chapter 2 using data from experiments in which head/neck manikins were subjected to free-field side blasts. The life-size manikins consist of a polyethylene skull, silicone gel brain, and silicone rubber skin; unlike many of the models used in other experiments, they are not spherical or ellipsoidal, but instead capture the shape of the human head. Further, unlike any of the validation studies in the literature thus far, the physical and computational models described in this chapter incorporate the Advanced Combat Helmet (ACH), allowing us to begin investigating the effects of the ACH on the human head response to blasts. In this chapter, we compare pressure histories from the state-of-the-art experiments and simulations, conducted with and without the ACH, at several locations inside and outside the head.

(a) Polyethylene skull and silicone gel brain

(b) Fully assembled head with external gages
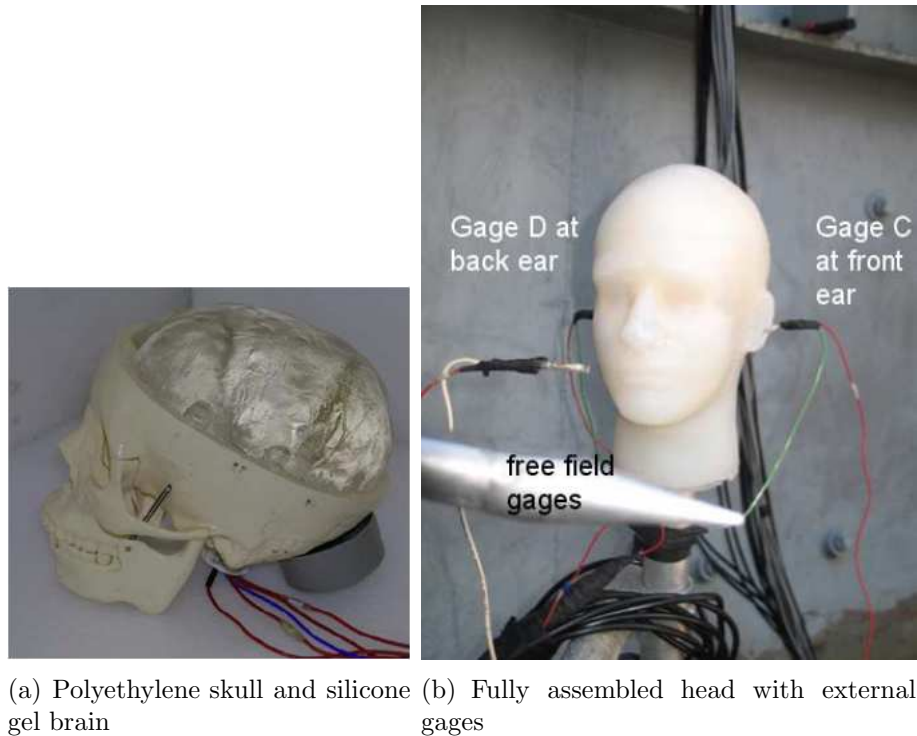
Figure 3-1: The head/neck manikin used in free-field blast tests

3.2 Methods

3.2.1 Experiments

The experiments were conducted by our collaborators at the Naval Surface Warfare Center, Carderock Division; for completeness, we summarize the experimental procedures, which are described in [39]. In the experiments, our collaborators subjected head/neck manikins to free-field side blasts. The manikins consisted of a polyethylene skull, a Sylgard silicone gel brain, and flesh formed from Smooth-On Dragon Skin, a silicone rubber with Shore 20A hardness. Fig. 3-1(a) shows the polyethylene skull with the silicone gel brain resting inside, and Fig. 3-1(b) shows the fully assembled head/neck manikin, along with external gages. Fig. 3-2 shows the fully assembled head/neck manikin with the ACH.

Our collaborators conducted two sets of experiments. In the initial set, they exposed the manikins to free-field side blasts from 0.57 kg pentolite charges located 1.1 m from the left ear of the manikin. Each pentolite charge was placed at ear level,

Figure 3-2: Fully assembled head/neck manikin with ACH

or 1.4 m from the floor of the explosive test pit. They conducted tests both with and without the ACH.

They measured free-field pressure using three gages: Gage A, Gage B, and Gage O. Gages A and O were tourmaline piezoelectric gages manufactured in-house, and Gage B was a PCB Model 137A23 Quartz ICP pressure pencil probe. External gages C and D were located 6.4 mm from the front of each ear; Gage C, which was located directly in front of the left ear, was expected to record the reflected pressure. They also instrumented the manikins with four intracranial pressure gages: E, G, M, and N. Gage M developed problems after initial testing, and the measurements from that gage are not shown here.

In the second set of experiments, our collaborators exposed the manikins to free-field side blasts from 0.057 kg pentolite charges located either 0.71 or 1.1 m from the left ear. They again conducted tests both with and without the ACH. In these tests, free-field pressure was measured by Gage B, and Gages C and D were again located 6.4 mm from the front of each ear. They instrumented the manikins with 6 intracranial pressure gages: E, F, G, H, K, and O. The locations of the gages are shown in Fig. 3-4.
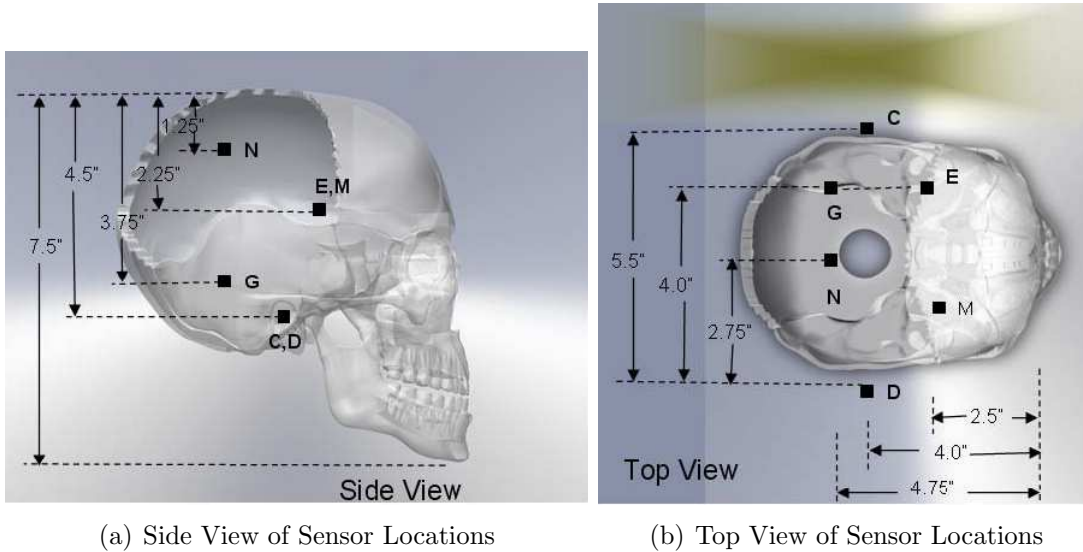
(a) Side View of Sensor Locations

(b) Top View of Sensor Locations

Figure 3-3: Manikin intracranial pressure sensor locations for first set of experiments
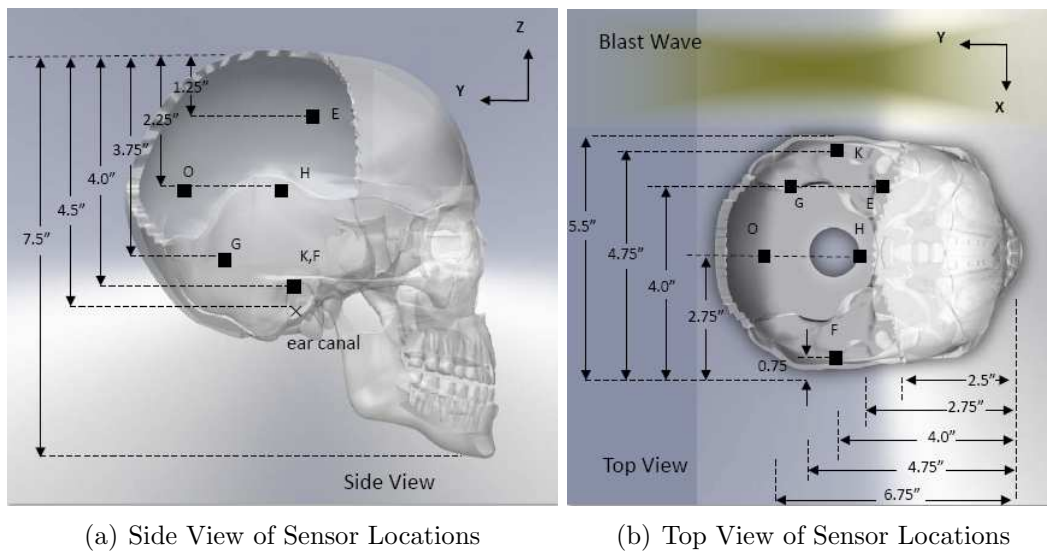
(a) Side View of Sensor Locations

(b) Top View of Sensor Locations

Figure 3-4: Manikin intracranial pressure sensor locations for second set of experiments

3.2.2 Computational Simulations

The DVBIC/MIT Full Head Model and extensions including protective equipment

In order to model the manikins, we adapted the DVBIC/MIT FHM and ACH-FHM described in Chapter 2. For this study, the air sinus was divided into an interior air sinus (within the skull) and an exterior air sinus (outside the skull). All of the intracranial structures (gray matter, white matter, CSF, interior air sinus, ventricles, glia, and venous sinus) were assigned the material properties of silicone gel. The skull was assigned the material properties of polyethylene, and all the extracranial structures (skin and fat, muscle, and exterior sinus) were assigned the material properties of silicone rubber.

Material models and properties

The manikin components were described using the simple viscoelastic material model described in Chapter 2. For the polyethylene skull, we used the Hugoniot equation of state. The material properties used for the skull, which were obtained from the literature, are given in Table 3.1.

Material	ρ (kg/m^3)	K (MPa)	G (MPa)	C_0	s	c_1	c_L
Polyethylene	900	1333	285.7	1850.0	0.94	0.6	0.8

Table 3.1: Material Properties for Polyethylene [146]

For the silicone gel in the intracranial cavity and the silicone rubber flesh outside the skull, we adopted the Tait equation of state. The material properties used for the head components, which were obtained from the literature, are given in Table 3.2.

Material	ρ (kg/m^3)	K (MPa)	G (MPa)	κ (Pa · s)	μ (Pa · s)	Γ_0	c_1	c_L
Sylgard	950	1000	0.0036	1000	1000	6.15	0.6	0.4
DragonSkin	1080	0.7032	.06330	1000	1000	6.15	0.6	1.0

Table 3.2: Material Properties for Sylgard [146] and DragonSkin [9, 81]

For the ACH, which consists of a Kevlar shell and foam pads, we used a neo-

Hookean elastic model. The material properties used for the Kevlar and foam components of the ACH are given in Table 2.1 in Chapter 2.

Computational Framework

Simulations of the experiments described in section 3.2.1 were conducted using the computational framework described in Chapter 2. The computational domain extended from -0.5 to 0.5 m in the x and y directions and from -0.0886 to 0.5 m in the z direction, with the center of the head model located at the origin. The fluid grid used two levels of subdivision, with an equivalent resolution of 1000 x 1000 x 580 grid points. 20 processors were used for the fluid solver, and 60 processors were used for the solid solver. The two blast conditions used correspond to free-field explosions of 0.057 kg pentolite at 0.71 and 1.1 m, resulting in peak incident overpressures of 236 and 102 kPa respectively. The simulations were run to a final time of 2.0 ms to evaluate the early-time response of the head.

3.3 Results

3.3.1 Round 1

In the initial set of experiments, head/neck manikins, both with and without the ACH, were exposed to free-field side blasts from 0.057 kg pentolite at 1.1 m. Simulations of these experiments were conducted with the modified FHM; snapshots of pressure contours from the unhelmeted head and ACH simulations are shown in Figs. 3-5 and 3-6 respectively. In both the experiments and the simulations, pressure traces were recorded at the locations of three intracranial sensors: E, G, and N. For each sensor, the pressure profiles were normalized to the peak pressure from the unhelmeted head experiment. In the absence of external or surface pressure data for this set of experiments, the pressure profiles were shifted in time such that the average arrival time for the three sensors was identical in the experiments and simulations.

Fig. 3-7 shows the pressure histories at sensor E for the head and helmet simula-

tions compared to the respective experimental results. For the head, the numerical peak pressure magnitude is within 4.4% of the experimental peak pressure magnitude, and the numerical peak pressure arrival time is within 6.7% of the experimental peak pressure arrival time. The pressure-time curves from the experiment and simulation exhibit similar rise and decay times; the primary discrepancy between the two curves is that the simulation does not capture some of the high-frequency oscillations observed in the experiment. For the ACH experiment and simulation, there is a 91% difference in the peak pressure magnitudes and a 26% difference in the peak pressure arrival times. The curves from the experiment and simulation both feature one broad peak with some oscillations, although there is some negative (tensile) behavior in the simulation after 0.76 ms that is not observed in the experiment.

For both the experiments and the simulations, the ACH curves display a longer rise time and lower peak pressure magnitude than the unhelmeted head curves. For example, in the simulation, the peak pressure for the ACH occurs 0.18 ms after the peak pressure for the unhelmeted head, and in the experiment, the peak pressure for the ACH occurs 0.29 ms after the peak pressure for the unhelmeted head. Further, in the simulation, the ACH peak pressure magnitude is 29% lower than the unhelmeted head peak pressure magnitude, and in the experiment, the ACH peak pressure magnitude is 61% lower than the unhelmeted peak pressure magnitude.

Fig. 3-8 shows the pressure histories obtained from the simulations and experiments at sensor G. For the unhelmeted head, there is a 27% difference in the peak pressure magnitudes and an 18% difference in the peak pressure arrival times from the experiment and simulation. For the ACH, there is a 2.1% difference in the peak pressure magnitudes and a 3.7% difference in the peak pressure arrival times from the experiment and simulation. For both the unhelmeted head and ACH, the pressure-time curves from the simulation and experiment have similar rise and decay times, although in the case of the ACH, we again observe tensile behavior after 0.75 ms in the simulation that is not observed in the experiment.

Fig. 3-9 shows the pressure histories at sensor N. For the unhelmeted head, the experiment features an initial peak followed by a double peak, with all three peaks
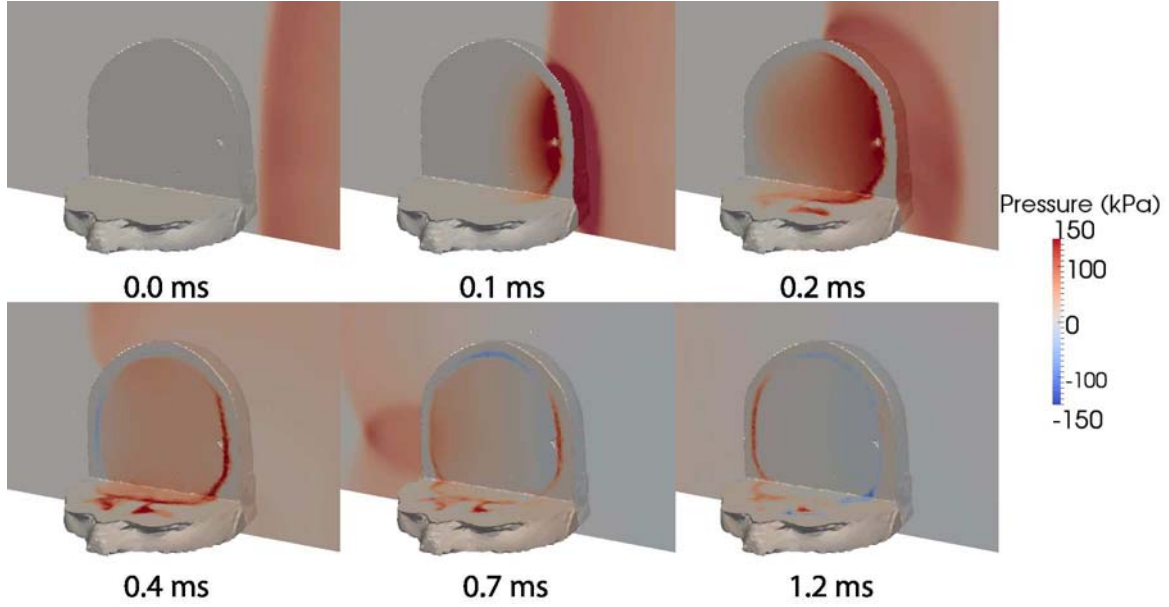
Figure 3-5: Snapshots showing the time evolution of pressure contours from the unprotected head simulation
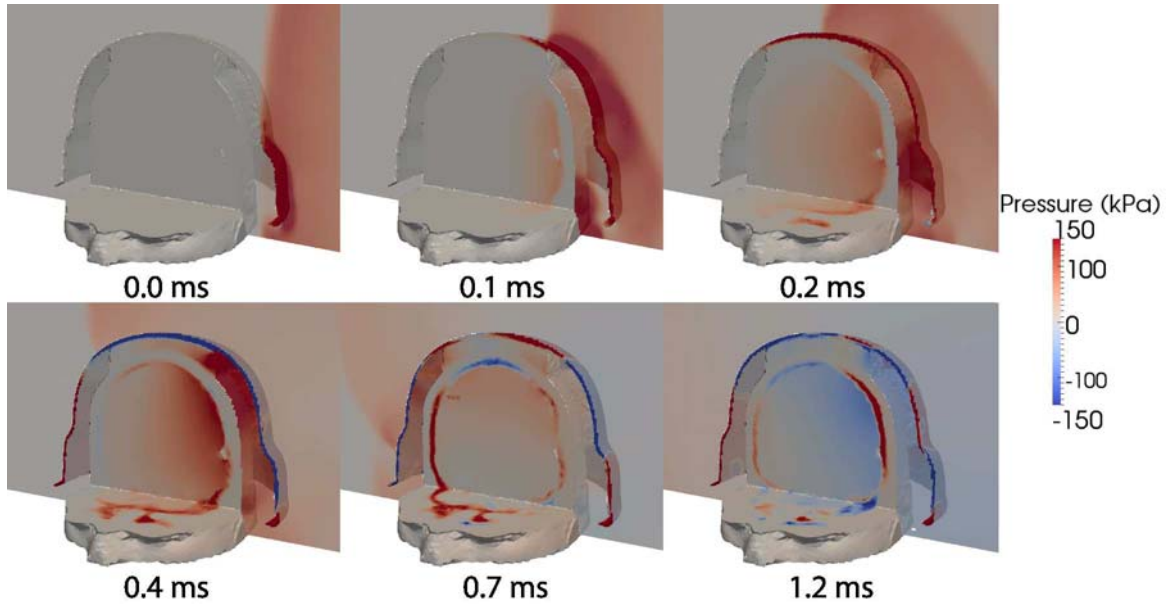
Figure 3-6: Snapshots showing the time evolution of pressure contours from the helmeted head simulation
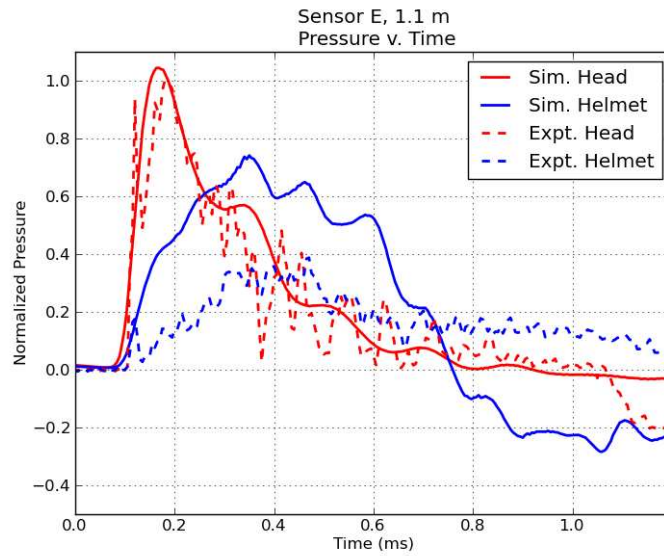
Figure 3-7: Comparison of pressure profiles at intracranial sensor E in the simulation and experiment, both with and without the ACH
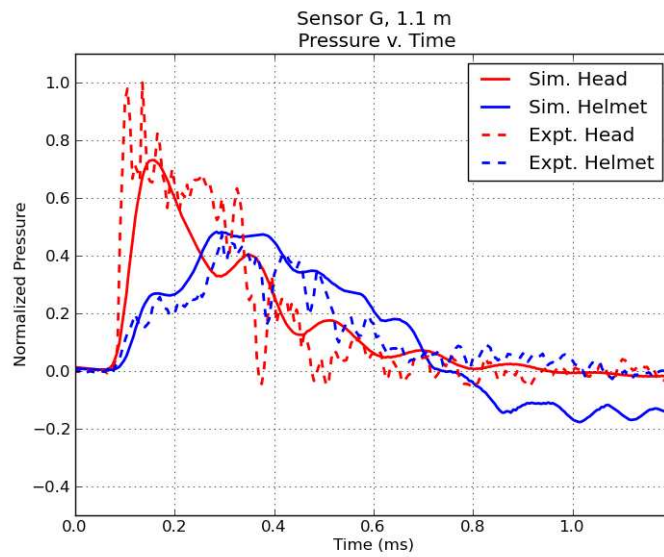
Figure 3-8: Comparison of pressure profiles at intracranial sensor G in the simulation and experiment, both with and without the ACH
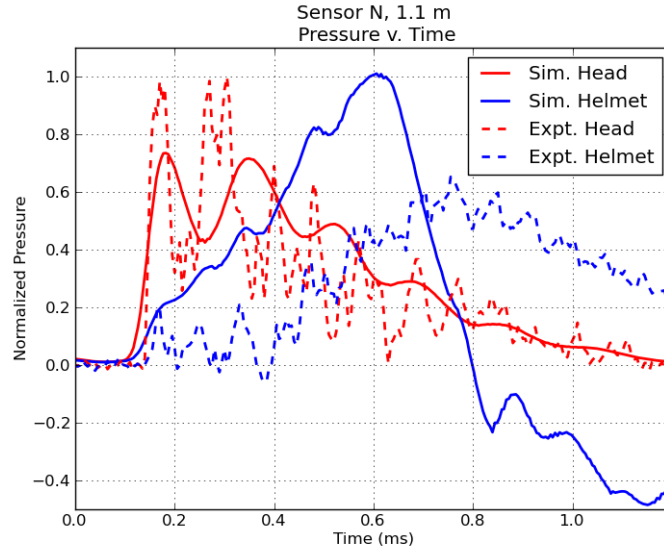
Figure 3-9: Comparison of pressure profiles at intracranial sensor N in the simulation and experiment, both with and without the ACH

having approximately the same magnitude. Similarly, the simulation features an initial peak followed by another peak of approximately the same magnitude. Comparing the initial pressure peaks from the simulation and experiment for the unhelmeted head, we find a difference in magnitude of 25% and a difference in arrival time of 7.1%. Comparing the maximum of the double peak from the experiment with the second peak from the simulation, we find a difference in magnitude of 28% and a difference in arrival time of 15%. For the ACH, the pressure histories from the experiment and simulation at sensor location N exhibit behaviors similar to those observed at sensor locations E and G; the pressure histories from the experiment and the simulation both feature one broad peak, and tensile behavior is observed after 0.8 ms in the simulation but not in the experiment. Comparing the peak pressure magnitudes from the simulation and experiment for the ACH, we find a difference of 55%, and comparing the peak pressure arrival times, we find a difference of 20%.

3.3.2 Round 2

In the second round of experiments, our collaborators at Carderock exposed head/neck manikins, both with and without the ACH, to free-field side blasts from 0.057 kg pen-

tolite charges at standoff distances of 0.71 and 1.1 m. We then conducted simulations of the experiments using the modified FHM. For each sensor, pressure profiles were normalized to the peak pressure from the unhelmeted head experiment. For this round of experiments, data from some external sensors was available, allowing us to evaluate whether we were accurately capturing the loading conditions of the experiments. The pressure profiles were shifted in time such that time zero occurred when the peak pressure arrived at external sensor B.

0.71 m

We first consider the results from the simulations and experiments conducted at a standoff distance of 0.71 m. At external sensor B, which measured the free-field pressure, the peak overpressure in the head simulation is 9.4% lower than in the head experiment, and the peak overpressure is 17% lower in the ACH simulation than in the corresponding experiment. At surface pressure sensor C, the simulation underpredicts the peak pressure by 37% in the case of the head and 46% in the case of the helmet.

Figure 3-10: Comparison of pressure profiles at the external sensors in the simulation and experiment conducted at 0.71 m standoff distance

We next consider three representative intracranial sensors: E, G, and K. At sensor E, we find that for the unhelmeted head, the peak pressure from the simulation is 22% lower and occurs 19% later than the peak pressure from the experiment. For the

81

(a) Sensor E   (b) Sensor G   (c) Sensor K

Figure 3-11: Intracranial sensors, 0.71 m. The pressure profiles for the unprotected head are in red, and those for the ACH are in blue. The solid lines represent the simulation results, and the dashed lines represent the experimental results.

ACH, the peak pressure from the simulation is 54% higher and occurs 31% later than the peak pressure from the experiment. At sensor G, for the unhelmeted head, the peak pressure from the simulation is 15% lower and occurs 26% earlier than the peak pressure from the experiment. In the experiment, the pressure-time curve features an initial peak consisting of two peaks of approximately equal magnitude that occur 0.025 ms apart and a third peak at a higher magnitude that occurs 0.055 ms after the second peak. In the simulation, this is represented by a single peak that spans the width of the three peaks from the experiment, with a magnitude between the first two peaks and the third peak. The simulation captures the overall shape of the curve, but it does not capture the high-frequency characteristics. For the ACH, the pressure-time curve from the experiment features three peaks and an additional double peak that all have magnitudes within 6.4% of each other. In the simulation, there are three peaks that vary in magnitude by up to 36% and span the width of the five experimental pressure peaks. Comparing the highest peak of the simulation with the closest peak from the experiment, we find a 25% difference in magnitude and a 3.0% difference in arrival time. At sensor K, for the unhelmeted head, the peak pressure magnitude is 36% lower in the simulation than in the experiment, and the peak pressure arrival time occurs 19% earlier in the simulation than in the experiment. For the ACH, the peak pressure is 35% higher and occurs 27% later in the simulation than in the experiment.

For all three sensors, in both the experiments and simulations, the peak pressure

magnitudes are significantly lower in the case of the ACH than in the case of the unhelmeted head. For example, at sensor G, in the simulation, the ACH peak pressure magnitude is 48% lower than the unhelmeted head peak pressure magnitude, and in the experiment, the peak pressure magnitude is 62% lower for the ACH than for the unhelmeted head.

1.1 m

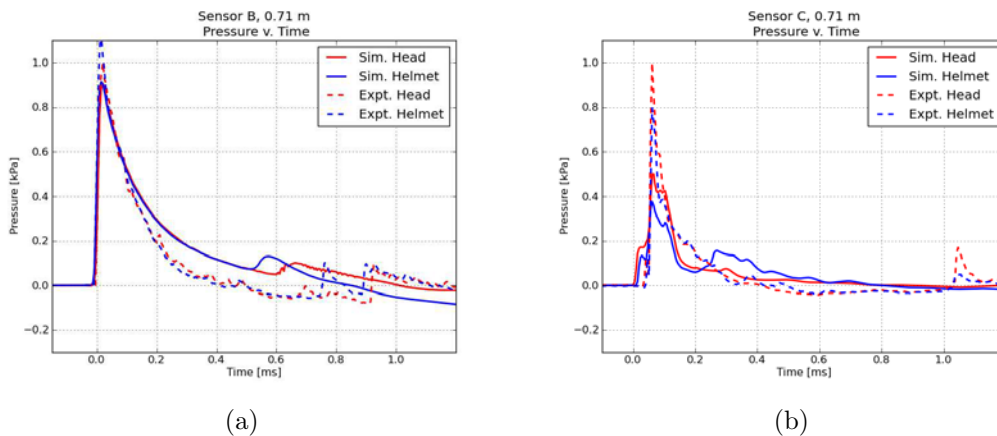(a)   (b)
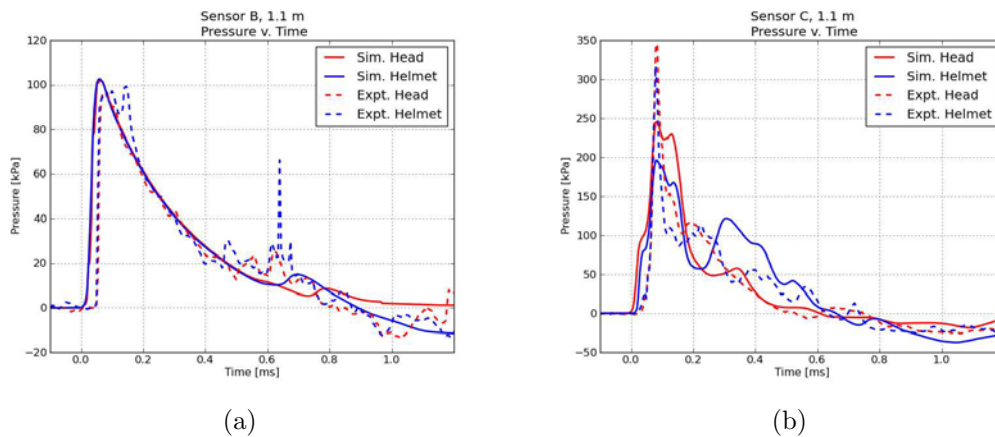
Figure 3-12: Comparison of pressure profiles at the external sensors in the simulations and experiments conducted at 1.1 m standoff distance

For the set of tests conducted at a standoff distance of 1.1 m, we first consider external sensor B. For the head, there is a 5.7% difference between the peak pressure magnitudes from the simulation and experiment, and for the helmet, there is a 3.3% difference. Looking at surface pressure sensor C, we find that the simulation underpredicts the peak pressure magnitude for the head by 10% and for the helmet by 21%.

We next consider representative intracranial sensors. At sensor E, we find that for the unhelmeted head, the peak pressure from the simulation is 42% higher and occurs 44% later than the peak pressure from the experiment. For the ACH, the peak pressure is 140% higher and occurs 97% later in the simulation compared to the experiment. At sensor G, for the unhelmeted head, the simulation underpredicts the peak pressure magnitude by 38%, and the peak pressure arrival time occurs 39%
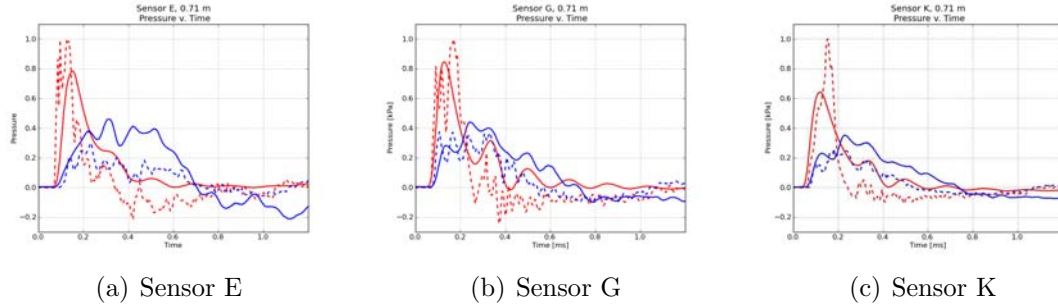
|(a) Sensor E|(b) Sensor G|(c) Sensor K|
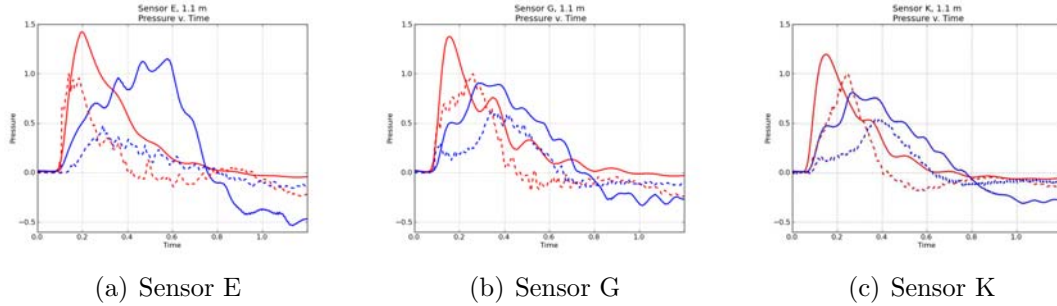
Figure 3-13: Intracranial sensors, 1.1 m. The pressure profiles for the unprotected head are in red, and those for the ACH are in blue. The solid lines represent the simulation results, and the dashed lines represent the experimental results.

earlier in the simulation than in the experiment. In the case of the helmet, the simulation overpredicts the peak pressure by 47%, and the peak pressure occurs 17% earlier in the simulation than in the experiment. At sensor K, in the case of the unhelmeted head, the simulation overpredicts the peak pressure magnitude by 20%, and the peak pressure arrival time occurs 37% earlier. In the case of the helmet, the simulation overpredicts the peak pressure magnitude by 51%, and the peak pressure arrival time occurs 27% earlier.

We again observe that for all three intracranial sensors, in both the experiments and the simulations, the peak pressures for the ACH are lower and occur later than the peak pressures for the unhelmeted head. For example, at sensor K, in the simulation, the peak pressure for the ACH is 32% lower and occurs 75% later than the peak pressure for the unhelmeted head. In the experiment, the peak pressure for the ACH is 46% lower and occurs 51% later than the peak pressure for the unhelmeted head.

3.4   Discussion

In this chapter, we compared simulation results with data from free-field blast experiments involving head/neck manikins. In the first set of experiments and simulations, the percent difference between the head experiments and simulations ranged from 4.4 to 28% for peak pressure magnitude and from 6.7 to 18% for peak pressure arrival time. The percent difference between the ACH experiments and simulations ranged

from 2.1 to 91% for peak pressure magnitude and from 3.7 to 26% for arrival time. In the second round, the percent difference in peak pressure magnitude for the external sensor, which provided an indicator of the level of success in modeling the free-field blast wave from the experiments, ranged from 3.3 to 17%. For the intracranial pressure sensors, the percent difference in peak pressure magnitude ranged from 15 to 42% for the head and from 25 to 140% for the helmet. The percent difference in peak pressure arrival time ranged from 19 to 44% for the head and from 3.0 to 97% for the helmet.

In general, the simulations were able to capture the overall intensity of the physical human head surrogate's blast response. In some cases, the simulations were able to closely match many of the characteristics of the experimental pressure profiles, including the maximum amplitudes, arrival times, rise and decay times, and overall shapes of the pressure peaks. For example, at sensor E in the unhelmeted head in the first round of experiments, the difference in experimental and computational peak pressure magnitudes was 4.4%, and the two pressure profiles were similar in terms of peak width and arrival time, although the simulation did not capture some of the high-frequency oscillations observed in the experiment. Similarly, at sensor G in the helmeted head in the first round of experiments, the difference in experimental and computational peak pressure magnitudes was 2.1%, and the two pressure profiles were similar in terms of peak width and arrival time, although the simulation exhibited some tensile behavior after 0.75 ms that was not observed in the experiment. In most of the other cases, the discrepancies between the experimental and computational pressure profiles were more significant. On average, the difference between experimental and numerical peak pressure magnitudes was 26% for the unhelmeted head and 56% for the helmeted head. And in some cases, the differences were substantially higher. For example, at sensor E in the helmeted head at the 1.07 standoff distance in the second round of experiments, the difference between experimental and numerical peak pressure magnitudes was 140%.

There are a number of potential sources of these discrepancies between the experimental and numerical results, including differences in the geometries of the manikin

head used in the experiments and the computational FHM used in the simulations, lack of experimental measurements of the material properties of the head/neck manikin components, and uncertainty about sensor placement within the manikins. In addition, some of the discrepancies in the helmet simulations may be due to the boundary conditions between the pads and the surface of the head. Given the variability of contact conditions between helmets and heads, and given the lack of information on friction coefficients, for simplicity we assumed that the meshes were conformal; that is, the helmet pad and head meshes could not slide with respect to each other. This may explain both why the peak pressures observed in the helmet simulations were consistently higher than those in the experiments and why negative pressures were observed in the helmet simulations but not in the experiments. Additionally, an explanation for the high-frequency oscillations that were often observed in pressure profiles from experiments but not simulations may be related to the nature of the pressure gauges; it is possible that the sensors, which were embedded in silicone gel, may have been affected by their own dynamic response to the passing blast wave.

Despite the sometimes significant discrepancies between the experimental and numerical results, we believe that the level of validation achieved is sufficient for the purposes of this thesis, given the current state-of-the-art modeling capabilities presented in this thesis. Further improvements would require additional efforts to quantify and reduce uncertainty in both the models and the experiments that are beyond the scope of this thesis.

This work also represents the first validation effort to incorporate the ACH, allowing us to begin investigating the effects of the ACH on the mechanical response of the human head to blasts. From the results presented in this chapter, we can see that in both the experiments and the simulations, intracranial pressures for the helmeted head were consistently lower than those for the unprotected head. At the 0.71 m standoff distance, the average difference between the peak pressure magnitudes for the helmeted and unhelmeted head was 45% in the simulations and 69% in the experiments. At the 1.1 m standoff distance, the average difference was 28% in the simulations and 47% in the experiments. The results suggest that the ACH is

able to somewhat mitigate the effects of primary blast waves on the human head. A more detailed discussion of the blast protection performance of the ACH is given in Chapter 5.

Chapter 4

Validation: Live Pig and Human Cadaver Tests

4.1   Introduction

Blast injury tests cannot be conducted on live humans, so experiments are instead conducted on physical surrogates, animals, and human cadavers. While experiments conducted on physical surrogates, such as those described in Chapter 3, allow researchers to investigate blast effects while avoiding undue animal experimentation, experiments conducted on biological specimens, particularly live animals, are needed to understand the response of biological tissue to blasts. A number of experimental studies have begun investigating the effects of blasts on animals, including rats, rabbits, pigs, and monkeys [25, 106, 13, 76]. Pigs have proved particularly useful for investigating blast-induced TBI due to similarities between pigs and humans in terms of body mass and brain architecture [102]. In one study, Bauman et al. exposed 175 pigs equipped with torso-protecting armor to a variety of blast environments and observed outcomes including vasospasm, white matter fiber degeneration and astrocytosis, inflammatory injury, and disruptions in neurologic function [13]. In another experimental study, Suneson et al. found that exposing pigs to a high-explosive blast resulted in transient depression of cortical activity and short-lasting apnea, indicating a possible effect on the brainstem [119].

However, there have been few studies to date comparing simulation results with data from experiments exposing biological specimens to blasts. In one study, Teland et al. exposed pigs to low-level blasts and conducted simulations using a rudimentary two-dimensional porcine head model [124]. In the experiments, anesthetized pigs received three consecutive exposures to a 23-30 kPa blast that resulted from firing either a 12.7 mm anti-materiel rifle or a 155 mm Howitzer. The simulations were conducted using a porcine head model that consisted of a skull modeled as an elliptical surface and a brain modeled as a solid ellipse, with an elastic material model used for both the skull and the brain. Pressure profiles at a location within the brain were obtained from the simulations and experiments; while there was no direct comparison of experimental and simulation results provided, the pressure profiles appeared to be in general agreement. Recently, Zhu et al. conducted a study involving a more accurate computational pig head model [145]. In that study, the porcine head model was developed from CT and MRI images, and it consisted of a skull, brain, CSF, dura, and pia; the skull was modeled as a linearly elastic material, the brain tissues and CSF were modeled using a viscoelastic model, and the pia and dura mater were modeled as thin shell elements that were assumed to be linearly elastic. Simulations and experiments were conducted in which the pigs were exposed to side blasts from a shock tube using 0.48 and 0.61 kg TNT. Comparing the intracranial pressures at rostral, caudal, and medial locations within the brain, they found that the simulated peak intracranial pressures were within 12% of the experimental values. In addition to these two pig studies, another study conducted simulations and experiments exposing rats to a frontal blast with an overpressure of 85 kPa [144]. That study found that the simulations underpredicted the peak positive pressures by 2-7% and the pulse widths by 15-18%.

In this chapter, we present a collaborative effort to validate our computational framework using results from shock tube experiments involving pigs and a human cadaver that were conducted by researchers at Duke University. In a comprehensive validation effort, we compare simulation results with data from live pig experiments conducted at five different blast conditions, a pig cadaver experiment, and human

cadaver experiments. In Chapter 3, we compared data from experiments and simulations that exposed physical human head surrogates to blasts. In this chapter, we investigate the ability of the computational framework to describe the blast response of not just engineering materials, but biological tissues. To that end, we conducted simulations using three-dimensional, biofidelic human and porcine computational head models, and we compared metrics of mechanical blast response, including intracranial pressure and strain histories, from the experiments and simulations.

4.2 Experiments

4.2.1 Pig Experiments

In this section we summarize the experiments, which were conducted by our collaborators at Duke University and reported in [118]. The experiments were conducted using a 305-mm diameter shock tube consisting of a driver section separated from a driven section by a diaphragm. The compressed-gas shock tube generated planar shock waves representative of free-field blasts from high explosives, with the overpressure and positive phase duration of the shock waves controlled by varying the diaphragm thickness and the driver section length. Overpressure was measured by three flush-mounted pressure transducers (Endevco 8530B, San Juan Capistrano, CA) evenly spaced around the tube circumference 6.35 mm interior to the tube exit. The transducers were oriented such that they recorded incident (side-on) pressure.

Condition	Incident Overpressure (kPa)	Duration (ms)	Number of Tests
1	230	5.00	1
2	234	2.63	2
3	260	3.56	1
4	274	6.53	4
5	514	2.93	3

Table 4.1: Blast Conditions for Live Pig Experiments

Eleven live, anesthetized Yorkshire pigs (*Sus scrofa*) with an average body mass of 60.97 ± 11.18 kg were exposed to side blasts from the shock tube. The five blast
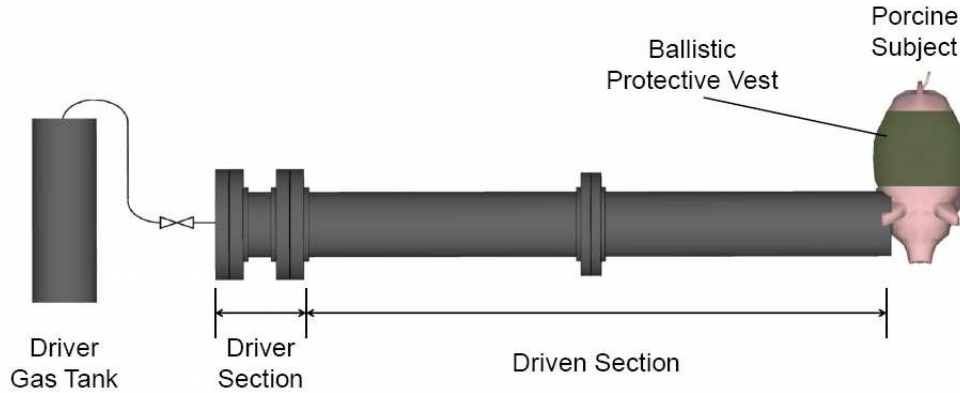
Figure 4-1: Schematic of the experimental setup (source: [118]). The porcine subjects were positioned such that the shock wave from the shock tube impinged on the right temporal region of the head.

conditions are shown in Table 4.1. In addition, one cadaveric pig with a mass of approximately 70 kg was exposed to a 514 kPa, 2.93 ms side blast, and three pigs were tested as controls without a blast. The incident overpressures and positive duration values were selected to approximately correspond to a 50% injury risk for brain hemorrhage and pulmonary injury in a ferret model scaled to porcine exposure [107]. The overpressures were comparable to survivable blasts produced by 105 and 155 mm artillery rounds at a range of 1-5 m and up to 50 kg of TNT-equivalent high explosive at a range of 7-10 m [118].

Fig. 4-1 illustrates the experimental setup. Each pig was restrained and positioned such that the axial centerline of the shock tube was perpendicular to the right temporal bone and aligned with the surface pressure gauge located near the right ear. The distance from the center of the open face of the shock tube to the right surface pressure gauge was 5.34 ± 1.6 cm. In order to isolate the shock wave to the head, the pigs wore police-issue ballistic vests at NIJ Level-2 (PACA-2, Protective Apparel Corporation of America, Jacksboro, TN, USA) without the hard ceramic inserts, protecting the thorax, and the pigs were positioned such that the thorax was not directly exposed to the shock wave.

External pressure was measured using three surface pressure gauges (LQ-125, Kulite Semiconductor Products Inc., Leonia, NJ, USA) sutured to the skin surface.

One gauge was located at the intersection of the nuchal crest and the midsagittal plane (crown surface pressure sensor), and the other two were located 1 cm anterior to the vertex of each ear (right and left surface pressure sensors). Intracranial pressure (ICP) was measured using catheter pressure transducers (SPR-524, Millar Instruments, Inc., Houston, TX) inserted through three 4-mm holes in the skull. One sensor was located 2.39 ± 0.30 cm anterior to the nuchal crest in the midsagittal plane (crown ICP), one sensor was located 2.41 ± 0.26 cm anterior to the nuchal crest and 2.29 ± 0.49 cm lateral to the midsagittal plane (right ICP), and one sensor was located 2.39 ± 0.328 cm anterior to the nuchal crest and 2.51 ± 0.43 cm lateral to the midsagittal plane (left ICP).

4.2.2 PMHS Experiments

In addition to the porcine subjects, a post mortem human subject (PMHS) was exposed to blasts from the shock tube. Our collaborators at Duke subjected the PMHS to frontal and side blasts at two blast conditions; in the first, a membrane thickness of 20 mil resulted in an incident overpressure of 130 kPa and a positive duration of 0.52 ms, and in the second, a membrane thickness of 40 mil resulted in an incident overpressure of 197 kPa and 0.72 ms. For each of the four sets of conditions, three repeated tests were conducted.

Three pressure sensors were located on the surface of the PMHS head. One sensor was located at the vertex of the head (crown surface pressure sensor), one was located 2 cm superior to the intersection of the Frankfurt plane and the midsagittal plane (front surface pressure sensor), and one was located 5 cm superior to the intersection of the Frankfurt plane and the midcoronal plane (side surface pressure sensor). Intracranial pressure was measured at three locations within the PMHS head. One pressure sensor was located at the intersection of the midcoronal and midsagittal planes at a depth of 2 cm (crown ICP), one was located 2 cm superior to the nasion in the midsagittal plane at a depth of 2 cm (front ICP), and one was located 5 cm superior to the intersection of the intersection of the midcoronal and Frankfurt planes at a depth of 8 cm (midbrain ICP).

4.3 Computational Simulations

4.3.1 Porcine Head Simulations

Computational Porcine Head Model

A three-dimensional, biofidelic computational model of a porcine head was generated from CT images available from the Virtual Pig Project at Ohio University. Using Amira, the CT images were segmented into four distinct materials: brain, soft tissue, eye, and skull. A solid model was then generated and imported into Ansys ICEM CFD, which was used to generate a finite element mesh consisting of 91,778 tetrahedral elements. This mesh, which is shown in Fig. 4-2, includes a nasal cavity that is filled by the fluid domain during simulations and large ears that were partially reconstructed because they extended beyond the original CT images.

In preliminary simulations, the ears experienced significant deformation. Since the large, reconstructed ears were not critical for the purpose of the current study, we used a slightly smaller, simplified computational mesh that did not contain the reconstructed ears. The simplified mesh, which is shown in Fig. 4-3, consists of three distinct materials – brain, soft tissue, and skull – and has 74,337 quadratic tetrahedral elements.

Material Models and Properties

The mechanical response of the porcine brain was described using the Socrate brain tissue constitutive model described in Chapter 2 and the material model parameters presented in Table 2.4. The skull and soft tissue were modeled using the simple viscoelastic model described in Section 2.3.2, using the Hugoniot and Tait equations of state respectively. The material model parameters for the skull are given in Table 2.2, and the parameters for soft tissue are given in Table 4.2.

Material	ρ (kg/m^3)	K (GPa)	G (GPa)	κ (Pa $\cdot$ s)	μ (Pa $\cdot$ s)	Γ_0	c_1	c_L
Soft Tissue	1100	3.48	0.588	1000	1000	6.15	0.4	0.6

Table 4.2: Material Properties for Porcine Soft Tissue
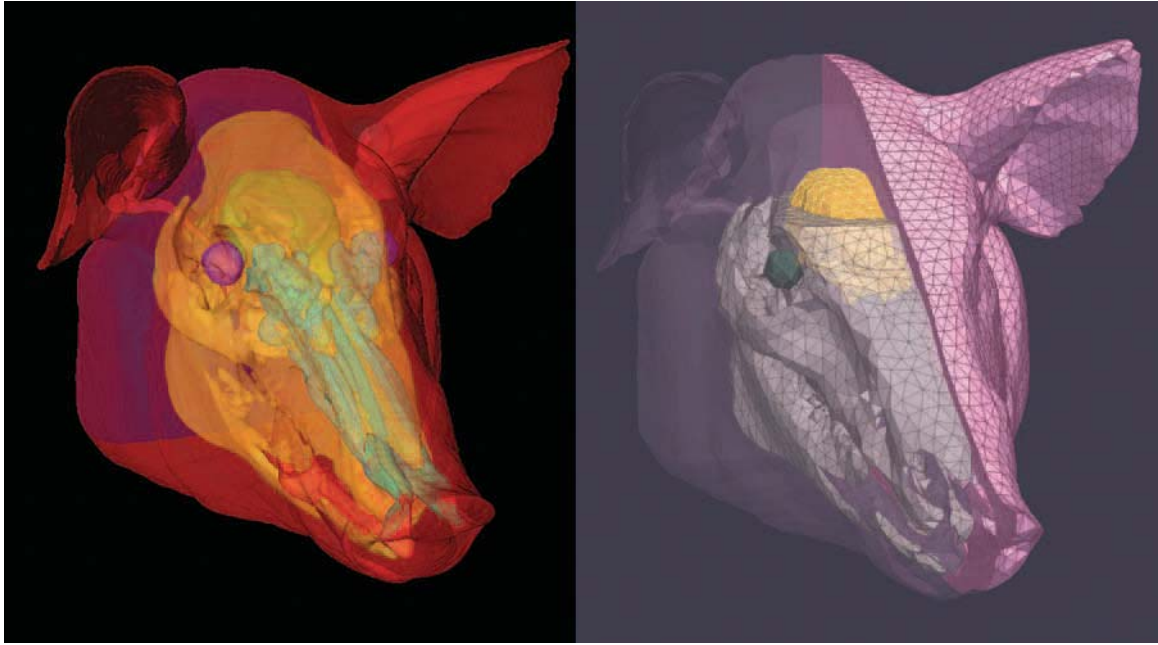
Figure 4-2: The full pig head model. On the left are the solid surfaces generated by segmentation of the CT data set, and on the right is the computational mesh with details of the internal model components.
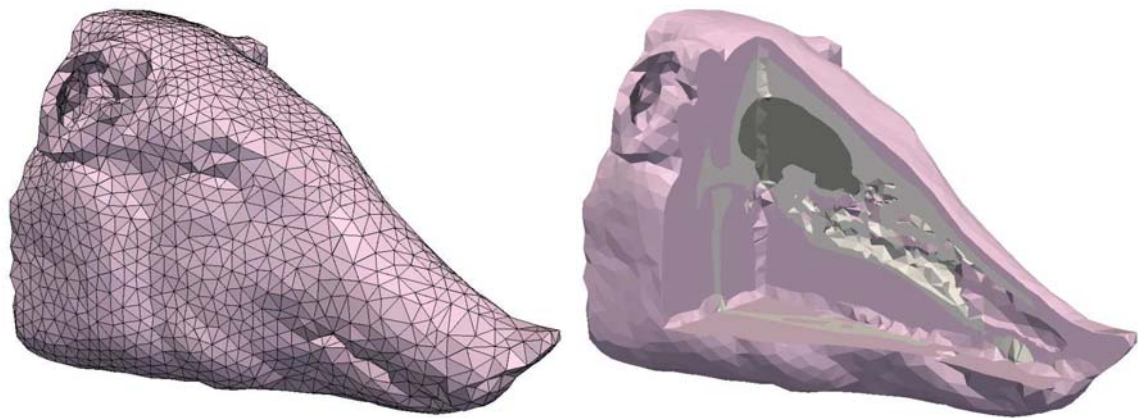
(a) Computational Pig Head Mesh   (b) Interior of Pig Head Model

Figure 4-3: The simplified porcine head computational mesh used in this study: (a) a view of the exterior of the mesh and (b) a combined sagittal, coronal, and axial cut showing the interior of the model. The soft tissue is represented as pink, the skull as white, and the brain as gray.
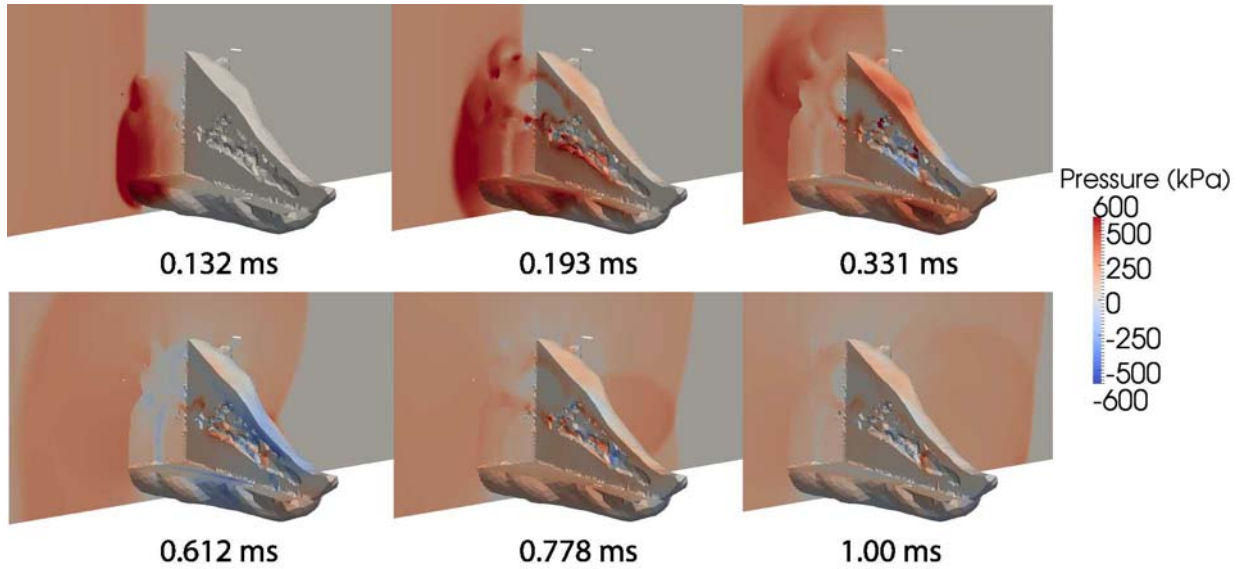
Figure 4-4: Snapshots of the time evolution of the pressure response from the porcine head simulation at blast condition 4 (see Table 4.1).

Simulation Loading Conditions

In the simulations of the tests described in Section 4.2.1, the computational domain extended from -0.6 to 0.6 m in the x and y directions and from -0.1180 to 0.5 m in the z direction. The center of the porcine head model was located at the origin. The fluid grid used two levels of subdivision, with an equivalent resolution of 1200 x 1200 x 620 grid points. 20 processors were used for the fluid solver, and 50 processors were used for the solid solver. Instead of modeling the shock tube, which was used in the experiments to reproduce a free-field blast, we modeled a spherical blast wave. The blast front was initialized such that the peak incident overpressure and positive duration matched the values listed in Table 4.1. Representative snapshots of the pressure contours from the 274 kPa, 6.53 ms simulation (blast condition 4) are shown in Fig. 4-4.

4.3.2   PMHS Head Simulations

The DVBIC/MIT Full Human Head Model presented in Chapter 2 was used in the PMHS simulations described in this chapter. The computational domain extended from -0.6 to 0.6 m in the x and y directions and from -0.0876 to 0.5 m in the z

direction, with the center of the human head located at the origin. The fluid grid used two levels of subdivision, with an equivalent resolution of 1200 x 1200 x 580 grid points. 20 processors were used for the fluid solver, and 60 processors were used for the solid solver. The blast front was initialized such that the peak incident overpressure and positive duration matched the values described in Section 4.2.2.

4.4 Results

4.4.1 Live Pig Tests

The first step in the validation process involves comparing external pressure histories from the experiments and simulations to evaluate the ability of the computational framework to describe the external blast wave. In the experiments, external overpressure was measured by three pressure transducers that were located 6.35 mm interior to the shock tube exit and placed 120° apart. Fig. 4-5 compares external pressure histories from representative experiments at each blast condition with external pressure histories from the corresponding simulations. In the experiments, $t = 0$ is taken as the time when the sensors at the mouth of the shock tube experienced the onset of overpressure. For consistency, the equivalent time, rather than the time of detonation, is taken as time zero in the simulations.

From Fig. 4-5, we observe that in both the experiments and simulations, there is a rapid rise in pressure followed by an exponential decay; this is characteristic of the Friedlander waveform, which describes the pressure signature at a fixed point for an idealized free-field blast wave. The experimental and numerical pressure-time curves exhibit similar peak pressures and decay times, and the simulations generally appear to be able to capture the secondary peaks observed in the experiments due to reflection of the blast wave from the porcine head. The secondary peaks occur at three distinct times due to variations in porcine head geometry along the anteroposterior axis, since the three pressure transducers are located at different points along that axis. Discrepancies between secondary peak magnitudes and arrival times in the
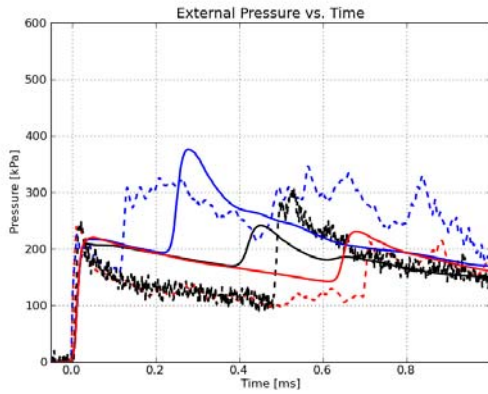
(a) Condition 1
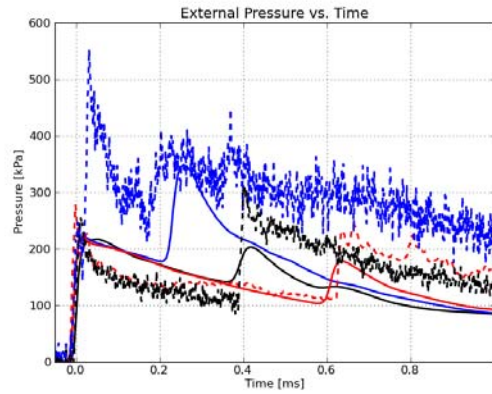
(b) Condition 2
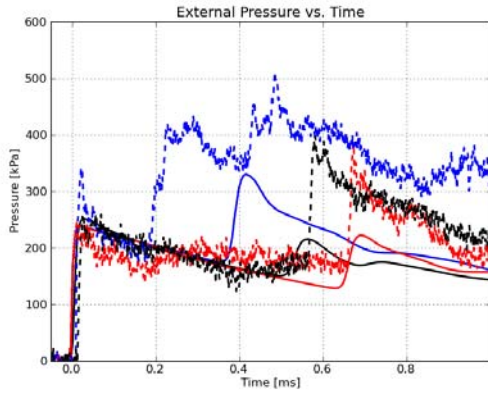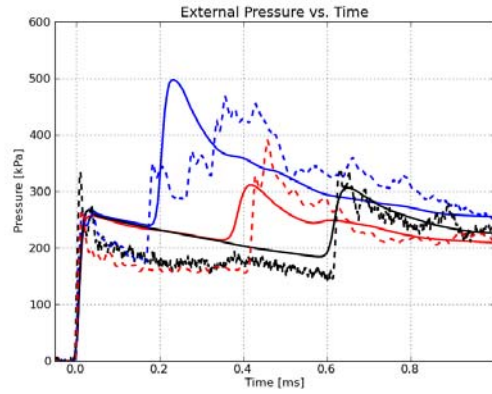
(c) Condition 3
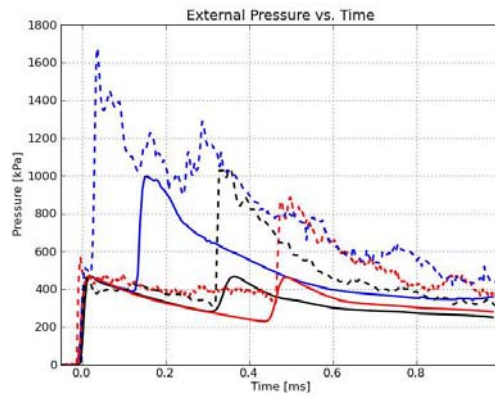
(d) Condition 4

(e) Condition 5

Figure 4-5: Comparison of external overpressures at the mouth of the shock tube from representative experiments and the corresponding simulations. The solid lines represent simulation results, and the dashed lines represent experimental results. Each color represents one of three pressure sensors evenly spaced around the mouth of the tube 6.35 mm interior to the shock tube exit.
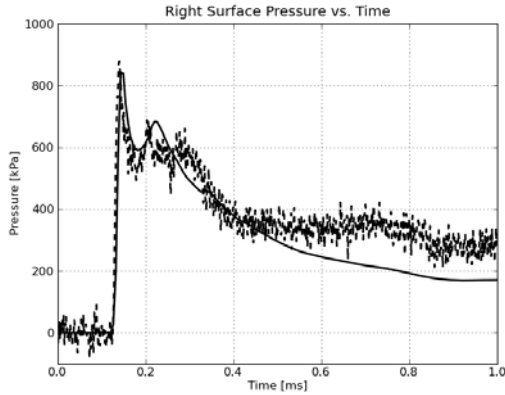
(a) Right Surface Pressure

(b) Crown Surface Pressure

Figure 4-6: Comparison of computational and experimental surface pressure profiles from blast condition 3 (see Table 4.1). The solid line represents simulation results, and the dashed line represents experimental results.

experiments and simulations may be attributable to differences in the head geometries of the live pig specimens and the computational mesh.

Condition	Expt. Pressure (kPa)	Sim. Pressure (kPa)	% Difference
1	233	216	-7.5
2	252	219	-13
3	281	243	-14
4	286	263	-8.3
5	521	468	-10

Table 4.3: Comparison of Peak Incident Overpressures from Porcine Experiments and Simulations

To assess the difference between experimental and computational results more quantitatively, the peak incident overpressures from the experiments and simulations at each blast condition are given in Table 4.3. The experimental pressures were averaged over the three sensors at the mouth of the shock tube, and if multiple tests were conducted at a given blast condition, the pressures were averaged over the tests. From Table 4.3, we see that all of the peak simulation overpressures are within 14% of the peak experimental pressures, and on average, the simulations underpredict the peak incident overpressures from the experiments by 11%.

In addition to the pressure transducers at the shock tube exit, pressure sensors were located at the surface of the porcine head and within the intracranial cavity. For

each blast condition where experimental data from the right surface pressure sensor was available, the surface and intracranial pressure histories from the experiments and simulations were temporally aligned at the onset of overpressure at the right surface sensor. Since usable experimental data from the right surface pressure sensor was not available for condition 1, the surface and intracranial pressure histories for that condition were instead aligned using the onset of overpressure at the mouth of the shock tube.

The right surface pressure gauge measured reflected overpressure. From Fig. 4-6(a), which compares the right surface pressure profiles from the experiment and simulation at blast condition 3, we observe in both curves a sharp rise to the peak pressure, followed by a secondary peak and exponential decay. The peak pressure magnitude from the simulation, 843 kPa, is within 4.1% of the experimental peak pressure magnitude, 880 kPa.

Fig. 4-6(b) also compares the crown surface pressure profiles from the experiment and simulation for blast condition 3. We see that the pressure profiles have similar shapes, although the peak pressure in the simulation, 233 kPa, is 90% higher than the peak pressure in the experiment, 123 kPa. The arrival time in the simulation, 0.248 ms, is also 0.024 ms earlier than the arrival time in the experiment, 0.272 ms. One explanation for the discrepancy in pressure magnitudes may be that the crown surface pressure sensor was mounted on skin, which is an extremely compliant surface, in the experiment. The orientation of the pressure sensor may be another source of discrepancy.

Condition	Expt. Peak Pressure (kPa)	Sim. Peak Pressure (kPa)	% Difference
1	251	267	+6.2
2	144	113	-21
3	195	210	+7.3
4	200	191	-4.4
5	228	202	-11

Table 4.4: Comparison of Peak Pressure at Right Intracranial Sensor from Porcine Experiments and Simulations

Fig. 4-7 compares the right intracranial pressure profiles from simulations and
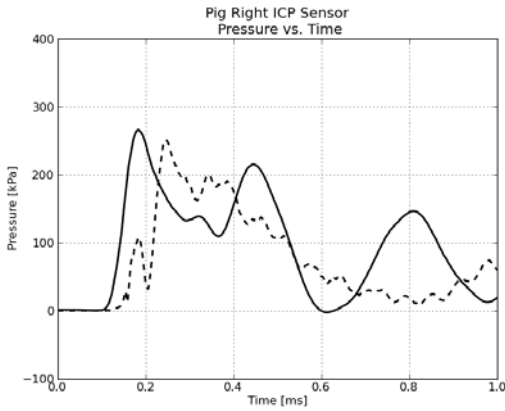
(a) Condition 1
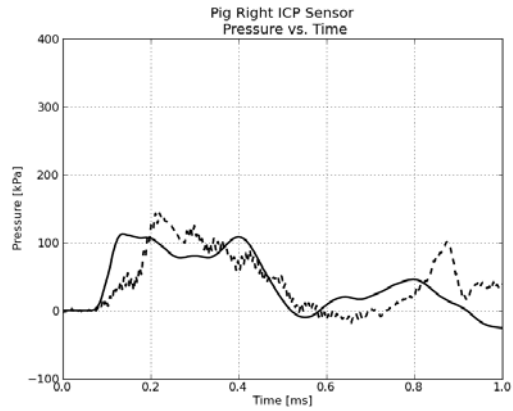
(b) Condition 2
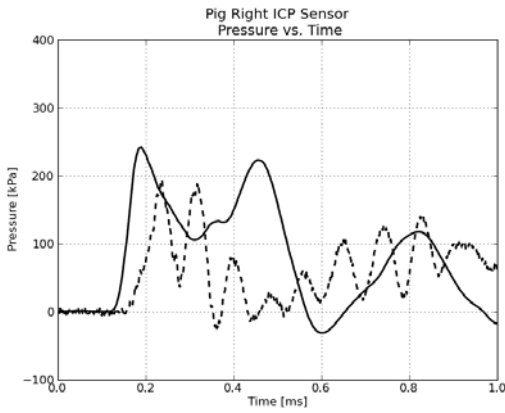
(c) Condition 3

(d) Condition 4

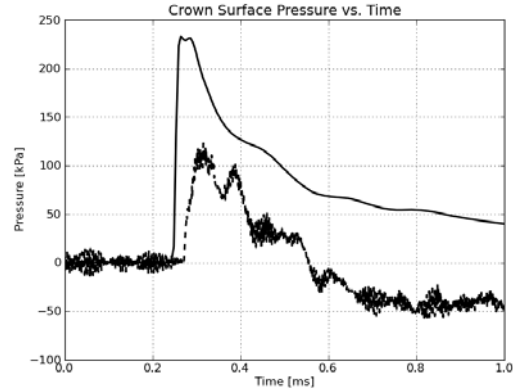(e) Condition 5

Figure 4-7: Comparison of computational and experimental pressure profiles at the right ICP sensor location. The solid lines represent simulation results, and the dashed lines represent experimental results.

experiments for the five blast conditions. From Fig. 4-7, we observe that the simulations were able to capture many of the significant features of the experiments. For example, for condition 1, we observe that the primary peak has similar rise times, arrival times, and magnitudes in the simulation and experiment. Additionally, in both the simulation and experiment, the primary peak is followed by a second peak of slightly lower magnitude. For all five blast conditions, the simulations provide a reasonable estimate of the overall intensity of the pressure response, although some of the high frequency oscillations observed in the experiments are not captured by the simulations. Even between the experiments, we can observe distinct variations in the shapes of the pressure profiles; this is likely because all the experimental specimens had unique head geometries that affected wave propagation and also because of the difficulty in placing pressure sensors in the same locations in each specimen. Despite the difficulty of capturing the blast response within biological specimens, we can see from Table 4.4 that the percent difference between the experiments and simulations ranges from 4.4 to 21%, and the average percent difference is 10%.

Condition	Expt. Peak Pressure (kPa)	Sim. Peak Pressure (kPa)	% Difference
1	225	260	+16
2	110	118	+7.5
3	148	168	+13
4	203	186	-8.8
5	324	362	+12

Table 4.5: Comparison of Peak Pressure at Crown Intracranial Sensor from Experiments and Simulations

Fig. 4-8 compares the crown intracranial pressure profiles from simulations and experiments for the five blast conditions. From Fig. 4-8, we again see that the simulations generally capture the shape of the experimental pressure profiles. For example, in condition 1, we see in both the simulation and experiment that there are two main peaks of comparable magnitude. This is a pattern we see again in condition 5, and to a lesser extent, in condition 3. From Table 4.5, we see that the percent difference ranges from 7.5 to 16%, and the average percent difference is 11%.

Fig. 4-9 compares the left intracranial pressure profiles from simulations and ex-
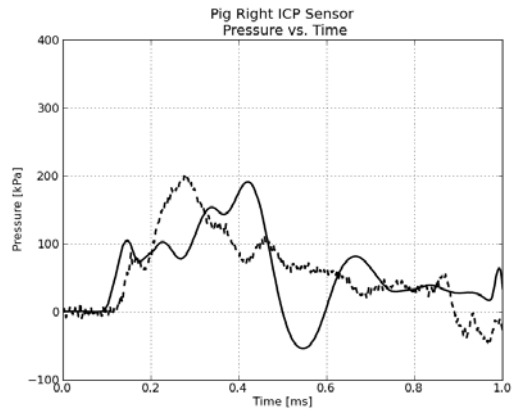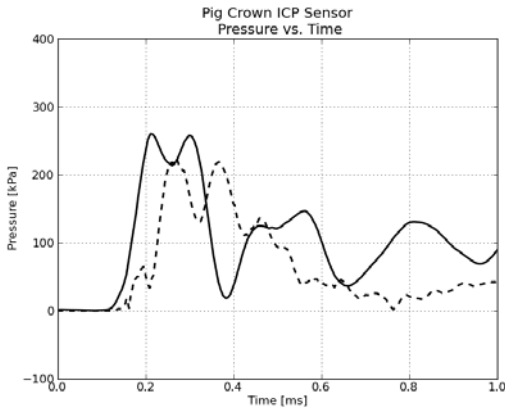
(a) Condition 1
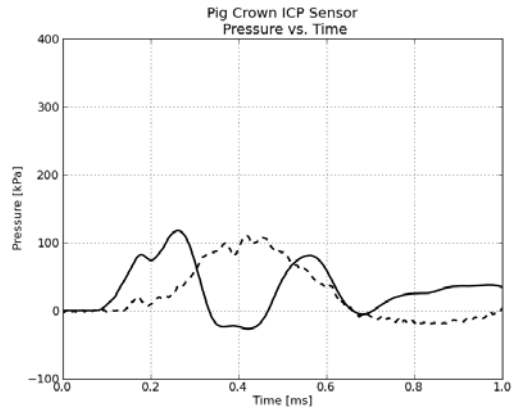
(b) Condition 2
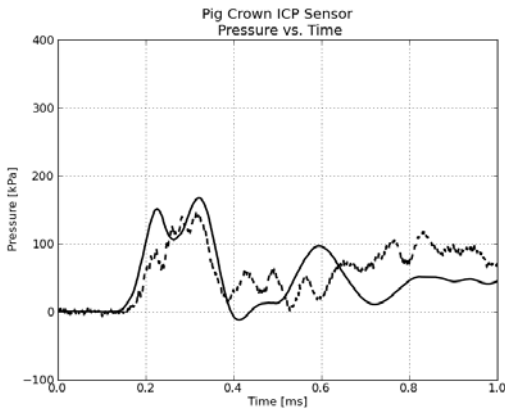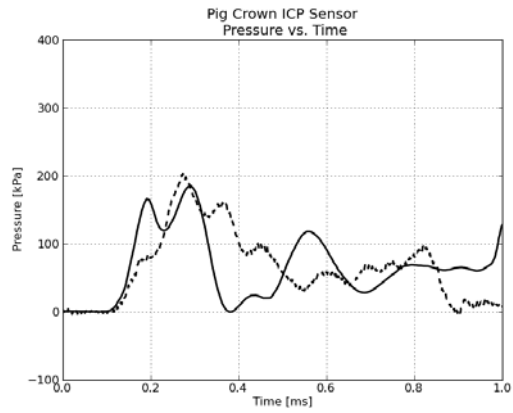
(c) Condition 3
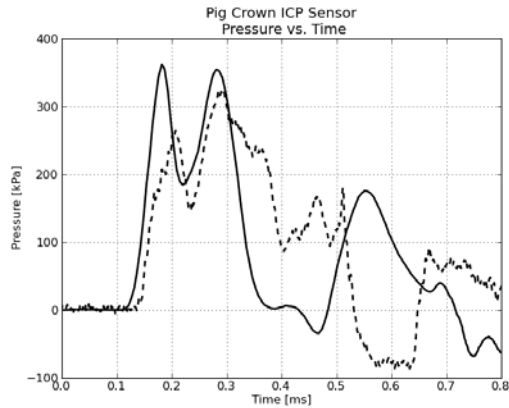
(d) Condition 4

(e) Condition 5

Figure 4-8: Comparison of computational and experimental pressure profiles at the crown ICP sensor location. The solid lines represent simulation results, and the dashed lines represent experimental results.
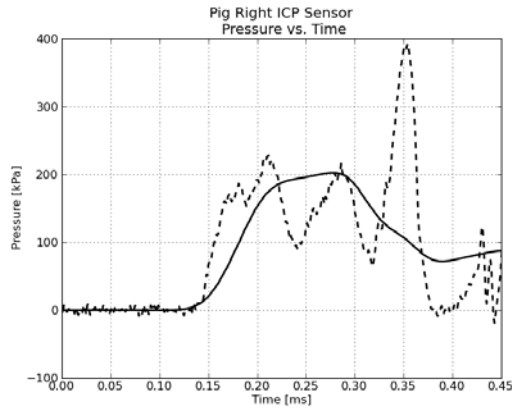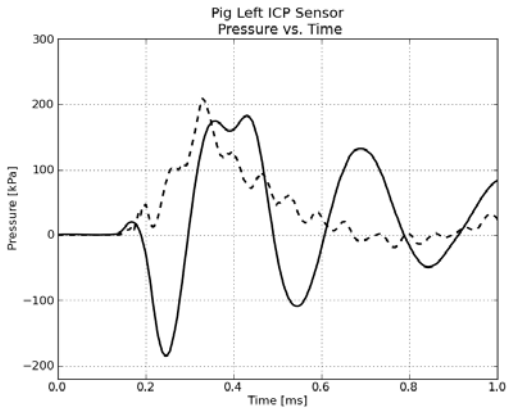
(a) Condition 1
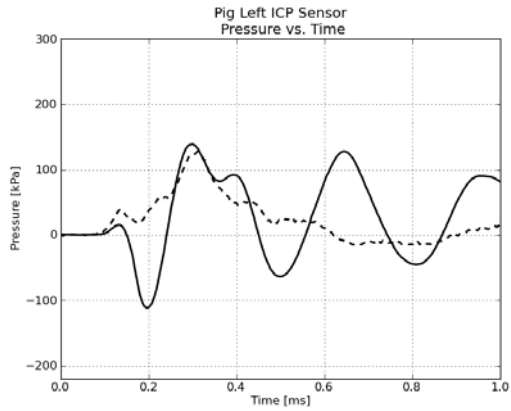
(b) Condition 2
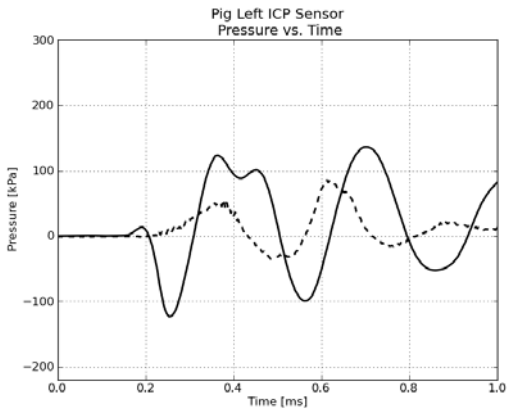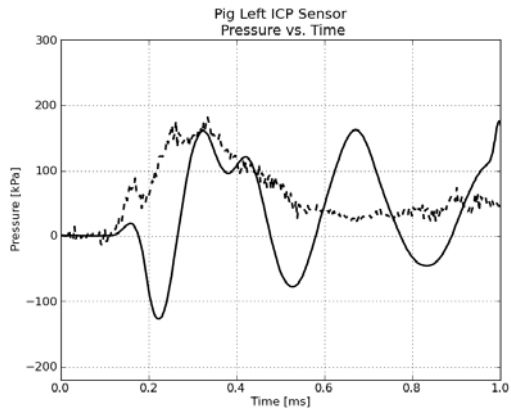
(c) Condition 3
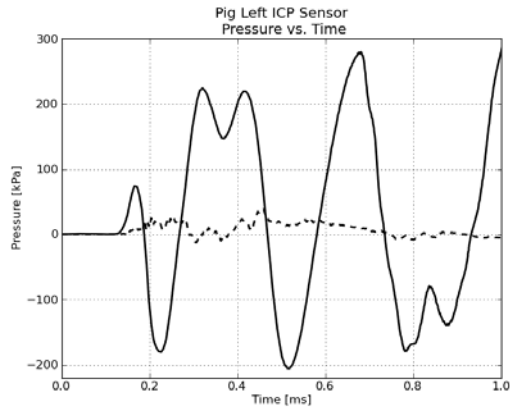
(d) Condition 4

(e) Condition 5

Figure 4-9: Comparison of computational and experimental pressure profiles at the left ICP sensor location. The solid lines represent simulation results, and the dashed lines represent experimental results.
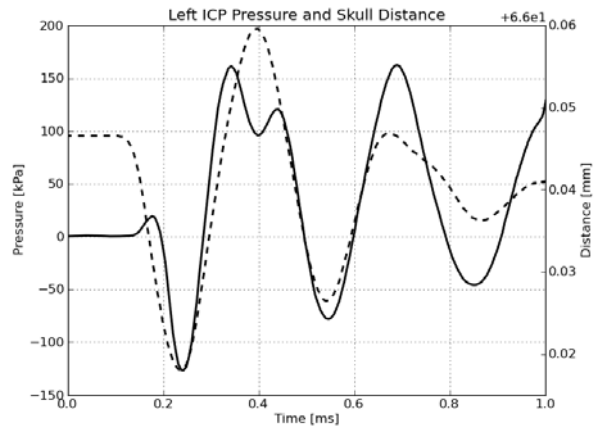
Figure 4-10: Comparison between pressure profile from the left ICP sensor location and the distance between two locations in the skull at blast condition 4.

Condition	Expt. Peak Pressure (kPa)	Sim. Peak Pressure (kPa)	% Difference
1	209	174	-17
2	128	139	+8.3
3	86.6	136	+57
4	181	161	-11
5	39.1	280	+615

Table 4.6: Comparison of Peak Pressure at Left Intracranial Sensor from Experiments and Simulations

periments for the five blast conditions. We can see that for all five blast conditions, the pressure profiles from the simulations exhibit oscillations that are not observed in the experiments. These oscillations appear to reflect the elastic "ringing" of the skull, since the left ICP sensor is located close to the skull and a nonlinear elastic model is currently used to describe the constitutive response of bone. At blast condition 4, for example, we can see from Fig. 4-10 that the pressure profile from the simulation is very similar to the time history of distance between two points in the skull, with both the pressure and distance profiles featuring oscillations with the same frequency. Using an alternative constitutive model for the skull may eliminate this effect.

Despite the extraneous oscillations, we can see that the simulations are again able to predict peak pressure magnitudes in the experiments, except at blast condition 5. From Table 4.6, we can see that excluding condition 5, the average percent difference in peak pressure magnitude is 23%. However, for condition 5, the difference in peak pressure from the simulation and experiment is 615%. While the peak pressure from the simulation at that condition is 280 kPa, the peak pressure from the experiment is only 39.1 kPa. Given that the experiments at conditions 1-4 have peak incident overpressures of 233-286 kPa and result in peak magnitudes at the left ICP sensor of 86.6-209 kPa, and given that the peak incident overpressure at condition 5 is 521 kPa, the experimental peak pressure value of 39.1 kPa is significantly lower than expected. We can clearly see from Fig. 4-11, which shows experimental vs. computational peak pressures at the three ICP sensors for all five blast conditions, that the peak pressure at the left ICP sensor for condition 5 is an outlier. The unexpectedly low reading from the left ICP sensor in the experiments conducted at blast condition 5, which is not consistent with the corresponding simulation or the other experiments, may be attributable to an experimental error, such as a malfunction of the pressure sensor.

In order to obtain some understanding of the uncertainty associated with the experimental results, we more closely examined the intracranial pressure profiles from blast condition 4, since four repeated tests were conducted at that condition. While four repeated tests are insufficient for rigorous statistical error analysis, in the absence of data from additional repeated tests, we averaged pressure over the four tests and
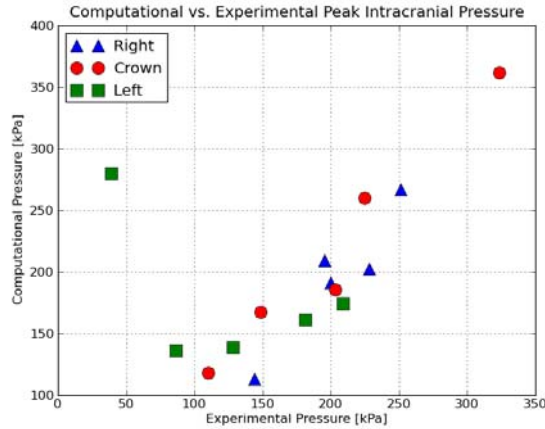
Figure 4-11: Computational versus experimental pressure for the three ICP sensors at all 5 blast conditions.

generated one standard deviation corridors. For each of the three intracranial pressure sensors, Fig. 4-12 compares the average pressure profile and one standard deviation corridors from the experiments with the pressure profile from the simulation.

In addition to the pressure profiles at specific locations, the simulations provide a wealth of quantitative data that enable the visual analysis of wave propagation through the porcine head, as well as the analysis of other metrics of mechanical response unavailable to the experiments, allowing us to increase our understanding of the blast response. For example, Fig. 4-13 shows a coronal slice of the porcine head at various time steps from the simulation at blast condition 4, illustrating the propagation of the pressure wave through the porcine head. We observe that by 0.132 ms, the blast has arrived at the head, and part of the pressure wave has begun to be transmitted through the soft tissue and skull. By 0.193 ms, it is evident that the pressure wave is significantly mitigated by the tissue surrounding the brain, resulting in pressures within the brain that are substantially lower than the pressures in the surrounding skull and soft tissue. Within the brain, there are fluctuations in the pressure field resulting from the interaction of waves reflecting off of the skull, and in some locations the pressure becomes negative, as we see at 0.331 and 0.612 ms. By 1.0 ms, the stresses in the intracranial cavity appear to have largely dissipated.

In addition to examining pressure contours, we can also investigate the highest
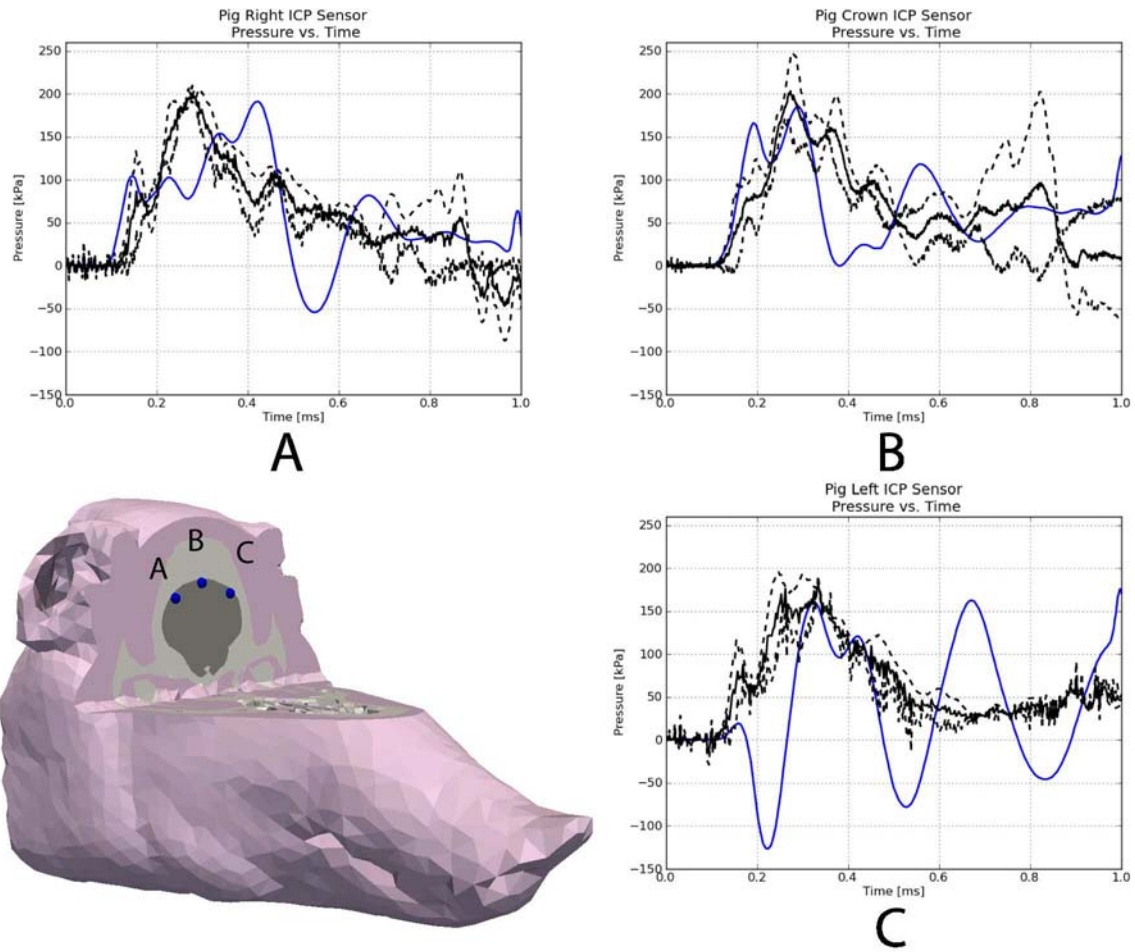
Figure 4-12: Comparison of pressure histories at three intracranial locations at blast condition 4. In the plots, the blue line represents the simulation results. The black lines represent pressure corridors from the experiments; the solid line represents the mean, and the dashed lines represent the upper and lower bounds of the experimental data.
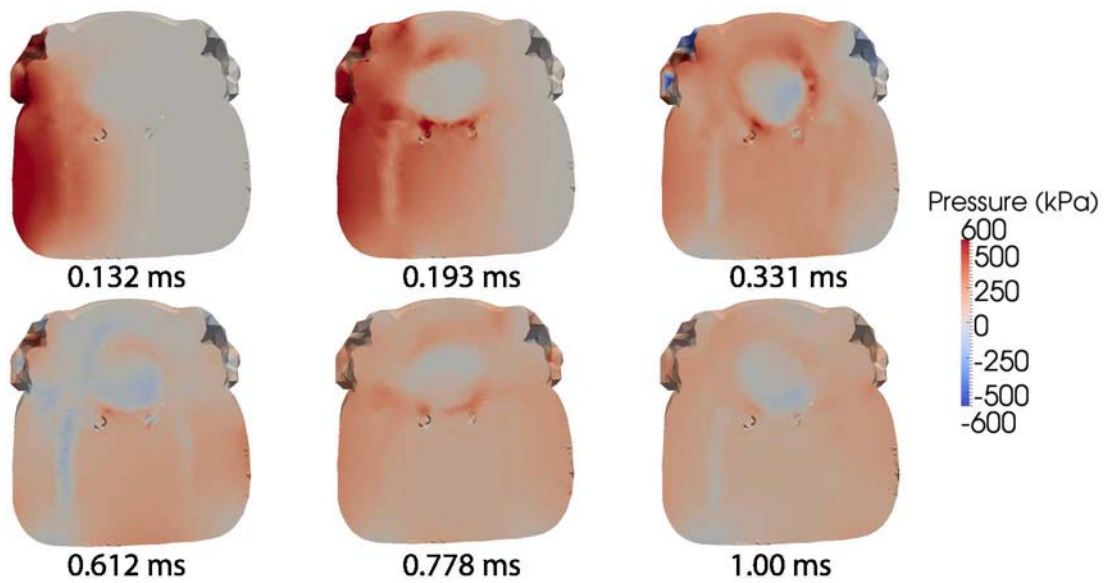
Figure 4-13: Coronal slices from the porcine head simulation at blast condition 4 showing time evolution of pressure contours

(a) Pressure Envelopes
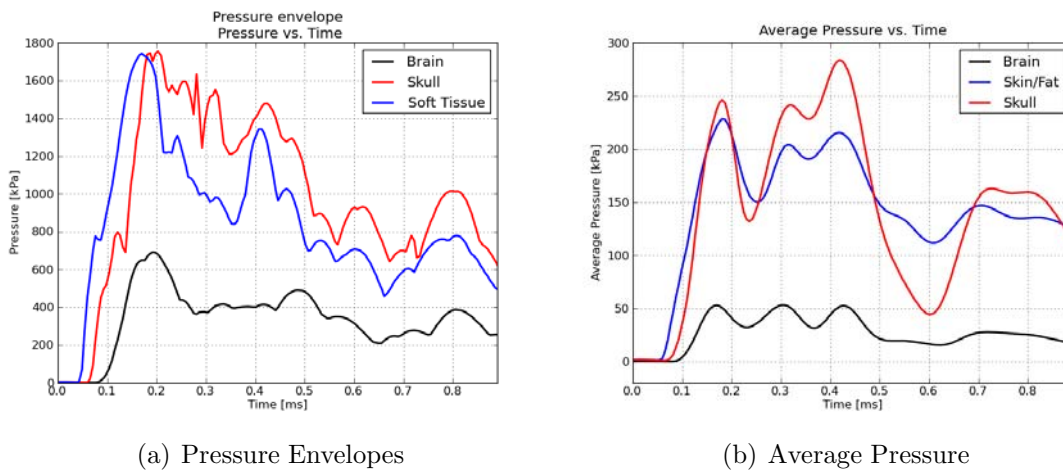
(b) Average Pressure

Figure 4-14: Pressure envelopes and average pressure from blast condition 4
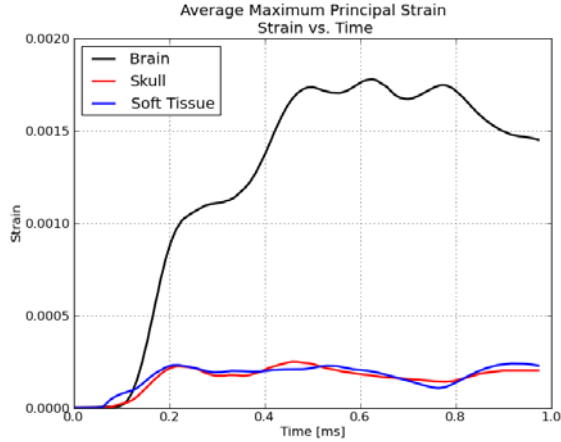
Figure 4-15: Average maximum principal strain from blast condition 4

pressures experienced in the porcine head. Fig. 4-14(a) depicts the pressure envelopes for the skull, brain, and soft tissue; these curves, which are the envelopes of the pressure histories of all points within each structure, give the maximum pressure for each structure at each time point. Looking at the envelopes, we see that the maximum pressures in the brain are significantly lower than the maximum pressures in the skull and soft tissue; while the maximum pressure reached in the skull is 1754 kPa, the maximum pressure reached in the brain is 691.8 kPa. In addition to looking at the highest pressures experienced by each structure, we also consider the average pressures in the various structures. While the standard deviations are high, indicating that the average pressure for a structure is not representative of the pressure at any given point in the structure, we can see from Fig. 4-14(b) that on average, the pressures in the brain are significantly lower than those in the skull and soft tissue; while the average pressure in the skull at times exceeds 250 kPa, the average pressure in the brain remains at or below 50 kPa.

Finally, we consider the maximum principal strains. To compute the principal strains, the principal stretches λ_i, or eigenvalues of the right stretch tensor $\mathbf{U} = (\mathbf{F}^T\mathbf{F})^{1/2}$, were obtained, and the principal Hencky strains $E = \ln\lambda_i$ were calculated. Fig. 4-15 shows the average strain in the skull, brain, and soft tissue; we can see that the largest strains were experienced in the brain, with the average strain exceeding 0.15%. The average strain in the skull and soft tissue remains below 0.05%. This
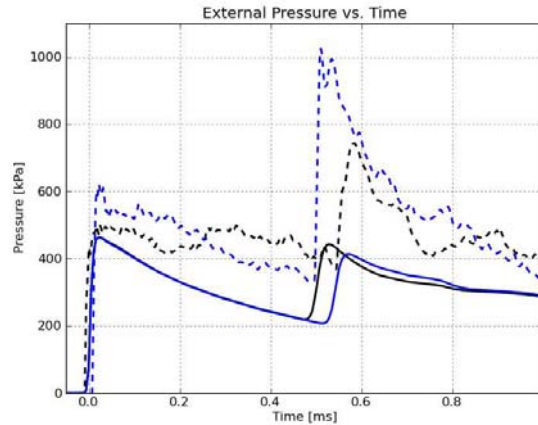
Figure 4-16: External pressure for cadaveric pig. The solid lines represent simulation results, and dashed lines represent experimental results. Each color represents one of two pressure sensors located 6.35 mm interior to the shock tube exit.

result is expected, since brain tissue is more compliant than the other porcine head materials.

Taken together, the envelopes, average histories, contours, and time histories at specific intracranial locations provide insight into the propagation of the pressure wave through the porcine head and the levels of mechanical stress experienced by the brain and other structures within the head.

4.4.2 Cadaveric Pig Test

In addition to the live pig tests, a test was conducted with a cadaveric pig at blast condition 5. From Fig. 4-16 and Fig. 4-17, we can see that the external and surface pressure profiles from the simulation exhibit similar characteristics. For example, the peak pressure at the right surface pressure sensor in the simulation, 1986 kPa, is within 2.2% of the peak pressure in the experiment, 2032 kPa. Looking at the right intracranial sensor profiles, as shown in Fig. 4-18, we find that the peak pressure from the simulation, 705 kPa, is within 1% of the peak pressure from the experiment, 699 kPa. However, while the peak pressure magnitudes and arrival times are reasonably similar in the simulation and experiment, the pressure profile from the simulation exhibits a number of oscillations that are not observed in the experiment.

111
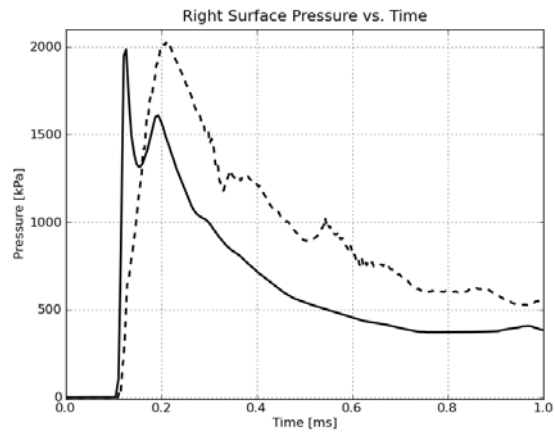
Figure 4-17: Right surface pressure for cadaveric pig. The solid line represents the simulation result, and the dashed line represents the experimental result.
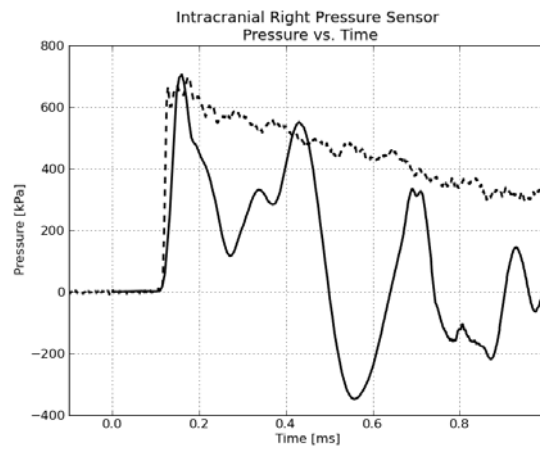
Figure 4-18: Right intracranial pressure for cadaveric pig. The solid line represents the simulation result, and the dashed line represents the experimental result.

4.4.3 PMHS Tests

Experiments were also conducted in which a PMHS was subjected to frontal and side blasts with incident overpressures of 130 kPa and 197 kPa. For each condition, three repeated tests were conducted.
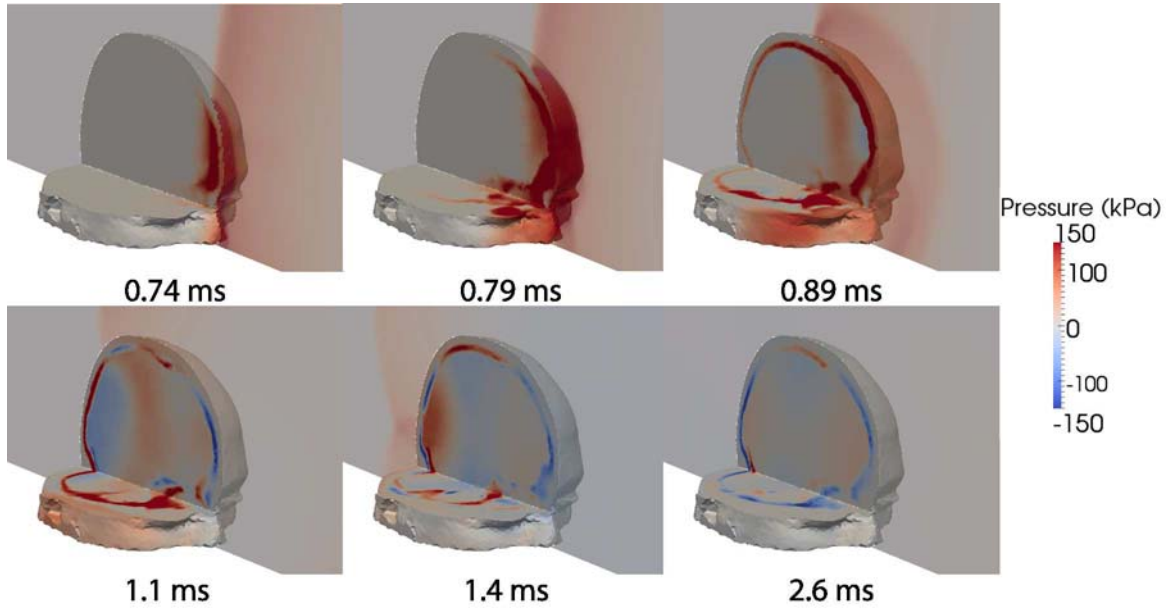
Figure 4-19: Pressure contours from the 130 kPa frontal blast PMHS simulation
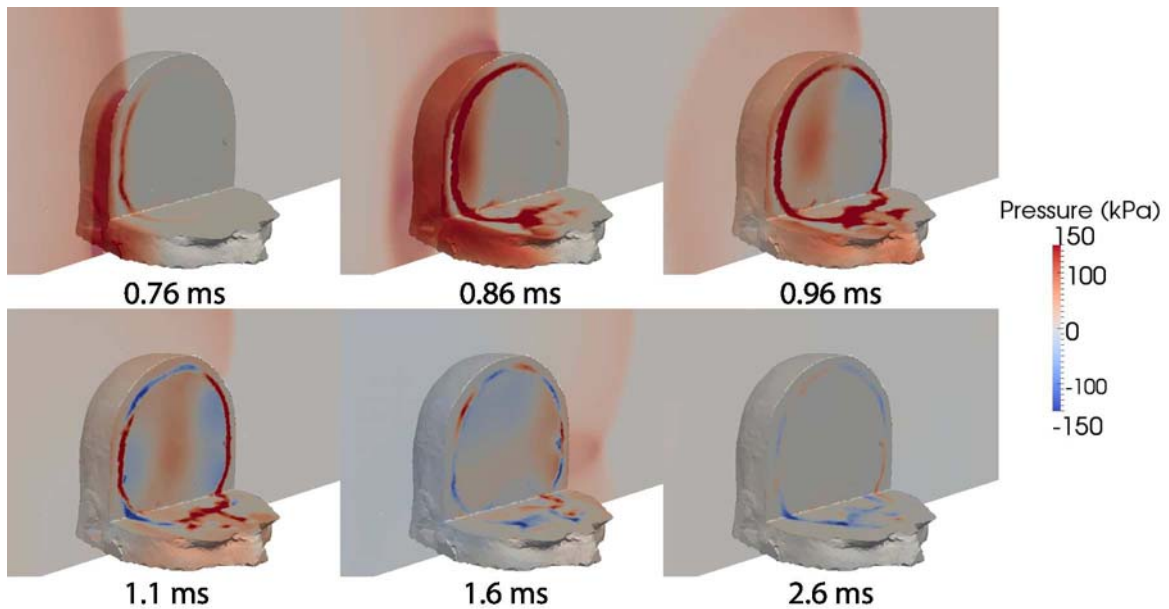
Figure 4-20: Pressure contours from the 130 kPa side blast PMHS simulation

(a) Front Blast   (b) Side Blast
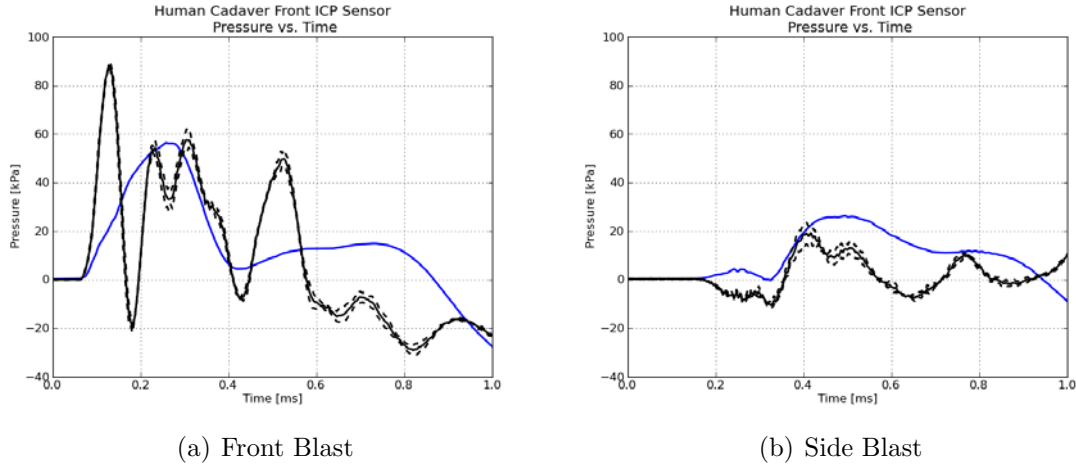
Figure 4-21: Front Intracranial Pressure, 130.3 kPa. The blue line represents the simulation results. The black lines represent the experimental results; the solid line is the average, and the dashed lines represent the one standard deviation corridors.

Fig. 4-19 shows pressure contours from the 130 kPa frontal blast simulation, and Fig. 4-20 shows pressure contours from the 130 kPa side blast simulation. In both sets of pressure contours, we can observe the arrival of the blast at the head, the subsequent partial reflection and transmission of stresses, and the propagation of stress waves through the intracranial cavity. Initially, stresses propagate through the skull more rapidly than through the air or other head structures due to the stiffness of the skull. By 1.1 ms, tensile stresses can be observed at the contrecoup site in both simulations, although by 1.4-1.6 ms, concentrations of compressive stress have developed at the contrecoup site. By 2.6 ms, the intracranial stresses have largely dissipated in both simulations.

The data available from the human cadaver experiments is more limited than the data from the porcine experiments, due to failure of some of the sensors. However, some comparisons between experimental and computational data can still be made, particularly for the front intracranial sensor. Fig. 4-21 shows pressure profiles from the front intracranial sensor for the front and side blast experiments and simulations at the 130 kPa blast condition, and Table 4.7 shows the peak pressure responses at that sensor location for the simulations and experiments at all four blast conditions. From Fig. 4-21, we can see that in both the front and side blast scenarios, the

simulations were able to capture the general behavior observed in the experiments. The peak pressure in the frontal blast simulation is within 36% of the experimental peak pressure and within 2% of a local maximum occurring near the simulation peak. For the side blast, we note that the peak pressure magnitudes from both the simulation and experiments are significantly lower than the magnitudes from the front blast scenario, which is expected at a sensor located in the frontal region. Comparing the experiments and simulations, we find that the peak pressure magnitude from the simulation is within 37% of the magnitude from the experiment. From Table 4.7, we can see that the percent difference between the peak pressure in the simulation and the average peak pressure in the experiments ranges from 18 to 39%, with the percent difference invariably exceeding the standard deviation from the experiments. However, because each test resulted from exposure of the same PMHS specimen with the same instrumentation to the same blast condition, little deviation from the mean would be expected in the experiments. We can also see that for the side blast, the frontal sensor location was not significantly affected by the increase in blast intensity.

Condition	Expt. Pressure (kPa)	Expt. Std. Dev.	Sim. Pressure (kPa)	% Diff.
Front, 130 kPa	88.3	0.4%	56.4	−36%
Front, 197 kPa	164	5.8%	99.8	−39%
Side, 130 kPa	19.0	23%	26.3	+38%
Side, 197 kPa	29.3	6.8%	34.6	+18%

Table 4.7: Comparison of Peak Pressure at Front Intracranial Sensor from Human Cadaver Experiments and Simulations

4.5 Discussion

The work presented in this chapter is an effort to validate a computational framework for modeling porcine and human head response to blast loading. In a series of repeated tests, 11 live, anesthetized pigs, 1 pig cadaver, and 1 human cadaver were exposed to side blasts generated by a compressed-gas shock tube. Simulations of the experiments were conducted, and pressure histories from the simulations and experiments were compared for locations inside and outside the head. In both the simulations and the

experiments, the external pressure histories displayed characteristics of shock loading, with a rapid rise to peak overpressure followed by exponential decay. In general, the external pressure histories from the simulations matched those from the experiments in terms of peak incident overpressure, positive duration, and arrival time of secondary peaks due to reflection.

After comparing the external blast loading in the experiments and simulations, we considered pressures at three intracranial locations. For the live pig tests, the percent difference between peak pressure magnitudes from experiments and simulations ranged from 4.4 to 21% for the right ICP sensor, 7.5 to 16% for the crown ICP sensor, and 11 to 57% for the left ICP sensor (excluding blast condition 5). At the right and crown ICP sensor locations, the simulations were better able to capture the shape and intensity of the experimental pressure profiles than at the left ICP sensor location, which was furthest from the blast. The larger discrepancies observed at the left ICP sensor location may have been due to the geometric effects of wave propagation and reflection becoming more evident by the time the pressure wave reached the left ICP location. Further, at the left ICP sensor location, the pressure profiles from the simulations all exhibited oscillations that were not observed in the experiments. The oscillations, which have the same frequency as the distance between two points in the skull, appear to reflect elastic "ringing" in the skull, which could be reduced or eliminated by an improved constitutive model for bone.

In addition to pressure histories at specific locations, the simulations provided data on the mechanical blast response throughout the porcine head. Looking at the simulation conducted at blast condition 4 in more detail, we found that the pressure contours depicted the partial transmission of the incident pressure wave through the soft tissue and skull into the brain, and they clearly showed that the porcine brain was significantly protected by surrounding structures. This protective effect was also evident from plots of pressure envelopes and average pressure for the various head structures, with maximum and average pressures in the brain significantly lower than corresponding values in the skull and soft tissue. In contrast to pressure, which was lowest in the brain, strain was highest in the brain, with maximum principal strains

116

in the brain reaching 2.9%. This result was expected, since the brain is significantly more compliant than either the skull or soft tissue. Overall, the results suggest that protective effect of surrounding structures on the brain is much more pronounced in the case of the pig than in the case of the human, raising some concerns about the potential relevance of pig injury models to human injury.

Results were also compared for pig and human cadaver experiments and simulations. At the right ICP sensor in the pig cadaver, there was only a 1% difference in the peak pressure magnitudes from the simulations and experiments. However, while the simulation featured a number of oscillations, possibly reflecting the complex wave interaction behavior within the brain, the oscillations were absent in the experimental results, possibly due to the nature of the cadaveric tissue. Comparing peak pressures at the right ICP sensor location from the live and cadaveric pig experiments, we found that the peak pressure observed in the case of the cadaveric pig, 705 kPa, was significantly higher than the pressure observed in the case of the live pig, 202 kPa. However, it is likely that the discrepancy in peak pressure magnitudes reflects sensitivity to location rather than difference in mechanical response of live and cadaveric porcine brain tissue. The right ICP sensors were placed in slightly different locations due to the difficulty of placing sensors in biological specimens, but based on that difference, we were able to match curves from both the cadaveric and live pig cases to curves from one simulation conducted using a single set of material properties. In the case of the human cadaver, we found that the peak pressure magnitudes from the simulations were within 18-39% of the peak pressure magnitudes from the experiments, and the simulations were generally able to capture the basic shapes observed in experimental pressure profiles.

Although every effort was made to incorporate the state of the art in the experimental and computational frameworks, there were a number of significant discrepancies between experimental and computational results. Some of the discrepancies may be explained by differences in the head geometries of the tested specimens and the computational models, uncertainty in the positioning of pressure sensors in the experiments, and calibration of the brain tissue constitutive model to data from tests

conducted using in vitro tissue, which is known to behave in a stiffer manner than in vivo tissue [103]. Additional data from live animal experiments would be helpful for further comparison with simulations; in particular, better instrumentation and the ability to measure metrics other than pressure would be useful for validation of the computational model.

Despite these discrepancies, we believe the level of validation is sufficient for the purposes of this thesis. The work presented in this chapter represents the current state of the art in blast experiments and simulations, and further improvements would require additional efforts to quantify and reduce uncertainty in both the experiments and the computational models that are beyond the scope of this thesis. Even with all the caveats, it is encouraging that the computational models were generally able to capture the overall level of blast response intensity observed in the experiments; such models may be used to improve our understanding of blast-induced TBI.

Chapter 5

Blast Mitigation Effects of Personal Protective Equipment

5.1 Introduction

As blast-induced TBI has gained prominence in the military conflicts in Iraq and Afghanistan, it has become necessary to understand the effect of personal protective equipment (PPE) on the mechanical response of the human head to blasts. While it is thought that current PPE allows U.S. service members to survive blasts that previously would have been fatal due to penetrating injuries or primary blast injury to gas-filled organs such as the lungs or gastrointestinal system, it is still unclear how PPE contributes to preventing blast-induced TBI. For example, while the ACH has been extensively tested for blunt impact mitigation and ballistic penetration resistance, its influence on the propagation of stress waves in the brain following blast exposure is largely unknown.

Some computational studies have begun investigating the effect of PPE on the human head response to blasts. In 2009, Moss and King conducted blast simulations involving an ellipsoid head and a hemi-ellipsoidal helmet shell [88]. Subjecting the head-helmet system to a 100 kPa blast, they observed that when the helmet is used with a nylon web suspension system, the blast wave washes under the helmet, resulting in geometric focusing of the blast wave and higher pressures under the helmet than

outside the helmet. When the helmet is used with foam pads, as in the ACH, they found that the underwash effect was largely prevented, but motion of the helmet was more strongly coupled to the head, increasing mechanical loads to the brain. Due to the grossly simplified geometries of the head and helmet, the simulation results are unreliable.

The first detailed investigation of the effects of the ACH on the blast response of the human head was [95], which presented an earlier version of the work described in this chapter. In that study, simulations were conducted in which computational models of a head, helmet, and conceptual face shield were subjected to blasts with an incident overpressure of 1 MPa. All of the head components were modeled using the approach described in Section 2.3.2, where the volumetric response is described by an equation of state and the deviatoric response is described by the neo-Hookean model.

Following the publication of [95], a few other groups began conducting computational studies on the effects of PPE on blast-induced TBI. For example, Zhang et al. used the Wayne State University Head Injury Model to conduct blast simulations with and without the ACH at overpressures ranging from 0.27 to 0.66 MPa and positive durations ranging from 1 to 3 ms [141]. Modeling the ACH shell using a transversely isotropic composite failure material model and the foam padding using a low density foam material model, they found that the stress wave response was more profound in the brain without the helmet than with the helmet; overall, the ACH mitigated intracranial pressures by 15-35% and reduced strain in the brain by 16-30%. The effect of the ACH varied by brain region, with the ACH reducing pressures in cortical regions but failing to provide significant protection to the brainstem. The effect of the ACH also varied with blast orientation, with a lower average reduction in cortical pressure in the side blast (20%) than in the forward (25%) and backward blasts (30%).

As in [95], which first presented the effects of adding a conceptual face shield to the ACH, some studies have investigated the effects of conceptual modifications to current PPE. For example, the U.S. Army Aeromedical Research Laboratory (USAARL) and

CFD Research Corporation (CFDRC) developed a computational head model based on the Virtual Head Project and conducted simulations not just with the ACH, but with full and partial visors [104]. First, subjecting their helmeted head model to a 1.6 MPa frontal blast, they found that the ACH without pads led to an underwash shock wave that reflected from the surface of the helmet and focused on the head, leading to pressures of up to 6-10 MPa. For the ACH with pads, they found that the underwash effect was attenuated, and the padded helmet reduced frontal pressure by 50% but increased occipital pressure by almost 10 times. Investigating the effect of full and partial visors, they found that a visor could reduce pressure in the eye and ear regions by up to 8 times; for eye protection, the half and full visors were equally effective, but for ear protection, the full visor was three times more effective than the half visor. Grujicic et al. also investigated a slight modification to the existing ACH, studying the blast mitigation performance of an ACH with polyurea pads rather than foam pads [54]. The ACH shell was modeled using an orthotropic equation of state and an orthotropic linear elastic strength model, and the polyurea pads were modeled using a time-dependent, nonlinear, viscoelastic formulation. In simulations with the helmeted head conducted at the two blast conditions previously used in [87], they found that the ACH equipped with polyurea pads provided some level of protection against mTBI. For the 5.2 atm (527 kPa) blast, they found that the ACH-pad system reduced maximum principal compressive stress by 40% and maximum shear stress by 8%. For the 18.6 atm (1.88 MPa) blast, they found that the maximum principal tensile stress was reduced by 65% and the shear stress was reduced by 20%. They thus concluded that the level of protection provided by the ACH-polyurea pad system increases with increasing blast peak pressure.

This chapter presents an investigation of the effects of the ACH and a conceptual face shield on the mechanical response of the human head to blasts; it is an extension of the work that was originally presented in [95]. Conducting blast simulations using a computational framework that includes a biofidelic human head model and the Socrate brain tissue constitutive model, we find that the ACH is able to somewhat mitigate blast effects in the brain, and the face shield addition may be able to

much more significantly reduce the stresses experienced in the brain following blast exposure.

5.2 Materials and Methods

5.2.1 The DVBIC/MIT Full Head Model and Extensions Including Protective Equipment

We adapted the FHM and ACH-FHM described in Chapter 2 for use in the simulations. Since the level of detail in those models was not needed to investigate the potential blast-mitigating effects of PPE, the FHM and ACH-FHM were simplified to allow for more rapid simulations at a lower computational cost. The resolution of the computational mesh was reduced, and the number of differentiated anatomical structures was decreased from eleven to four: cerebrum, skull, CSF, and soft tissue. The skin/fat and muscle were combined into a single structure and assigned properties for skin/fat. The gray matter, white matter, and glia were combined into a second structure with properties of brain tissue. The CSF, eyes, venous sinuses, ventricles, and air sinuses were combined into a third structure with properties of CSF. Finally, the skull was considered as a differentiated structure with properties of bone. To illustrate the resolution of the simplified computational meshes, Fig. 5-1 shows the exterior of the simplified ACH-FHM as well as the unified cerebrum mesh from the ACH-FHM. The simplified FHM consists of 343,527 quadratic tetrahedra, and the simplified ACH-FHM consists of 435,345 quadratic tetrahedra.

To investigate the effects of a face shield, a conceptual face shield was added to the ACH-FHM. The geometry of the face shield was designed such that the top edge of the face shield was coincident with the front edge of the ACH and the face shield smoothly projected from the surface of the helmet shell. Fig. 5-2(a) shows the geometry of the ACH-FHM with the face shield. Using the process described in Chapter 2, a finite element mesh was generated using the Octree algorithm in Ansys ICEM CFD and

(a) ACH and Soft Tissue   (b) Cerebrum
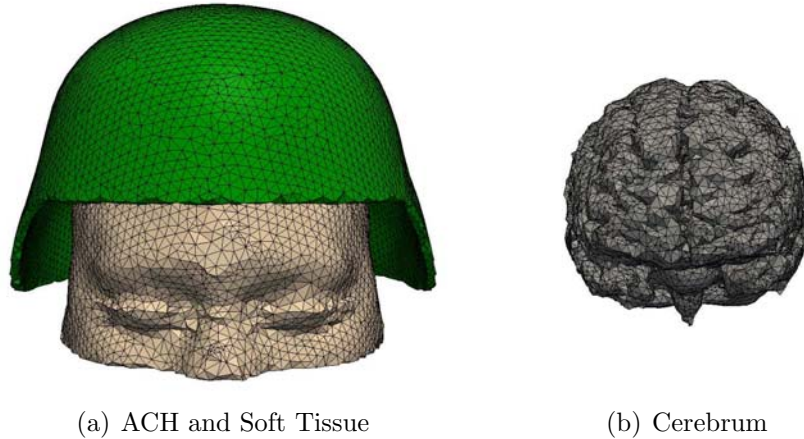
Figure 5-1: ACH, soft tissue, and cerebrum meshes from the simplified ACH-FHM mesh

optimized using the HealMesh[1] mesh optimization library. The resulting mesh of the head model with ACH and face shield consists of 443,452 tetrahedral elements with quadratic interpolation. Fig. 5-2(b) shows the full mesh, with sagittal and axial cuts to show the interior of the mesh.

5.2.2 Material Models and Properties

The mechanical response of the cerebrum was described using the Socrate brain tissue constitutive model, and the material model parameters given in Table 2.4 were used. The skull, CSF, and soft tissue were described following the approach described in Section 2.3.2, where the deviatoric response is described by the neo-Hookean model and the volumetric response is described by an equation of state – the Hugoniot equation of state for the skull and the Tait equation of state for the CSF and soft tissue. The material properties given in Table 2.2 were used for the skull, and the properties given for the CSF and skin/fat in Table 2.3 were used for the corresponding structures in the simplified HFM and ACH-HFM. The ACH shell, padding, and face shield were modeled as neo-Hookean materials, and the Kevlar properties given in Table 2.1 were used for the ACH shell and face shield, while the foam properties given in the same table were used for the padding.

---

[1]HealMesh ©Parasim Inc.
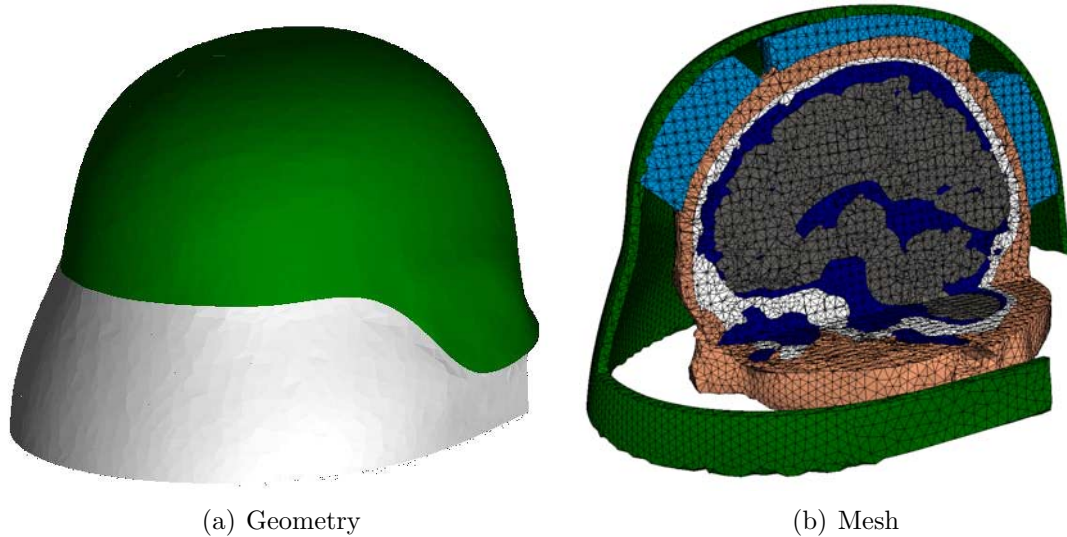
| (a) Geometry | (b) Mesh |

Figure 5-2: Simplified head model with ACH and face shield: (A) geometry of the ACH and face shield and (B) combined sagittal and axial cut showing the interior of the full computational mesh.

5.2.3 Simulation Loading Conditions

The blast conditions used in the simulations correspond to a free air explosion of 85 g of TNT at 1.07 m standoff distance, producing an incident overpressure of 100 kPa. The free-field incident overpressure was selected to be below the threshold for unarmored blast lung injury given by the Bowen curves, which estimate the tolerance to a single blast at sea level for a 70-kg human oriented perpendicular to the blast [20].

Throughout this chapter, time zero is taken to be the time of detonation. The simulations were run to a final time of 1.95 ms to evaluate the early-time response of the head when the severity of events inside the cranium is largest and the opportunities for mitigation using protective devices are greatest.

5.3 Results

In comparing the three simulations, we focus on stress wave propagation, which is the main dynamic effect loading brain tissue during a blast event. We focus in particular on pressure as a scalar metric of stress intensity. Fig. 5-3 shows snapshots of the
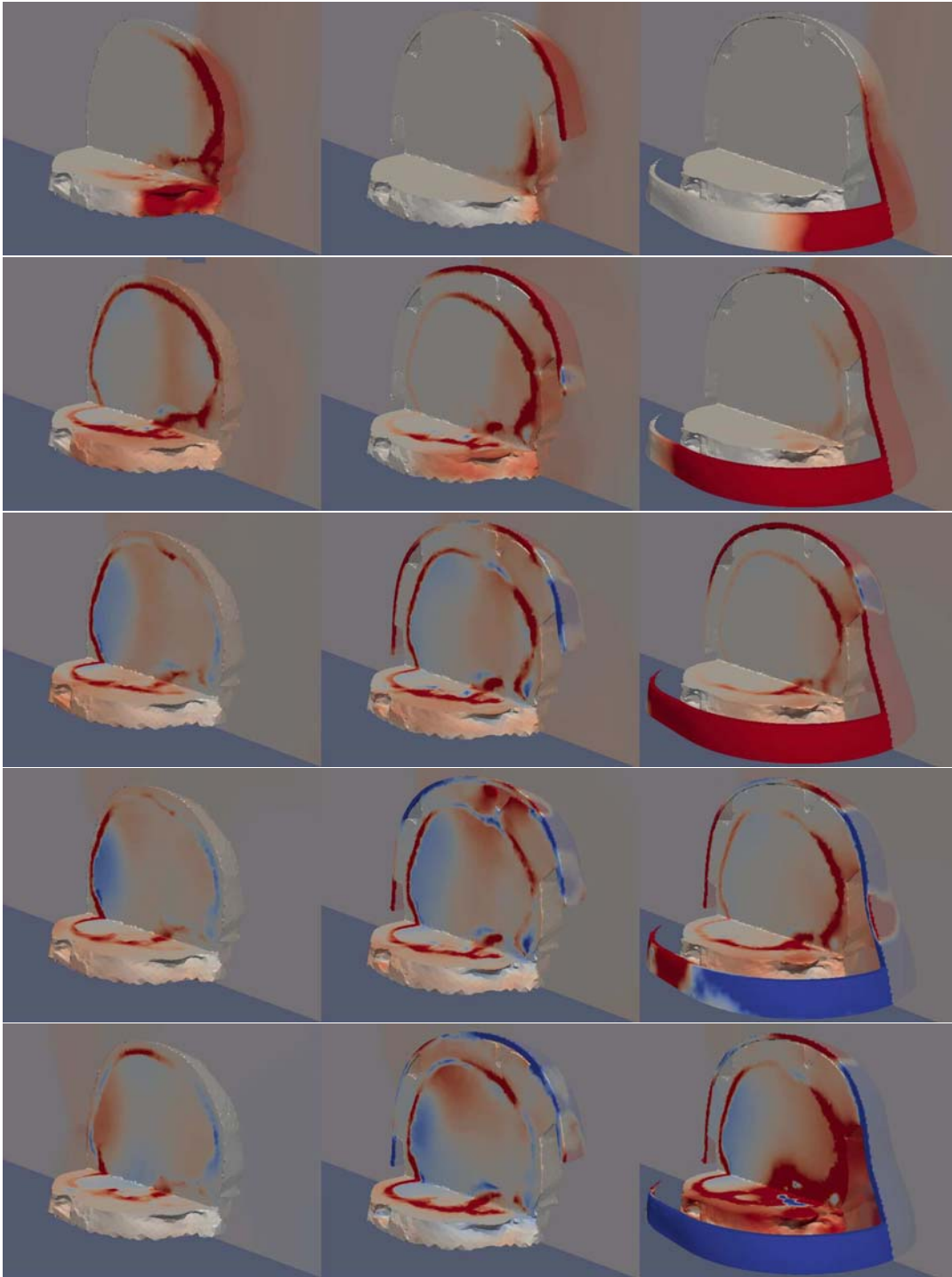
Figure 5-3: Pressure contours in the head (left), ACH (center), and face shield (right) simulations. Starting at the top, the rows correspond to time snapshots at 1.38, 1.53, 1.68, 1.78, and 1.95 ms. The scale is from -150 (blue) to 150 (red) kPa.

pressure fields in the fluid and solid structures, illustrating the progression of the interaction of the blast wave with the head and protective structures in the three simulations. Partial sagittal and axial cuts of the head are used to visualize the interior pressure fields. The fluid in the midsagittal plane is shown, although it is translucent to allow partial visualization of the solid on the other side of the plane. These snapshots allow us to qualitatively evaluate how protective equipment affect the propagation of pressure waves through the human head.

The figures in the left column of Fig. 5-3 correspond to the unhelmeted head simulation. At $t = 1.38$ ms, the blast wave is directly impinging on the face, transmitting a pressure wave from the soft tissue to the skull and into the intracranial cavity. At $t = 1.53$ ms, we can observe the pressure wave propagating through the intracranial cavity. We can also see that the pressure wave has traveled faster in the skull than in the other head tissues due to its higher relative stiffness. At $t = 1.68$ ms, we can observe some tensile behavior in the frontal region and a separate, larger region of tensile behavior in the occipital region that may be due to endogenous wave reflection or rarefaction. The simulation proceeds with fluctuations in the pressure field of decreasing intensity. By $t = 1.95$ ms, the stresses in the intracranial cavity have largely dissipated; there are elevated pressures in the occipital region, but the largest remaining stresses are largely located in the skull.

In the helmet simulation (center column of Fig. 5-3), it can be seen that the presence of the ACH slightly delays the arrival of the blast wave at the head but does not impede direct transmission of pressure waves into the intracranial cavity since it does not protect the face. The snapshot at $t = 1.38$ ms shows that in the helmet simulation, unlike the head simulation, the pressure wave has not yet been transmitted to the intracranial cavity. At $t = 1.53$ ms, we see that the transmitted pressure has propagated through the skull and has begun to propagate through the intracranial cavity, and we see the beginning of tensile response (indicated in blue) in the helmet shell, behind in the eyes, and in the occipital region. At $t = 1.68$ ms, we can see that there are higher pressures in the frontal part of the skull in the helmet simulation than in the head simulation, which may be due to the higher

pressures transmitted to the skull via the helmet-pad system. We can more clearly see at $t = 1.78$ ms that the foam pads act as load concentration points for the impulse transferred from the blast wave to the surface of the head. At $t = 1.95$, the stresses within the skull and intracranial cavity are higher than those observed in the head simulation.

Because it does not cover the face, the helmet does not significantly contribute to mitigating the stress waves transmitted to the brain tissue. While it does protect the top part of the head from direct exposure to the blast, the advantage is minimal since this is not a major pathway of load transmission into the intracranial cavity. Conversely, these results show that the existing ACH does not enhance blast effects on brain tissue as has been suggested recently with more simplistic models [88].

The column on the right of Fig. 5-3 shows snapshots of the pressure contours in the simulation including face protection. It can be seen that the immediate effect of the face shield is to impede direct transmission of stress waves to the face. At $t = 1.38$ ms, when the blast has already arrived at the head in both the unhelmeted head and ACH simulations, the blast has arrived at the face shield but has not arrived at the head, and there are no stresses within the head. At $t = 1.53$ ms, we can see that stresses have begun to be imparted to the head through two main mechanisms: through the foam padding and through the face. The stresses continue to increase as the surface of the head continues to be loaded, resulting in intracranial pressures by $t = 1.95$ that are significantly higher than the pressures observed in the head and helmet simulations.

Fig. 5-4 allows us to investigate the late rise in pressure in the face shield. We can see that at 1.42 ms, the blast wave has arrived at the face shield and has been partially reflected and partially transmitted. At 1.53 ms, we see that the portion of the blast wave that continued to propagate has arrived at the head and has partially been reflected back towards the face shield. At 1.58 ms, we see the portion reflected from head propagating towards the face shield, and at 1.66 ms, we see that the reflected portion has arrived at the face shield and has been amplified. At 1.72 ms, we notice amplification and focusing of the blast wave, resulting in significantly higher pressures
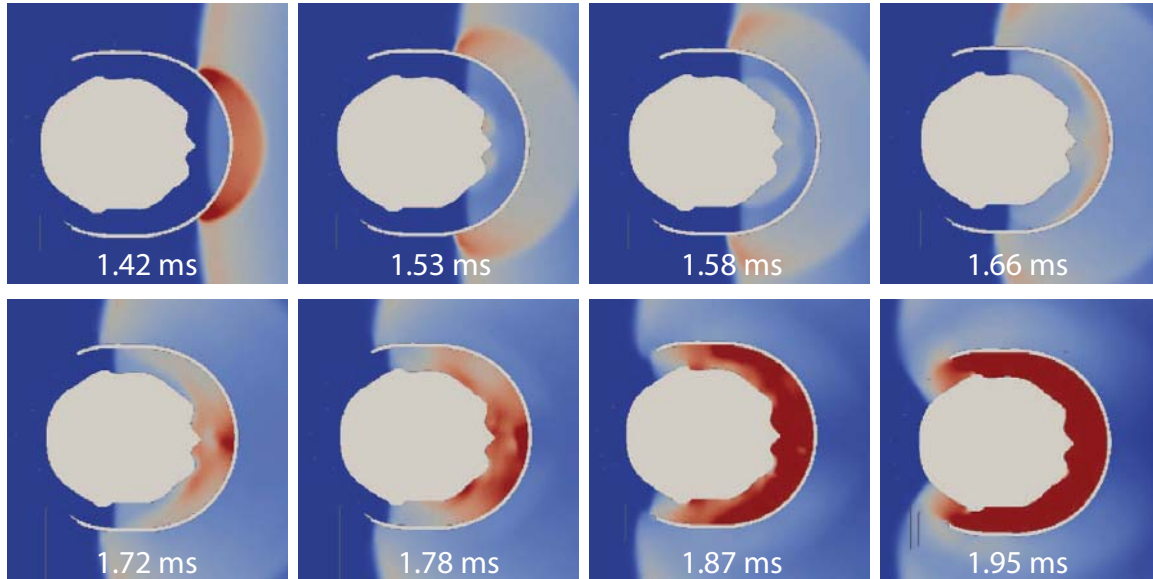
Figure 5-4: Time snapshots of an axial slice through the fluid and solid domain showing pressure amplification between the head and face shield. The scale is from -150 to 150 kPa.

in the interstitial space between the face shield and the head. This effect continues to be amplified at 1.78 ms. At 1.87 ms, when the blast wave wraps around the back of the helmet, the effect is heightened, with extremely high pressures in that interstitial space. By 1.95 ms, the pressure in the space between the head and the face shield has exceeded 150 kPa.

To develop a more quantitative understanding of the simulation results, pressure histories at a number of points within the skull and cerebrum were extracted and compared for all three simulations, as shown in Figs. 5-5 and 5-6. From these pressure histories, it can be observed that the helmet alone slightly delays and reduces the magnitude of pressure peaks, while the helmet-face shield combination has a much more pronounced effect.

For example, at location A in Fig. 5-6, which is located in the right temporal lobe of the cerebrum, the pressure in the head simulation reached a peak of 39.9 kPa at 1.67 ms. In the helmet simulation, the peak pressure was delayed 0.068 ms to 1.73 ms and reduced 11.2% to 35.4 kPa. In the face shield simulation, the pressure did not begin to rise above 1 kPa until 1.75 ms. The pressure then began to rise, and by the
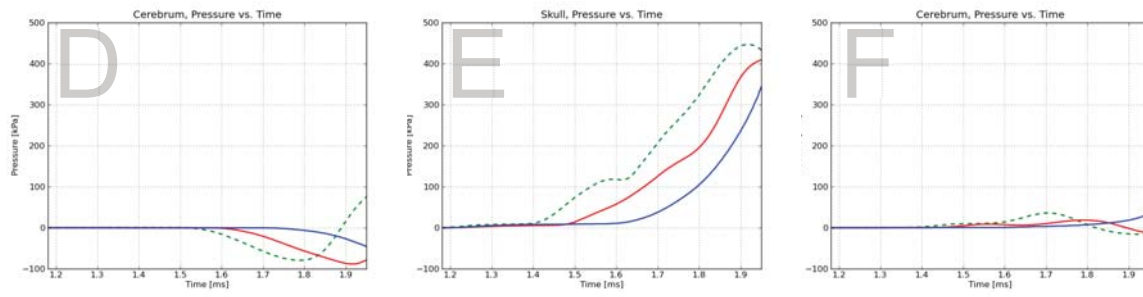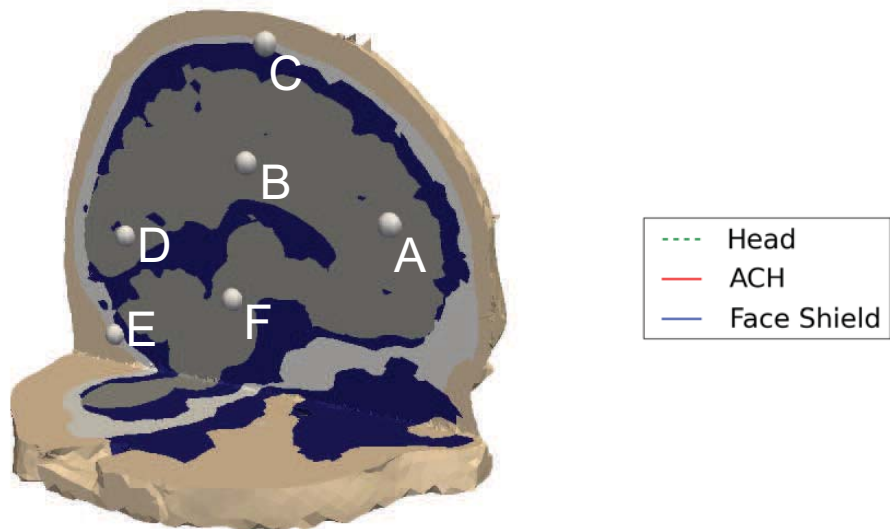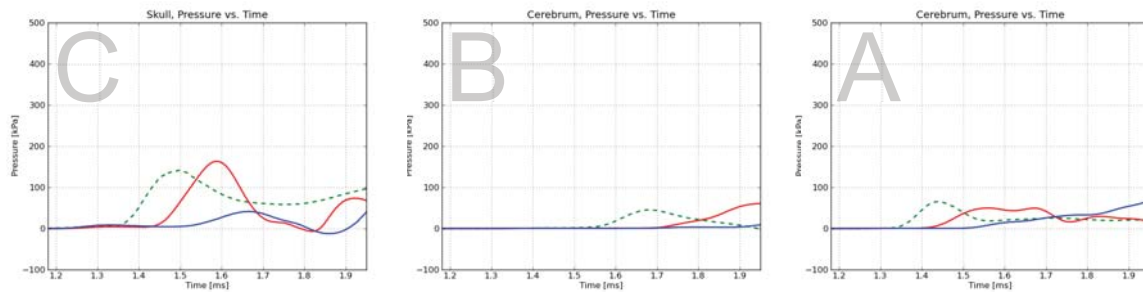
Figure 5-5: Pressure profiles from points in the skull and cerebrum that are located in the midsagittal plane.
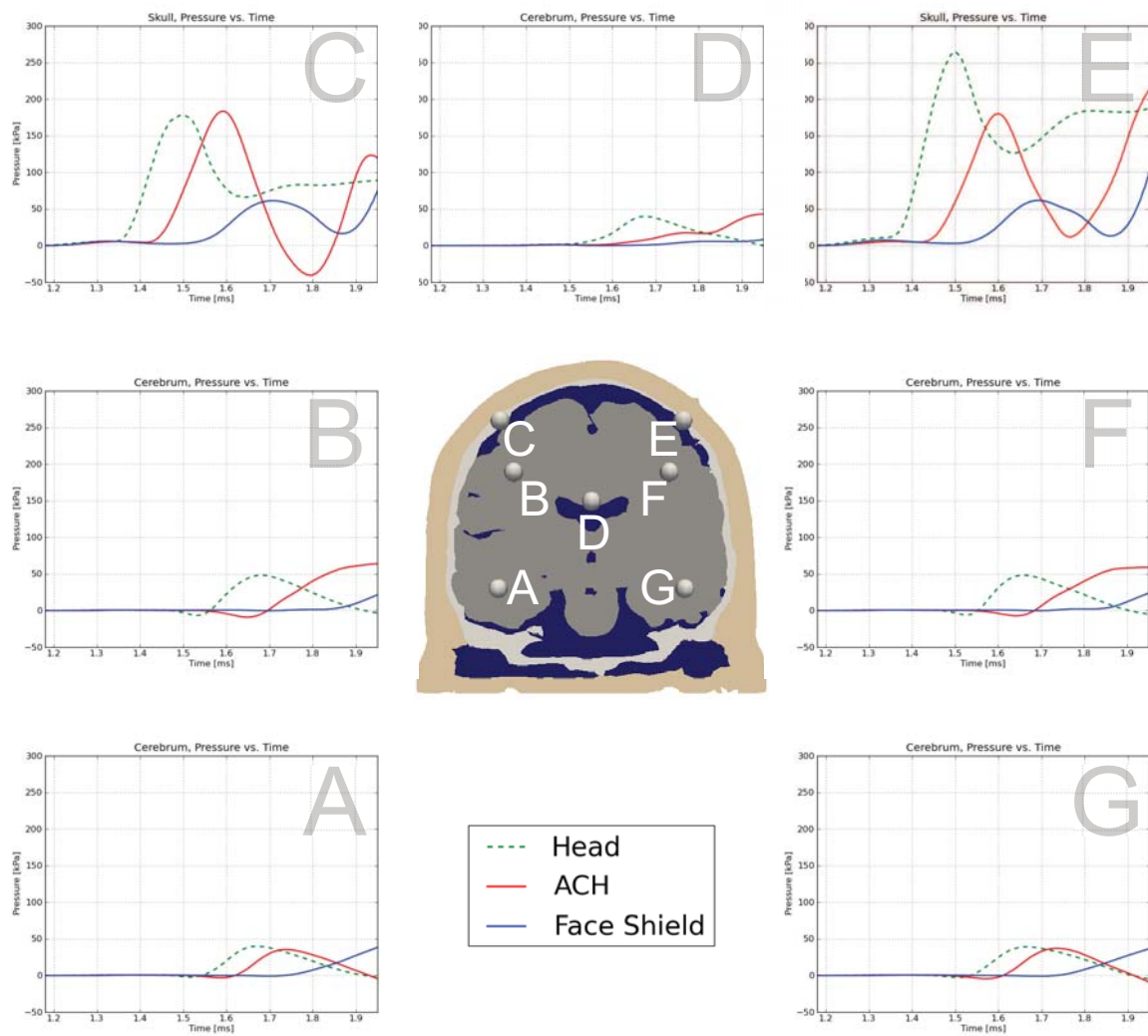
Figure 5-6: Pressure profiles from points in the skull and cerebrum that are located in the midcoronal plane.

end of the simulation, the pressure had reached a peak of 38.3 kPa, 3.8% lower than the peak experienced in the unprotected head simulation. As expected, the behavior at location G, a mirror image point in the left temporal lobe, is almost identical to the behavior observed at location A.

At location B, which is located in the right frontal lobe of the cerebrum, we observe a similar pattern of behavior. In the head simulation, the peak pressure of 48.3 kPa occurred at 1.68 ms. In the helmet simulation, the peak pressure was delayed 0.267 ms to 1.95 ms but increased by 32.3% to 63.9 kPa. In the face shield simulation, the peak pressure also occurred at 1.95 ms, but it only reached a magnitude of 21.4 kPa, 55.7% lower than the peak pressure magnitude in the head simulation. As with location G, here the behavior of location F, in the left frontal lobe, is essentially identical to the behavior observed at location B.

At location D, located in the corpus callosum, the peak pressure in the ACH simulation is 43.1 kPa, which is 7.85% more than the peak pressure in the head simulation of 40.0 kPa, but it occurs 0.271 ms later, at 1.94 ms compared to 1.67 ms in the head simulation. In contrast, the peak pressure in the face shield simulation is 8.31 kPa and occurs at 1.95 ms. The peak pressure in the face shield simulation is 79.2% lower and occurs 0.274 ms later than in the head simulation.

We also considered locations in the skull. At location C, the peak pressure in the head simulation is 178 kPa at 1.50 ms. In the ACH simulation, the peak pressure is delayed to 1.59 ms and increased 3.33% to 184 kPa. However, the face shield has an initial peak 61.4 kPa at 1.71 ms, which is 65.5% lower than the head peak. There is a later increase in pressure, with the overall peak pressure being 74.4 kPa at 1.95 ms. Even that, though, is 58.1% lower than the peak pressure in the head simulation. The behavior at location E was similar.

We also considered points along the midsagittal plane, as shown in Fig. 5-5. For example, for location A in Fig. 5-5, which is located in the frontal lobe of the cerebrum, the pressure in the head simulation reached a peak of 65.2 kPa at 1.44 ms. In the helmet simulation, the peak pressure is reduced by 23.5% to 49.9 kPa and is delayed 0.122 ms to 1.56 ms. In the face shield simulation, however, the pressure does not even

begin to rise above zero until 1.51 ms, and for much of the simulation, the pressure remains well below the pressure in the head and helmet simulations. There is a late rise in pressure, though, and by the end of the simulation at 1.95 ms, the pressure has reached a maximum of 67.5 kPa, which is 3.45% larger than the peak pressure in the head simulation.

At locations B and F, we observe similar patterns. At location B, the peak pressure of 45.4 kPa occurred in the head simulation at 1.68 ms. In the helmet simulation, the peak pressure was delayed to 1.95 ms, but also increased to 60.9 kPa. In the face shield simulation, the peak pressure also occurred at 1.95 ms, but was only 9.1 kPa, 74.8% lower than the peak pressure in the head simulation. At location F, in the midbrain, the peak pressure is 36.1 kPa at 1.70 ms in the head simulation. The peak pressure is reduced in magnitude by 48.3% to 18.7 kPa and delayed 0.086 ms to 1.79 ms in the helmet simulation. In the face shield simulation, the pressure only began to rise above zero at 1.60 ms, although by the end of the simulation it had reached a peak pressure of 35.4 kPa, which is only 1.9% lower than the peak pressure in the head simulation.

We also considered location D in the occipital lobe of the cerebrum, which experienced tensile pressure. As we observed in the snapshots, regions of tensile pressure were formed in the occipital region. In the head simulation, the peak tensile pressure reached was 79.4 kPa at 1.79 ms. In the helmet simulation, the peak tensile pressure was delayed by 0.124 ms to 1.91 ms but reached 88.5 kPa, which was 11.4% higher. The face shield simulation experienced a peak pressure of 45.4 kPa, which is 42.9% lower than the peak pressure in the head simulation, at 1.95 ms, which is 0.159 ms later than the head simulation and 0.035 ms later than the helmet simulation.

We also considered locations in the skull. At location C, near the vertex, the peak magnitude in the head simulation was 141 kPa at 1.49 ms. The peak pressure in the helmet simulation was increased by 15.6% to 163 kPa, but the peak was delayed by 0.093 ms to 1.59 ms. In the face shield simulation, the peak pressure was delayed an additional 0.36 ms to 1.95 ms, and the peak pressure magnitude was reduced by 70.8% from the head simulation to 41.3 kPa. At location E, at the base of the skull,

(a) Average Pressure   (b) Pressure Envelopes
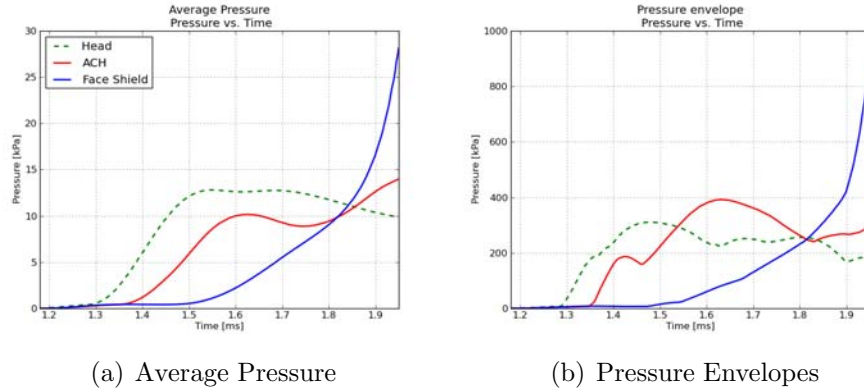
Figure 5-7: Average pressure and pressure envelopes from the head, helmet, and face shield simulations.

the peak magnitude reached in the head simulation was 447 kPa at 1.91 ms. In the helmet simulation, the peak magnitude of 409 kPa at 1.95 ms was 8.47% lower than the peak magnitude in the head simulation. In the face shield simulation, the peak magnitude was 343.6 kPa at 1.95 ms, which is 23.1% lower than in the head simulaton.

Both Fig. 5-6 and 5-5 suggest that the highest pressures occur in the skull, which, due to its stiffness, provides some natural protection to the brain tissue. Inside the brain, the maximum stresses are observed in the frontal region, where the transmitted stress waves initially enter the head for the front blast case analyzed.

Fig. 5-7 shows the average pressure and pressure envelopes (plots of the highest value at each time step) for the cerebrum in the head, helmet, and face shield simulations. These figures further confirm that the helmet slightly delays and does not significantly increase or mitigate stresses transmitted to brain tissue. The face shield, on the other hand, significantly mitigates stresses until the late rise in pressure discussed above.

5.4   Discussion

This chapter describes a simulation-based investigation of the possible blast-mitigating effects of the ACH, both by itself and with the addition of a conceptual face shield. First, a simulation was run exposing a biofidelic model of an unhelmeted human head

to a frontal blast wave with an intensity selected to be below threshold values of blast lung injury [20, 12]. The results suggest that the main transmission pathway involves the soft tissues in direct contact with the incident blast wave; stress waves are transmitted from the soft tissue to the skull to the intracranial cavity, where they propagate through the brain. The second simulation was intended to evaluate the blast protection properties provided by the ACH and foam pads. The results suggest that while the ACH provides no significant mitigation of blast effects on brain tissue, it does not have significant deleterious wave-focusing effects. The third simulation included a conceptual face shield rigidly attached to the helmet shell. It was found that the presence of the face shield contributed significantly to reducing the magnitude of stresses propagated inside the brain. However, this particular preliminary design of the face shield requires significant optimization.

The study was limited to a single set of material and blast characteristics (frontal incidence, fixed explosive mass, type, and standoff), which was sufficient to establish theoretical evidence that covering exposed head surfaces would likely contribute to mitigating blast-induced mild TBI. The conclusions are based on the trends and differences observed among the three simulations, which clearly show the effect of protection equipment. The study also focused on a preliminary design of a face shield; in order to enhance effectiveness in mitigating blast effects, the design must be optimized. Improvements to the face shield design may include increasing the stiffness, having the face shield attached to the ACH by a hinge, and extending the face shield in the posterior lower region of the head to reduce wave diffraction around the tip.

Chapter 6

Interspecies Scaling of Central Nervous System Response to Blast

6.1 Introduction

In medical research, animal studies are routinely conducted to gain understanding of human diseases. Following this approach, a number of studies have exposed animals such as mice, rabbits, pigs, and monkeys to controlled blasts in an effort to understand the effects of primary blast waves on the central nervous system (CNS) [113, 106, 13, 76]. These animal studies provide valuable data, allowing connections to be drawn between external blast loads and metrics such as intracranial pressure and behavioral test performance; however, in the absence of inter-species scaling laws for CNS vulnerability following blast exposure, it is not understood how to apply the findings of these studies to humans.

One common approach to developing animal-to-human scaling relations is allometric scaling. In its most widely used form, a biological variable is related to body mass through a power law:

$$Y = b \cdot m^a \tag{6.1}$$

where Y is a biological variable, m is body mass, and a and b are parameters. Typical values of a range from -0.25 for biological frequencies, such as heart rate and

respiratory rate, to 1.0 for physiological volumes [83, 3, 79]. Many of these allometric relations can be explained by mechanics-based arguments. For example, arguments based on elastic stability and flexure can explain Kleiber's law, which provides that metabolically-related variables, such as basal metabolic rate and rate of oxygen consumption, scale as $m^{3/4}$; this relation has been found to hold for animals ranging in size from the mouse to the elephant [83]. Applications of allometric scaling have been as disparate as prediction of pharmacokinetic properties of drugs in humans from animal studies [79] and investigation of whether the size of dinosaurs may have been limited by overheating [3].

In the context of blast lung injury, which is closer to the problem of blast-induced traumatic brain injury, Bowen et al. used dimensional analysis to derive the following time scaling expression:

$$t_{scaled} = t \left(\frac{m_{ref}}{m} \right)^{1/3} \tag{6.2}$$

where t is time, m is body mass, and m_{ref} is reference body mass [20]. This time scaling, which was thought to account for variation in chest wall thickness between species, has been adopted in subsequent studies of blast lung injury [12]. For the case of blast lung injury, where the known injury mechanism involves compression of the chest wall to achieve pressure equalization, this type of scaling is justified. Although the same type of scaling was recently used in a blast-induced brain injury study to account for variation in brain size between species [106], there was no investigation as to whether this scaling is appropriate for blast-induced brain injury. Given that the brain injury mechanism, while still a matter of debate, is nevertheless known to be wholly disparate from the lung injury mechanism, this type of scaling is speculative.

In this chapter, we use our computational framework to investigate the dependency of injury-relevant blast response metrics, such as peak intracranial pressure and von Mises stress, on anatomical parameters within and across species. First, in an intraspecies study, computational pig head models at three different sizes were subjected to a blast with an incident overpressure of 200 kPa and a positive duration of 3 ms. In a subsequent interspecies study, computational mouse, pig, and human

head models were subjected to blasts of varying incident overpressures and positive durations, and relationships between nondimensional scaling parameters and relevant blast response metrics were obtained.

6.2   Computational Head Models

6.2.1   Mouse Head

For this study, we adapted a publicly available finite element mesh [45] that was based on the Digimouse data set from the University of Southern California [37]. Digimouse is a 3D whole body digital mouse atlas that was generated from coregistered x-ray CT and color cryosection images of a 28 g nude male mouse. The labeled atlas consists of 21 segmented structures: whole brain, external cerebrum, cerebellum, olfactory bulbs, striatum, medulla, masseter muscles, eyes, lacrimal glands, heart, lungs, liver, stomach, spleen, pancreas, adrenal glands, kidneys, testes, bladder, skeleton, and skin. Fig. 6-1 shows sample cryosection and CT images of a coronal slice from the Digimouse data set.

The publicly available finite element mesh, which is shown in Fig. 6-2, consists of 210,161 tetrahedral elements and all 21 segmented structures. To adapt the mesh for this study, we used Ansys ICEM CFD to truncate the mesh to contain only the head and to consolidate the brain and external cerebrum into a single cerebrum structure. In addition, we added a sinus structure within the nasal cavity and manually optimized the mesh by adding new elements to fill gaps and ensuring that existing elements were assigned to the appropriate structure. The mesh was then further optimized by eliminating bad quality tetrahedra using the HealMesh optimization library. The final modified mesh, which is shown in Fig. 6-3(a), contains 36,720 tetrahedral elements and consists of the following materials: cerebrum, cerebellum, olfactory bulbs, striatum, medulla, sinus, masseter muscles, eyes, lacrimal glands, skull, and skin. The brain, which includes the olfactory bulb, cerebrum, cerebellum, striatum, and medulla, is shown in Fig. 6-3(b).

(a) Cryosection   (b) CT

Figure 6-1: Sample cryosection and CT images of a coronal slice from the Digimouse data set
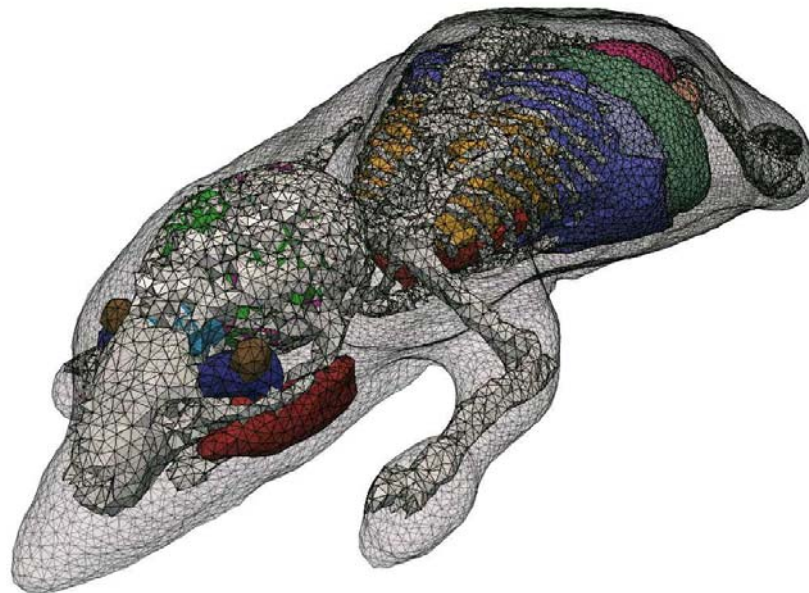
Figure 6-2: Publicly available finite element mouse mesh, with 21 structures
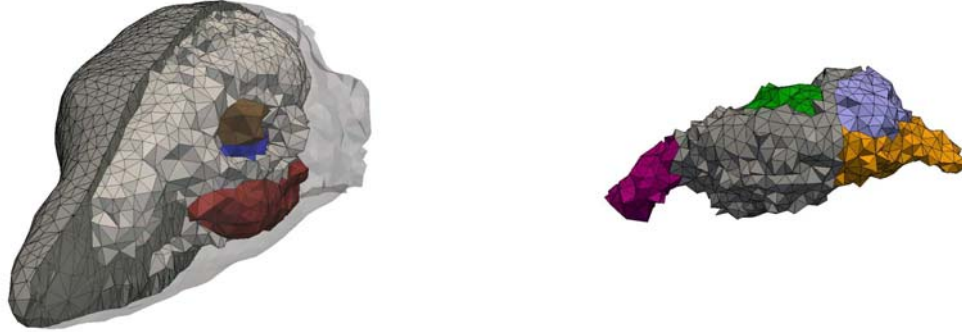
(a) View of the skin (gray), skull (white), eye (brown), lacrimal gland (blue), and masseter muscles (red).

(b) Side view of the mouse brain, which includes the olfactory bulb (magenta), cerebrum (gray), cerebellum (light purple), striatum (green), and medulla (gold).

Figure 6-3: Modified mouse head mesh

The mechanical response of the five brain structures was described using the Socrate brain tissue constitutive model described in Chapter 2 and the material model parameters given in Table 2.4. The simple viscoelastic model was used for the remaining structures, with the Hugoniot equation of state used for the skull and the Tait equation of state used for all other tissues. The material model parameters given for the human head structures in Tables 2.2 and 2.3 were used for the corresponding mouse head structures. For the lacrimal glands, the material properties of CSF were applied.

6.2.2   Pig Head

The pig head model presented in Chapter 4 was used in the pig simulations described in this chapter. To allow for an intraspecies investigation of size effects on blast response, the original pig head mesh was appropriately scaled to generate one model with 0.512 times the original mass and another model with 1.73 times the original mass. The sizes were selected to be within the range of reasonable pig head masses.

6.2.3   Human Head

The DVBIC/MIT Full Human Head Model presented in Chapter 2 was used in the human simulations described in this chapter.

6.2.4 Blast Loading Conditions

The mouse, pig, and human head models were first subjected to a blast with an incident overpressure of 200 kPa and a positive duration of 3 ms. The blast loading condition was selected to be above the pulmonary injury threshold and below the curve for 50% risk of moderate/severe brain hemorrhage for pigs [12, 106]. In order to assess the effect of varying overpressure, the models were then exposed to blasts with a positive duration of 3 ms and incident overpressures of 100 and 400 kPa. Additionally, in order to assess the effect of varying positive duration, the models were exposed to blasts with an incident overpressure of 200 kPa and positive durations of 2 and 4 ms. Finally, to investigate effects at a blast condition exceeding the 50% risk of moderate/severe brain hemorrhage, the models were also subjected to a blast with an incident overpressure of 400 kPa and a positive duration of 8 ms [106].

In the mouse simulation, the computational domain extended from -0.05 to 0.05 m in the x and y directions and from -0.00987 to 0.05 m in the z direction, with the center of the head model located at the origin. The fluid grid used two levels of subdivision, with an equivalent resolution of 1000 x 1000 x 600 grid points. 10 processors were used for the fluid solver, and 20 processors were used for the solid solver. In the pig and human simulations, the computational domain, fluid grid, and number of processors were the same as in the simulations described in Chapter 4.

6.3 Results

6.3.1 Intraspecies Scaling

We first investigated size effects within a species following primary blast exposure, subjecting pig head models at three different sizes to a blast with 200 kPa incident overpressure and 3 ms positive duration. We focused on two key metrics of blast response: maximum intracranial pressure ($p = \frac{1}{3}\sigma_{kk}$) and maximum intracranial von Mises stress ($\sigma_e = \sqrt{\frac{3}{2}s_{ij}s_{ij}}$). To obtain the maximum intracranial pressure, we first obtained the pressure envelope for the brain, which gives the maximum pressure in

the brain at each time point; the maximum intracranial pressure is then the peak pressure of the envelope. The pressure envelopes for the three simulations are shown in Fig. 6-4(a), and a plot of maximum intracranial pressure versus mass scale factor (ratio of porcine head mass to original porcine head mass) is shown in Fig. 6-4(b). From the two figures, it does not appear that there are any size effects within the species for the range of masses considered. We can see this more quantitatively in Table 6.1, which gives the brain mass, body mass, maximum intracranial pressure, and maximum intracranial von Mises stress for each sized porcine head model. The body mass was computed from the brain mass for each model using a brain-to-body mass ratio from the literature that has been widely accepted [28]. The smaller pig model, with a mass scaling factor of 0.512, resulted in a peak intracranial pressure that was within 0.18% of the peak intracranial pressure of the original model and a peak intracranial von Mises stress that was within 0.24% of the peak intracranial von Mises stress of the original model. For the larger pig model, with a mass scaling factor of 1.728, the peak intracranial pressure was within 0.23% of the original model's, and the peak intracranial von Mises stress was within 0.52% of the original model's. Neither of the scaled models had peak intracranial stress values that varied by more than 1% from the original model's; based on these results, there appear to be no size effects for the range of masses considered here.

Scaling Factor	Brain Mass (g)	Body Mass (kg)	Pressure (kPa)	VM Stress (kPa)
0.512	77.44	70.752	503.25	1030.8
1	151.3	138.23	502.3	1033.4
1.728	261.38	238.81	503.48	1027.98

Table 6.1: Pig Model Masses & Peak Intracranial Stresses

6.3.2 Interspecies Scaling

We then examined how the mechanical response of the brain to blasts scaled across three species. In light of the common allometric scaling relation $Y = b \cdot m^a$, we first considered a power law relationship between body mass and the key metrics of peak intracranial pressure and von Mises stress. Body mass values for the pig and human

(a) Pressure Envelopes   (b) Maximum Intracranial Pressure
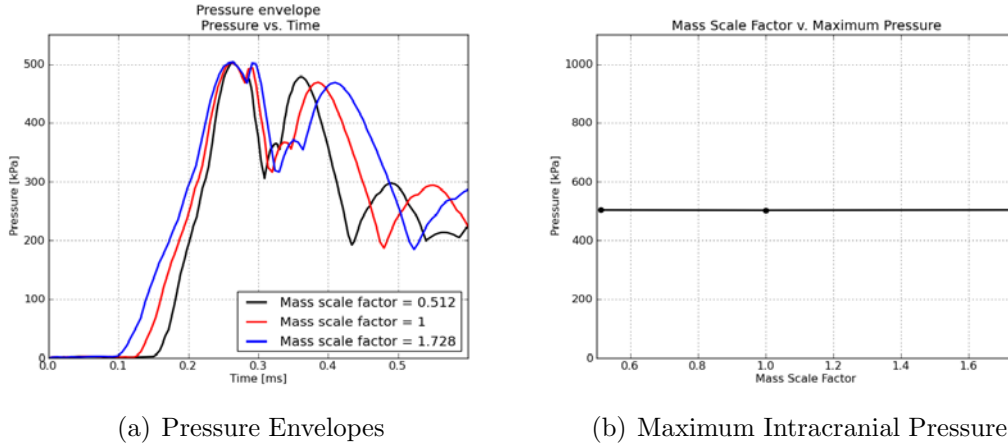
Figure 6-4: Investigation of intraspecies size effects based on blast simulations with computational pig head models at three sizes: (a) Maximum Pressure v. Time; and (b) Maximum Intracranial Pressure v. Mass Scale Factor.

models were computed from the mass of the brain in each model using brain-to-body mass ratios obtained from the literature [28]. For the mouse model, we used the known body mass of the mouse from which the model was generated. We can see from Fig. 6-5, which shows log-log plots of peak intracranial pressure and von Mises stress versus body mass for the 200 kPa, 3 ms blast condition, that power law scaling with body mass is inappropriate for translating these blast response metrics across species. Taking the natural log of both sides of the power function $Y = b \cdot m^a$, we obtain the expression $\log Y = a \log m + \log b$. On a log-log plot, this power function should be represented as a straight line with slope a and y-intercept $\log b$. However, we can see from Fig. 6-5 that a straight line could not be fit to the data with any reasonable correlation coefficient. A power law relationship with body mass thus appears to be inappropriate for scaling the blast response metrics across species.

Instead, based on the results, we considered alternative parameters. From Fig. 6-5, we observe that although the human and pig have similar body masses, the peak stresses within the brain are dramatically different in the two species. One explanation for this difference may be that the pig's skull and soft tissue, which are massive compared to the pig's brain, provide more protection from blasts than the human's skull and soft tissue. We therefore considered a ratio of brain mass to the mass of protective structures surrounding the brain, $\alpha = \frac{m_{brain}}{m_{skull} + m_{skin}}$, as a possible parameter

142
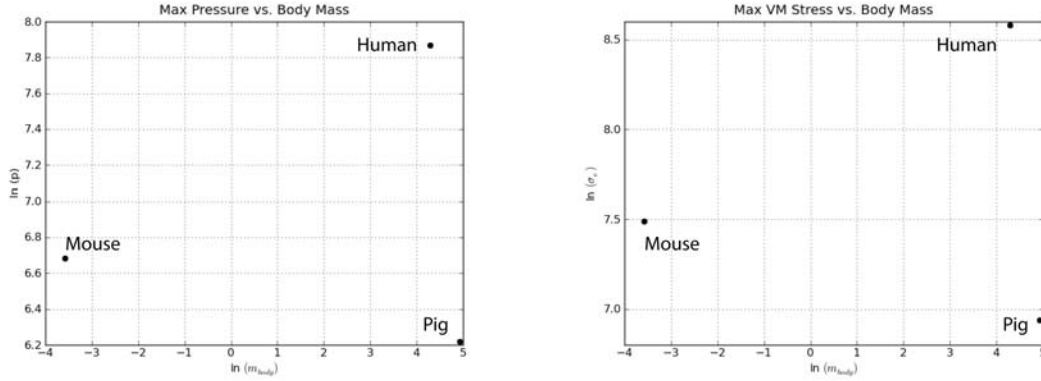
(a) Peak Intracranial Pressure v. Body Mass

(b) Peak Intracranial Von Mises Stress v. Body Mass

Figure 6-5: Log-Log Plots of: (a) Peak Intracranial Pressure v. Body Mass; and (b) Peak Intracranial von Mises Stress v. Body Mass

for scaling peak intracranial pressure and von Mises stress, normalized by ambient pressure, across species. Fig. 6-6(a) shows a log-log plot of $\frac{p}{p_a}$ versus α for the 200 kPa, 3 ms blast condition, where p is peak intracranial pressure and p_a is ambient pressure. We observe that a straight line can be fit to the three points with an R^2 value of 0.952, resulting in the following power law relation:

$$\frac{p}{p_a} = 23.7 \cdot \alpha^{0.475} \tag{6.3}$$

We can see from Fig. 6-6(b) that a power law relationship also exists between α and peak intracranial von Mises stress. Using linear regression, a line with almost the identical slope was fit to the maximum intracranial von Mises stress data, with an R^2 value of 0.974. We thus obtained the following power law relation:

$$\frac{\sigma_e}{p_a} = 49.5 \cdot \alpha^{0.471} \tag{6.4}$$

We also considered the brain-to-skull and brain-to-skin mass ratios as scaling parameters. Fig. 6-7 shows log-log plots of normalized peak intracranial pressure and von Mises stress versus the brain-to-skull mass ratio, along with the linear regression lines. For maximum intracranial pressure, the line of best fit has an R^2 value of 0.955,

(a) p/p_a v. α (b) σ_e/p_a v. α

Figure 6-6: Log-Log plots of normalized peak intracranial pressure and von Mises stress versus α for the 200 kPa, 3 ms blast condition

and it results in the following relation:

$$\frac{p}{p_a} = 14.1 \cdot \left(\frac{m_{brain}}{m_{skull}}\right)^{0.630} \tag{6.5}$$

For maximum intracranial von Mises stress, we obtained the following relation:

$$\frac{\sigma_e}{p_a} = 29.7 \cdot \left(\frac{m_{brain}}{m_{skull}}\right)^{0.625} \tag{6.6}$$

with an R^2 value of 0.976. Again, the slopes of the lines fit to the peak intracranial pressure and von Mises data were nearly identical.

Fig. 6-8 shows log-log plots of normalized peak intracranial pressure and von Mises stress versus the brain-to-skin mass ratio, along with the linear regression lines. For maximum intracranial pressure, the line of best fit has an R^2 value of 0.958, and it results in the following relation:

$$\frac{p}{p_a} = 18.6 \cdot \left(\frac{m_{brain}}{m_{skin}}\right)^{0.431} \tag{6.7}$$

For maximum intracranial von Mises stress, we obtained the following relation:

$$\frac{\sigma_e}{p_a} = 39.1 \cdot \left(\frac{m_{brain}}{m_{skin}}\right)^{0.427} \tag{6.8}$$

144

(a) p/p_a v. m_{brain}/m_{skull}

(b) σ_e/p_a v. m_{brain}/m_{skull}

Figure 6-7: Log-Log plots of normalized peak intracranial pressure and von Mises stress v. m_{brain}/m_{skull} in the 200 kPa, 3 ms blast simulations
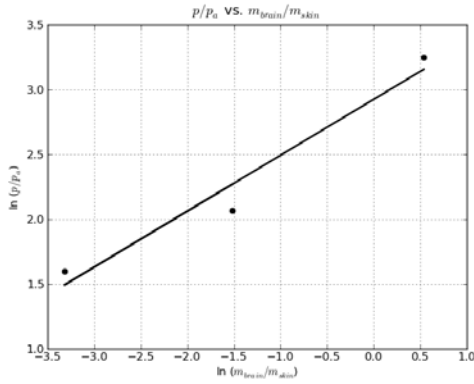
(a) p/p_a v. m_{brain}/m_{skin}
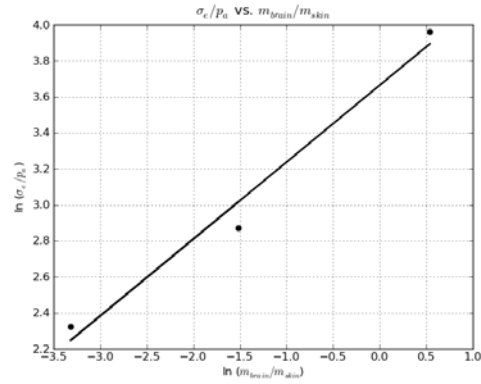
(b) σ_e/p_a v. m_{brain}/m_{skin}

Figure 6-8: Log-Log plots of normalized peak intracranial pressure and von Mises stress v. m_{brain}/m_{skin} in the 200 kPa, 3 ms blast simulations

with an R^2 value of 0.978. The data plotted in the figures is shown in Table 6.2.

Species	Body Mass (kg)	α	$\frac{m_{brain}}{m_{skull}}$	$\frac{m_{brain}}{m_{skin}}$	p (kPa)	σ_e (kPa)
Mouse	0.028	0.1567	0.5539	0.2186	800.455	1791.7
Pig	138.2	0.02946	0.15945	0.03614	502.326	1033.4
Human	72.97	0.9687	2.2291	1.713	2618.31	5322.1

Table 6.2: Mass Ratios and Peak Intracranial Stresses for the Mouse, Pig, and Human

In order to evaluate the effect of incident overpressure, in addition to the blast condition of 200 kPa and 3 ms, we also exposed the mouse, pig, and human head models to incident overpressures of 100 and 400 kPa. Fig. 6-9 shows plots of the
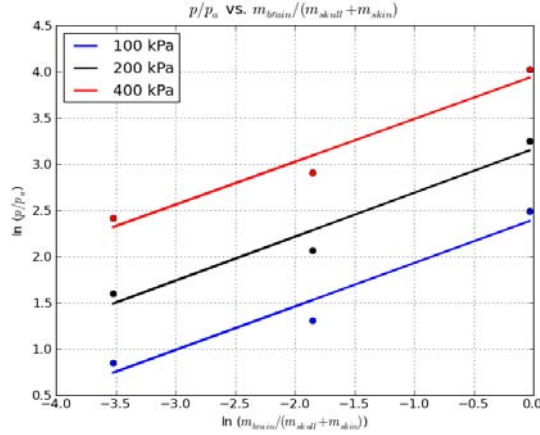
Figure 6-9: Log-Log plot of normalized peak overpressure v. α at overpressures of 100, 200, and 400 kPa

normalized peak intracranial pressures versus α at the three different overpressures, along with the lines of best fit. The slope (a) and y-intercept (b) of the three lines, along with the corresponding correlation coefficients, are given in Table 6.3.

Overpressure (kPa)	a	b	R^2
100	0.47	11.01	0.9506
200	0.48	23.66	0.9517
400	0.46	51.94	0.9615

Table 6.3: Linear Regression Lines for 100, 200, and 400 kPa blasts

We find that a remains constant, but there is a linear relationship between the incident overpressures p_0 and the values for b. Fig. 6-10 shows a plot of the b values versus incident overpressure, and we find that the line $b = 0.137p_0 - 3.13$ can be fit to the points with an R^2 value of 0.999.

We also investigated the effect of positive duration, conducting simulations at an incident overpressure of 200 kPa with durations ranging from 2 to 4 ms. Additionally, simulations were conducted at 400 kPa with durations of 3 and 8 ms. Unlike incident overpressure, we found that the length of positive duration had minimal effect on peak intracranial pressure or von Mises stress for the mouse and pig, and even for the human, the effect was small, as seen in Fig. 6-11.

Given the above results, we can therefore construct the following expression for
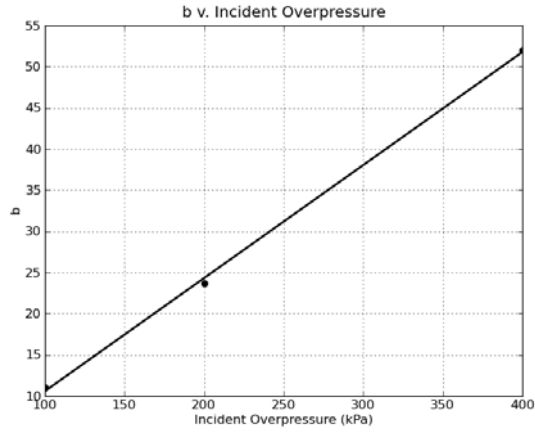
Figure 6-10: b v. Incident Overpressure
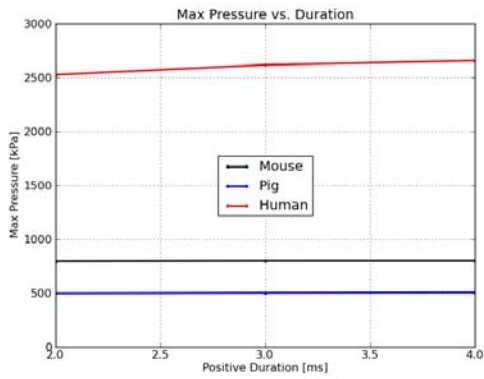
(a) 200 kPa
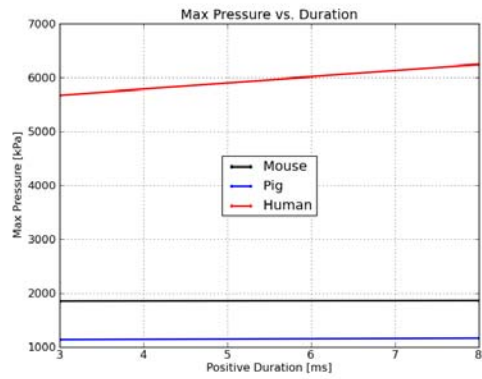
(b) 400 kPa

Figure 6-11: Peak intracranial pressure v. duration for two incident overpressures

peak intracranial pressure in an animal's brain, given the incident overpressure and the masses of the brain, skull, and skin:

$$p = p_a \cdot (0.1371p_0 - 3.13) \cdot \alpha^{0.47}$$ (6.9)

where p is peak intracranial pressure, p_a is ambient pressure, and p_0 is incident overpressure.

6.4 Discussion

In this chapter, we presented a general expression for peak intracranial pressure in a biological subject exposed to a blast, given the incident overpressure of the blast and the masses of the subject's brain, skull, and skin. Our simulation results suggest that peak intracranial pressure and von Mases stress, unlike many biological variables, scale across species not with body mass, but with mass ratios involving the brain and its surrounding protective structures.

A wide array of biological variables, from respiratory rate to population density, scale across species via power law relationships with body mass. While the variables appear to be wholly disparate, almost all of them are ultimately related to metabolism. For example, population density relates to the amount of resources an animal consumes, and organ growth can often be linked to metabolic rate. A number of explanations have been proposed for why metabolic variables scale with body mass. McMahon, for example, argued that for terrestrial vertebrates, energy metabolism scales with body cross-sectional area, which is proportional to d^2, where d is diameter [83]. McMahon then used elastic criteria to derive the relationship $d \propto m^{3/8}$ and arrive at Kleiber's law, which provides that metabolic variables scale as $m^{3/4}$. For some aquatic invertebrates and algae, Patterson suggested that scaling of metabolic rate with body mass could be explained by diffusion of metabolically important compounds through a boundary layer [99]. West used a more general model based on transport of fluids (e.g., air, blood) through space-filling fractal networks in

the body and minimization of energy needed to distribute resources to derive the 3/4 mass exponent for metabolic variables, since fluids transport oxygen and nutrients for metabolism [137].

In the case of blast-induced brain injury, however, our simulation results suggest that body mass is not a relevant parameter for scaling intracranial blast response metrics within or across species. Given the time scale of a blast event, transmission of stresses from the blast wave to the brain is not affected by metabolic processes, but instead is affected by the size of the brain in relation to the size of surrounding protective structures. From the simulations conducted with mouse, pig, and human heads at the 200 kPa, 3 ms blast condition, we obtained power law relations between key blast response metrics and $\frac{m_{brain}}{(m_{skull}+m_{skin})}$, $\frac{m_{brain}}{m_{skull}}$, and $\frac{m_{brain}}{m_{skin}}$. The mass exponents obtained for the two metrics – peak intracranial pressure and von Mises stress – were almost identical. It is not surprising that the mass ratios appear to be appropriate scaling parameters when we consider how stresses are transmitted from the blast wave to the intracranial cavity – namely, through the soft tissue and skull. An organism that has a high brain-to-skull or brain-to-skin ratio, such as the human, would therefore experience higher intracranial stresses than an organism with a low brain-to-skull or brain-to-skin ratio, such as the pig. It is also worth noting that the brain, skull, and skin masses are individually insufficient for inter-species scaling. It is not the size of just the brain, or just the skull and skin, that is relevant, but the size of the brain in relation to its protective structures.

Once we identified mass ratios such as $\alpha = \frac{m_{brain}}{(m_{skull}+m_{skin})}$ as the relevant scaling parameters and obtained power law relations between the mass ratios and peak intracranial pressure and von Mises stress at a given blast condition, we were able to investigate how the relations vary with blast condition. We conducted simulations at incident overpressures ranging from 100 to 400 kPa and positive durations ranging from 2 to 8 ms, and we obtained Equation 6.9, which is a general expression for peak intracranial pressure given the incident overpressure of a blast and the masses of the animal's brain, skull, and skin.

There are a number of limitations to this work, the most significant of which is

that only three species are represented in this study. In order to further investigate scaling functions for blast-induced brain injury, data from additional species is needed to confirm that the scaling relations proposed here are more widely applicable. To supplement the data we obtained for the 28 g, quadrupedal mouse, 73 kg, bipedal human, and 138 kg, quadrupedal pig, data is needed from additional representatives of large species, small species, bipeds, and quadrupeds. Another limitation of this work is that we investigated only two metrics of intracranial blast response; it is likely that other metrics may be as relevant, or more relevant, to blast-induced TBI. Additionally, another limitation is that the brain-to-body mass ratios used in this work were obtained from the literature and do not necessarily represent the mass ratios for the particular specimens that were studied.

Nevertheless, this work represents a first step in establishing scaling functions for blast response intensity within the brain. Using a simulation-based approach, we subjected mouse, pig, and human head models to blasts and found that the peak intracranial pressures and von Mises stresses scaled according to a power law relation between the blast response metrics and ratios of brain mass to the masses of surrounding structures. We also developed a general expression for peak intracranial pressure given an incident overpressure and the mass of the brain, skull, and skin. These results should provide a starting point for further investigation of scaling functions for blast-induced brain injury and should allow us to begin translating results from animal blast experiments to humans, allowing us to better understand the effects and mechanisms of blast-induced traumatic brain injury and to better protect human brains from the effects of blasts.

Chapter 7

Conclusions

In this thesis, we described a comprehensive computational framework for investigating the mechanical response of the human brain to blasts, conducted a validation effort that compared simulation results against data from free-field blast experiments involving physical human head surrogates and shock-tube tests involving pigs and human cadavers, and used the framework to examine the potential blast-mitigating effects of personal protective equipment and develop interspecies scaling laws that could enable translation of results from animal experiments to humans. We first presented the original framework in [87], using it to conduct the first detailed, biofidelic simulations of stress wave propagation in the human brain following blast exposure. In this thesis, we extended the framework to incorporate a sophisticated, experimentally-validated constitutive model for brain tissue and also to include detailed models of PPE and murine and porcine heads.

Further, we began to evaluate the ability of the framework to describe real-life systems by comparing simulation results with data from a broad range of experiments. We first compared results from free-field blast tests involving gel/plastic human head surrogates with simulation results, and we found that the difference between peak pressure magnitudes at various intracranial locations in the simulations and experiments ranged from 4.4 to 42% for an unhelmeted head and from 2.1 to 140% for a helmeted head. Comparing results from shock-tube tests involving biological specimens with our simulation results, we found that at the intracranial sensor locations,

the difference in peak pressure magnitudes ranged from 4.4 to 57% for the live pig, 1% for the pig cadaver, and from 18 to 39% for the human cadaver. Although the discrepancies between the experimental and numerical results were sometimes significant, we believe the level of validation achieved is sufficient for the purposes of this thesis. The work presented in this thesis represents the current state of the art in experimental and computational modeling capabilities, and further improvements would require a level of additional effort to quantify and reduce uncertainty in both the experiments and computational models that is beyond the scope of this thesis.

We then used the computational framework to investigate the potential blast-mitigating effects of PPE. Conducting blast simulations with an unhelmeted human head, a head with an ACH, and a head with an ACH and a face shield, we found that the ACH did not provide significant mitigation of blast effects on brain tissue, but neither did it have significant deleterious wave-focusing effects. Further, we found that the face shield contributed to sizeable reductions in the magnitude of stresses propagated within the brain, although it also resulted in elevated pressures in the interstitial space between the head and the face shield that led to a late rise in intracranial pressure. Improving the face shield design, for example by extending the face shield to fully wrap around the back of the head and/or having the face shield be hinged to allow release of pressure buildup between the head and face shield, could avoid the observed late rise in pressure.

Finally, this thesis concluded by proposing a relation for scaling two measures of blast response in the brain – peak intracranial pressure and von Mises stress – across species. First, based on mouse, pig, and human head simulations conducted at a blast loading condition selected to be above the pulmonary injury threshold and below the curve for 50% risk of moderate/severe brain hemorrhage for pigs, we developed a power law function relating α, the ratio of brain mass to the mass of surrounding protective structures, to peak intracranial pressure and von Mises stress. Second, based on simulations conducted at varying blast conditions, we developed a general expression for peak intracranial pressure within an animal's brain following exposure to a blast at a given incident overpressure, given the masses of the animal's brain,

skull, and skin. It is hoped that this general interspecies scaling relation could be used to translate results from animal blast injury experiments to humans.

7.1 Future Work

The work presented in this thesis is based on a comprehensive computational framework for modeling the blast response of the brain. Although this framework includes accurate blast initialization and fluid-structure interaction algorithms, an experimentally-validated brain tissue constitutive model, and three-dimensional, biofidelic head models, there are a number of features that could be added to further enhance its accuracy. First, more sophisticated material models for head and PPE components could allow simulations to better describe the mechanical response of the head. An enhanced constitutive model for bone could be particularly useful, given the critical role of the skull in protecting the intracranial cavity, and it could potentially eliminate the nonphysical, elastic "ringing" observed in Chapter 4. Second, more accurate material properties for the head components could also promote more accurate description of the blast response of the head. Currently, a significant amount of uncertainty surrounds the material property values of the various head components due to the difficulty of accurately measuring such values; the ranges of values reported in the literature are extremely wide. Third, improvement of the interface between the head and the helmet-pads system could enhance the accuracy of the helmeted head simulations. As we noted in Chapter 3, the helmeted head simulations tended to give rise to larger pressures than those observed in the experiments, possibly due to the conformal nature of the ACH-FHM. A contact algorithm that would allow sliding between the pads and the head may be more representative of the head-helmet interface.

Additional work is also needed to validate the computational framework. In this thesis, we presented a validation effort that compared simulation results with data from blast experiments involving physical human head surrogates, live and cadaveric pigs, and a human cadaver. While the comparisons provided a level of validation sufficient for the purposes of this thesis, additional work is needed to further reduce

discrepancies between experimental and numerical results. For example, improvements could be made by increasing the level of detail in the computational models and engaging in additional efforts to quantify and reduce uncertainty in the models and experiments. In addition, more extensive experimental data is needed. Experiments measuring metrics other than pressure, such as strain, and tests that are repeated at least five times at a given blast condition, for example, could be particularly useful for validation purposes.

Further investigation is also needed to better understand the effect of PPE on human head blast response and to devise strategies to protect against blast-induced mTBI. It would, for example, be advantageous to conduct PPE simulations with blasts from multiple angles and to explore potential improvements to the face shield design, such as extension of the face shield to wrap around the back of the head and inclusion of a hinge mechanism that would allow release of pressure buildup between the head and the face shield.

Finally, further investigation into interspecies scaling of blast effects is needed. A significant limitation of the interspecies scaling function presented in Chapter 6 is that it was developed using only three species. In order to determine whether this scaling function is generally applicable across species, simulations should be conducted with species across a wide range of sizes and shapes. In addition, the scaling work presented in Chapter 6 focused on a small set of potential scaling parameters – namely, mass ratios – and two metrics of blast response in the brain, peak intracranial pressure and von Mises stress. In future studies, it would be useful to explore other potential parameters and other metrics that may be relevant to blast injury.

Bibliography

[1] D.V. Agoston, A. Gyorgy, O. Eidelman, and H.B. Pollard. Proteomic biomarkers for blast neurotrauma: Targeting cerebral edema, inflammation, and neuronal death cascades. *Journal of Neurotrauma*, 26(6):901–911, 2009.

[2] M.P. Alexander. Mild traumatic brain injury: Pathophysiology, natural history, and clinical management. *Neurology*, 45(7):1253–1260, 1995.

[3] R. McNeill Alexander. All-time giants: The largest animals and their problems. *Paleontology*, 41:6, 1998.

[4] R.J. Anderson. Shell shock: An old injury with new weapons. *Molecular Interventions*, 8(5):204–218, 2008.

[5] K.B. Arbogast and S.S. Margulies. Material characterization of the brainstem from oscillatory shear tests. *Journal of Biomechanics*, 31(9):801–807, 1998.

[6] Armed Forces Health Surveillance Center (AFHSC). TBI numbers: Department of Defense worldwide numbers for traumatic brain injury. Online: http://www.health.mil/tbinumbers, 2012.

[7] R.A. Armonda, T.A. Tigno, S.M. Hochheimer, F.L. Stephens, R.S. Bell, A.H. Vo, M.A. Severson, S.A. Marshall, S.M. Oppenheimer, R. Ecker, and A. Razumovsky. Posttraumatic vasospasm and intracranial hypertension after wartime traumatic brain injury. *Perspectives in Medicine*, 1:261–264, 2012.

[8] E.M. Arruda and M.C. Boyce. A three-dimensional constitutive model for the large stretch behavior of rubber elastic materials. *J Mech Phys Solids*, 41:389–412, 1993.

[9] A. Atieh, M. Kalantari, R. Ahmadi, J. Dargahi, M. Packirisamy, and M.H. Zadeh. FEM analysis of the interaction between a piezoresistive tactile sensor and biological tissues. In *World Academy of Science, Engineering, and Technology*, 2011.

[10] Srikanti Rupa Avasarala. Blast overpressure relief using air vacated buffer medium. Master's thesis, Massachusetts Institute of Technology, 2009.

[11] W. E. Baker. *Explosions In Air*. University of Texas Press, Texas, 1973.

[12] C.R Bass, K.A. Rafaels, and R.S. Salzar. Pulmonary injury risk assessment for short-duration blasts. *Journal of Trauma-Injury Infection and Critical Care*, 65:604–615, 2008.

[13] R.A. Bauman, G. Ling, L. Tong, A. Januszkiewicz, D. Agoston, N. Delanerolle, Y. Kim, D. Ritzel, R. Bell, J. Ecklund, R. Armonda, F. Bandak, and S. Parks. An introductory characterization of a combat-casualty-care relevant swine model of closed head injury resulting from exposure to explosive blast. *Journal of Neurotrauma*, 26:841–860, 2009.

[14] H.G. Belanger, Z. Proctor-Weber, T. Kretzmer, M. Kim, L.M. French, and R.D. Vanderploeg. Symptom complaints following reports of blast versus non-blast mild TBI: does mechanism of injury matter? *Clinical Neuropsychologist*, 25:702–15, 2011.

[15] G. Belingardi, G. Chiandussi, and I. Gaviglio. Development and validation of a new finite element model of human head. In *Proceedings of the 19th International Technical Conference on the Enhanced Safety of Vehicles*, 2005.

[16] P.J. Belmont, G.P. Goodman, M. Zacchilli, M. Posner, C. Evans, and B.D. Owens. Incidence and epidemiology of combat injuries sustained during "The Surge" portion of Operation Iraqi Freedom by a U.S. Army Brigade Combat Team. *Journal of Trauma*, 68(1):204–210, 2010.

[17] Y. Bogdanova and M. Verfaellie. Cognitive sequelae of blast-induced traumatic brain injury: Recovery and rehabilitation. *Neuropsychol Rev*, 22:4–20, 2012.

[18] V. Bogo, R.A. Hutton, and A. Bruner. The effects of airblast on discriminated avoidance behavior in rhesus monkeys. Technical report, Lovelace Foundation for Medical Education and Research, 1971.

[19] R. Bolander, B. Mathie, C. Bir, D. Ritzel, and P. VandeVord. Skull flexure as a contributing factor in the mechanism of injury in the rat when exposed to a shock wave. *Annals of Biomedical Engineering*, 39:2550–59, 2011.

[20] I. Bowen, E.R. Fletcher, D.R. Richmond, F.G. Hirsch, and C.S. White. Biophysical mechanisms and scaling procedures applicable in assessing responses of the thorax energized by air-blast overpressures or by nonpenetrating missiles. *Ann. N.Y. Acad. Sci*, 152:122–146, 1968.

[21] B.S. Farrell. Coordinating authority needed for psychological health and traumatic brain injury activities. Technical Report GAO-12-154, U.S. Government Accountability Office, 2012.

[22] Centers for Disease Control and Prevention. *Explosions and Blast Injuries: A Primer for Clinicians*. CDC, Atlanta, GA, 2003.

[23] I. Cernak, J. Savic, Z. Malicevic, G. Zunic, P. Radosevic, I. Ivanovic, and L. Davidovic. Involvement of the central nervous system in the general response to pulmonary blast injury. *The Journal of Trauma: Injury, Infection, and Critical Care*, 40(3S):100S–104S, 1996.

[24] M.S. Chafi, G. Karami, and M. Ziejewski. Biomechanical assessment of brain dynamic responses due to blast pressure waves. *Annals of Biomedical Engineering*, 38(2):490–504, 2010.

[25] M. Chavko, W.A. Koller, W.K. Prusaczyk, and R.M. McCarron. Measurement of blast wave by a miniature fiber optic pressure transducer in the rat brain. *Journal of Neuroscience Methods*, 159(2):277–281, 2007.

[26] M.E. Clark, M.J. Bair, C.C. Buckenmaier, R.J. Gironda, and R.L. Walker. Pain and combat injuries in soldiers returning from Operations Enduring Freedom and Iraqi Freedom: Implications for research and practice. *Journal of Rehabilitation Research and Development*, 44(2):179–194, 2007.

[27] A.C. Courtney and M.W. Courtney. A thoracic mechanism of mild traumatic brain injury due to blast pressure waves. *Medical Hypotheses*, 72:76–83, 2009.

[28] G. Crile and D.P. Quiring. A record of the body weight and certain organ and gland weights of 3690 animals. *Ohio Journal of Science*, 40(5):219–259, 1940.

[29] D.K. Cullen, K.D. Browne, Y. Xu, S. Adeeb, J.A. Wolf, R.M. McCarron, S. Yang, M. Chavko, and D.H. Smith. Blast-induced color change in photonic crystals corresponds with brain pathology. *Journal of Neurotrauma*, 28:2307–18, 2011.

[30] J. Cummings, M. Aivazis, R. Samtaney, R. Radovitzky, S. Mauch, and D. Meiron. A virtual test facility for the simulation of dynamic response in materials. *Journal of Supercomputing*, 23:39–50, 2002.

[31] N.D. Davenport, K.O. Lim, M.T. Armstrong, and S.R. Sponheim. Diffuse and spatially variable white matter disruptions are associated with blast-related mild traumatic brain injury. *NeuroImage*, 59:2017–24, 2012.

[32] R. Deiterding, R. Radovitzky, S.P. Mauch, L. Noels, J.C. Cummings, and D. Meiron. A virtual test facility for the efficient simulation of solid material response under strong shock and detonation wave loading. *Engineering with Computers*, 22:325–347, 2006.

[33] A.M. Dennis and P.M. Kochanek. Pathobiology of blast injury. In Jean-Louis Vincent, editor, *Intensive Care Medicine*, pages 1011–1022. Springer Berlin Heidelberg, 2007.

[34] Department of Defense. Department of Defense Directive 6025.21E, 2006.

[35] Department of Defense. Annual Report to Congress on the Efforts and Programs of the Department of Defense Relating to the Prevention, Mitigation, and Treatment of Blast Injuries. Technical report, Department of Defense, 2012.

[36] P.C. Dischinger, G.E. Ryb, J.A. Kufera, and K.M. Auman. Early predictors of postconcussive syndrome in a population of trauma patients with mild traumatic brain injury. *Journal of Trauma: Injury, Infection, and Critical Care*, 66(2):289–297, 2009.

[37] B. Dogdas, D. Stout, A.F. Chatziioannou, and R.M. Leahy. Digimouse: A 3D whole body mouse atlas from CT and cryosection data. *Phys. Med. Biol.*, 53:577–587, 2007.

[38] D.S. Drumheller. *Introduction to wave propagation in nonlinear fluids and solids*. Cambridge University Press, 1998.

[39] P. Dudt, W. Lewis, K. Rye, H. DeJarnette, and D. Knight. Helmet effects for close-in blast waves. Technical Report NSWCCD-66-TR-2010/23, Naval Surface Warfare Center, Carderock Division, 2010.

[40] T. El Sayed, A. Mota, F. Fraternali, and M. Ortiz. Biomechanics of traumatic brain injury. *Computer Methods in Applied Mechanics and Engineering*, 197(51-52):4692–4701, 2008.

[41] N.M. Elsayed. Toxicology of blast overpressure. *Toxicology*, 121(1):1–15, 1997.

[42] S.L. Eskridge, C.A. Macera, M.R. Galarneau, T.L. Holbrook, S.I. Woodruff, A.J. MacGregor, D.J. Morton, and R.A. Shaffer. Injuries from combat explosions in Iraq: Injury type, location, and severity. *Injury*, 43(10):1678–82, 2012.

[43] M.-X. Huang et al. An automatic MEG low-frequency source imaging approach for detecting injuries in mild and moderate TBI patients with blast and non-blast causes. *NeuroImage*, 61:1067–82, 2012.

[44] A.I. Faden, P. Demediuk, S.S. Panter, and R. Vink. The role of excitatory amino acids and NMDA receptors in traumatic brain injury. *Science*, 244(4906):798–800, 1989.

[45] Q. Fang and D. Boas. Tetrahedral mesh generation from volumetric binary and gray-scale images. In *Proceedings of IEEE International Symposium on Biomedical Imaging*, volume 53, pages 1142–1145, 2009.

[46] M.R. Galarneau, S.I. Woodruff, J.I. Dye, C.R. Mohrle, and A.L. Wade. Traumatic brain injury during Operation Iraqi Freedom: Findings from the United States Navy-Marine Corps combat trauma registry. *Journal of Neurosurgery*, 108(5):950–957, 2008.

[47] S. Ganpule, A. Alai, E. Plougonven, and N. Chandra. Mechanics of blast loading on the head models in the study of traumatic brain injury using experimental and computational approaches. *Biomech Model Mechanobiol*, 2012.

[48] R.H. Garman, L.W. Jenkins, R.C. Switzer, R.A. Bauman, L.C. Tong, P.V. Swauger, S.A. Parks, D.V. Ritzel, C.E. Dixon, R.S.B. Clark, H. Bayir, V. Kagan, E.K. Jackson, and P.M. Kochanek. Blast exposure in rats with body shielding is characterized primarily by diffuse axonal injury. *Journal of Neurotrauma*, 28(6):947–59, 2011.

[49] A. Gawande. Casualties of war - military care for the wounded from Iraq and Afghanistan. *New England Journal of Medicine*, 351:2471–2475, 2004.

[50] M.D. Gilchrist, D. O'Donoghue, and T.J. Horgan. A two-dimensional analysis of the biomechanics of frontal and occipital head impact injuries. *International Journal of Crashworthiness*, 6(2):253–262, 2001.

[51] S.W. Gong, H.P. Lee, and C. Lu. Computational simulation of the human head response to non-contact impact. *Computers and Structures*, 86(7-8):758–770, 2008.

[52] K.R. Gould, J.L. Ponsford, L. Johnston, and M. Schonberger. Predictive and associated factors of psychiatric disorders after traumatic brain injury: A prospective study. *Journal of Neurotrauma*, 28(7):1156–63, 2011.

[53] M. Grujicic, G. Arakere, and T. He. Material-modeling and structural-mechanics aspects of the traumatic brain injury problem. *Multidiscipline Modeling in Materials and Structures*, 6:335–363, 2010.

[54] M. Grujicic, W.C. Bell, B. Pandurangan, and P.S. Glomski. Fluid/structure interaction computational investigation of blast-wave mitigation efficacy of the Advanced Combat Helmet. *Journal of Materials Engineering and Performance*, 20:877–893, 2011.

[55] A. Gyorgy, G. Ling, D. Wingo, J. Walker, L. Tong, S. Parks, A. Januszkiewicz, R. Baumann, and D.V. Agoston. Time-dependent changes in serum biomarker levels after blast traumatic brain injury. *Journal of Neurotrauma*, 28(6):1121–6, 2011.

[56] M.H. Heitger, R.D. Jones, A.D. Macleod, D.L. Snell, C.M. Frampton, and T.J. Anderson. Impaired eye movements in post-concussion syndrome indicate suboptimal brain function beyond the influence of depression, malingering or intellectual ability. *Brain*, 132(10):2850–2870, 2009.

[57] J. Ho and S. Kleiven. Dynamic response of the brain with vasculature: A three-dimensional computational study. *Journal of Biomechanics*, 40(13):3006–3012, 2007.

[58] C. W. Hoge, D. McGurk, J. L. Thomas, A. L. Cox, C. C. Engel, and C. A. Castro. Mild traumatic brain injury in U.S. soldiers returning from Iraq. *New England Journal of Medicine*, 358:453–463, 2008.

[59] T.J. Horgan and M.D. Gilchrist. The creation of three-dimensional finite element models for simulating head impact biomechanics. *International Journal of Crashworthiness*, 8(4):353–366, 2003.

[60] T.J. Horgan and M.D. Gilchrist. Influence of FE model variability in predicting brain motion and intracranial pressure changes in head impact simulations. *International Journal of Crashworthiness*, 9(4):401–418, 2004.

[61] J.F. Glenn. Summary of Meeting Proceedings from the International State-of-the-Science Meeting on Non-Impact, Blast-Induced Mild Traumatic Brain Injury. Technical report, Department of Defense, 2012.

[62] K. Kato, M. Fujimura, A. Nakagawa, A. Saito, T. Ohki, K. Takayama, and T. Tominaga. Pressure-dependent effect of shock waves on rat brain: Induction of neuronal apoptosis mediated by a caspase-dependent pathway. *Journal of Neurosurgery*, 106(4):667–676, 2007.

[63] J.E. Kennedy, M.S. Jaffee, G.A. Leskin, J.W. Stokes, F.O. Leal, and P.J. Fitzpatric. Posttraumatic stress disorder and posttraumatic stress disorder-like symptoms and mild traumatic brain injury. *Journal of Rehabilitation Research and Development*, 44(7):895–920, 2007.

[64] S. Kleiven and W.N. Hardy. Correlation of an FE model of the human head with local brain motion – consequences for injury prediction. *Stapp Car Crash Journal*, 46:123–144, 2002.

[65] S. Kleiven and H. von Holst. Consequences of head size following trauma to the human head. *Journal of Biomechanics*, 35(2):153–160, 2002.

[66] R.H. Kraft, P.J. McKee, A.M. Dagro, and S.T. Grafton. Combining the finite element method with structural connectome-based analysis for modeling neurotrauma: Connectome neurotrauma mechanics. *PLoS Computational Biology*, 8:e1002619, 2012.

[67] M.F. Kraus, T. Susmaras, B.P. Caughlin, C.J. Walker, J.A. Sweeney, and D.M. Little. White matter integrity and cognition in chronic traumatic brain injury: A diffusion tensor imaging study. *Brain*, 130(10):2508–2519, 2007.

[68] R. Kuehn, P.F. Simard, I. Driscoll, K. Keledjian, S. Ivanova, C. Tosun, A. Williams, G. Bochicchio, V. Gerzanich, and J.M. Simard. Rodent model of direct cranial blast injury. *Journal of Neurotrauma*, 28:2155–69, 2011.

[69] R.T. Lange, S. Pancholi, T.A. Brickell, S. Sakura, A. Bhagwat, V. Merritt, and L.M. French. Neuropsychological outcome from blast versus non-blast: Mild

traumatic brain injury in U.S. military service members. *J Int Neuropsychol Soc*, 18(3):595–605, 2012.

[70] L.Y. Leung, P.J. VandeVord, A.L. Dal Cegnio, C. Bir, K.H. Yang, and A.I. King. Blast related neurotrauma: A review of cellular injury. *Molecular and cellular biomechanics*, 5(3):155–168, 2008.

[71] H.S. Levin, E. Wilde, M. Troyanskaya, N.J. Petersen, R. Scheibel, M. Newsome, M. Radaideh, T. Wu, R. Yallampalli, Z. Chu, and X. Li. Diffusion tensor imaging of mild to moderate blast-related traumatic brain injury and its sequelae. *Journal of Neurotrauma*, 27(4):683–94, 2010.

[72] A. Lew, R. Radovitzky, and M. Ortiz. An artificial-viscosity method for the lagrangian analysis of shocks in solids with strength on unstructured, arbitrary-order tetrahedral meshes. *Journal of Computer-Aided Materials Design*, 8(2-3):213–231, 2001.

[73] G. Ling, F. Bandak, R. Armonda, G. Grant, and J. Ecklund. Explosive blast neurotrauma. *Journal of Neurotrauma*, 28:815–825, 2009.

[74] P. Lockhart, D. Cronin, K. Williams, and S. Ouellet. Investigation of head response to loading. *Journal of Trauma*, 70(2):E29–36, 2011.

[75] J.B. Long, T.L. Bentley, K.A. Wessner, C. Cerone, S. Sweeney, and R.A. Bauman. Blast overpressure in rats: Recreating a battlefield injury in the laboratory. *Journal of Neurotrauma*, 26(6):827–840, 2009.

[76] J. Lu, K.C. Ng, G. Ling, J. Wu, D.J.F. Poon, M. Kan, M.H. Tan, Y.J. Wu, P. Li, S. Moochhala, E. Yap, L.K.H. Lee, M. Tao, I.B. Yeh, D.M.B. Sergio, F. Chua, S.D. Kumar, and E.A. Ling. Effect of blast exposure on the brain structure and cognition in macaca fascilcularis. *Journal of Neurotrauma*, 29(7):1434–54, 2011.

[77] C.L. MacDonald, A.M. Johnson, D. Cooper, E.C. Nelson, N.J. Werner, J.S. Shimony, A.Z. Snyder, M.E. Raichle, J.R. Witherow, R. Fang, S.F. FLaherty, and D.L. Brody. Detection of blast-related traumatic brain injury in U.S. military personnel. *New England Journal of Medicine*, 364(22):2091–2100, 2011.

[78] A.J. MacGregor, R.A. Shaffer, A.L. Dougherty, M.R. Galarneau, R. Raman, D.G. Baker, S.P. Lindsay, B.A. Golomb, and K.S. Corson. Prevalence and psychological correlates of traumatic brain injury in Operation Iraqi Freedom. *J Head Trauma Rehabil*, 25(1):1–8, 2010.

[79] D.E. Mager, S. Woo, and W.J. Jusko. Scaling pharmacodynamics from in vitro and preclinical animal studies to humans. *Drug Metabolism and Pharmacokinetics*, 24:16–24, 2009.

[80] J. Magnuson, F. Leonessa, and G.S.F. Ling. Neuropathology of explosive blast traumatic brain injury. *Curr Neurol Neurosci Rep*, 12(5):570–579, 2012.

[81] H.A. Mansy, J.R. Grahe, and R.H. Sandler. Elastic properties of synthetic materials for soft tissue modeling. *Phys. Med. Biol.*, 53:2115–30, 2008.

[82] MatWeb. Material Property Data. Online: http://www.matweb.com, 2012.

[83] T. McMahon. Size and shape in biology. *Science*, 179(4079):1201–1204, 1973.

[84] M.A. Meyers. *Dynamic behavior of materials*. Wiley Interscience, 1994.

[85] Mild Traumatic Brain Injury Committee of the Head Injury Interdisciplinary Special Interest Group of the American Congress of Rehabilitation Medicine. The definition of traumatic brain injury. *Journal of Head Trauma and Rehabilitation*, 8(3):86–87, 1993.

[86] S.M. Moochhala, S. Md, J. Lu, C.-H. Teng, and C. Greengrass. Neuroprotective role of aminoguanidine in behavioral changes after blast injury. *The Journal of Trauma: Injury, Infection, and Critical Care*, 56(2):393–403, 2004.

[87] D. F. Moore, A. Jerusalem, M. Nyein, L. Noels, M. S. Jaffee, and R. Radovitzky. Computational biology, modeling of primary blast effect on the central nervous system. *NeuroImage*, 47:T10–T20, 2009.

[88] W.C. Moss, M.J. King, and E.G. Blackman. Skull flexure from blast waves: A mechanism for brain injury with implications for helmet designs. *The Journal of the Acoustical Society of America*, 125(4):2650–2667, 2009.

[89] C.K. Murray, J.C. Reynolds, J.M. Schroeder, M.B. Harrison, O.M. Evans, and D.R. Hospenthal. Spectrum of care provided at an echelon II medical unit during Operation Iraqi Freedom. *Military Medicine*, 170:516, 2005.

[90] D.E. Nampiaparampil. Prevalence of chronic pain after traumatic brain injury: A systematic review. *Journal of the American Medical Association*, 300(6):711–719, 2009.

[91] N.W. Nelson, J.B. Hoelzle, B.M. Doane, K.A. McGuire, A.G. Ferrier-Auerbach, M.J. Charlesworth, G.J. Lamberty, M.A. Polusny, P.A. Arbisi, and S.R. Sponeheim. Neuropsychological outcomes of U.S. veterans with report of remote blast-related concussion and current psychopathology. *Journal of the International Neuropsychological Society*, 18(5):845–855, 2012.

[92] S.J. Neuhaus, P.F. Sharwood, and J.V. Rosenfeld. Terrorism and blast explosions: Lessons for the Australian surgical community. *ANZ Journal of Surgery*, 76(7):637–644, 2006.

[93] T. Nishimoto and S. Murakami. Relation between diffuse axonal injury and internal head structures on blunt impact. *Journal of Biomechanical Engineering – Transactions of the ASME*, 120(1):140–147, 1998.

[94] M.K. Nyein. Finite element modeling of blast-related traumatic brain injury. Master's thesis, Massachusetts Institute of Technology, 2010.

[95] M.K. Nyein, A.M. Jason, L. Yu, C.M. Pita, J.D. Joannopoulos, D.F. Moore, and R.A. Radovitzky. In silico investigation of intracranial blast mitigation with relevance to military traumatic brain injury. *Proceedings of the National Academy of Sciences*, 107:20703, 2010.

[96] D.E. Okhotsimskii, I.A. Kondrasheva, Z.P. Vlasova, and R.K. Kozakova. Calculation of a point explosion taking into account counter pressure. *Tr. Mat. Inst. Steklova*, 50:1–65, 1957.

[97] S. Okie. Traumatic brain injury in the war zone. *New England Journal of Medicine*, 352(20):2043–2047, 2005.

[98] E. Park, J.D. Bell, and A.J. Baker. Traumatic brain injury: Can the consequences be stopped? *Canadian Medical Association Journal*, 178(9):1163–1170, 2008.

[99] M.R. Patterson. A mass transfer explanation of metabolic scaling relations in some aquatic invertebrates and algae. *Science*, 255(5050):1421–3, 1992.

[100] E.R. Peskind, E.C. Petrie, D.J. Cross, K. Pagulayan, and K. McCraw. Cerebrocerebellar hypometabolism associated with repeated blast exposure mild traumatic brain injury in 12 Iraq War veterans with persistent post-concussive symptoms. *NeuroImage*, 54(Supp):576–82, 2011.

[101] J.T. Povlishock and D.I. Katz. Update of neuropathology and neurological recovery after traumatic brain injury. *Journal of Head Trauma Rehabilitation*, 20(1):76–94, 2005.

[102] T.P. Prevost, A. Balakrishnan, S. Suresh, and S. Socrate. Biomechanics of brain tissue. *Acta Biomaterialia*, 7:83–95, 2011.

[103] T.P. Prevost, G. Jin, M.A. de Moya, H.B. Alam, S. Suresh, and S. Socrate. Dynamic mechanical response of brain tissue in indentation in vivo, in situ, and in vitro. *Acta Biomaterialia*, 7, 2011.

[104] A. Przekwas, X.G. Tan, V. Harrand, D. Reeves, Z.J. Chen, and K. Sedberry. Integrated experimental and computational framework for the development and validation of blast wave brain biomechanics and helmet protection. In *HFM-207: A Survey of Blast Injury Across the Full Landscape of Military Science*, pages 34–1 – 33–20, 2011.

[105] P.B. Pun, E.M. Kan, A. Salim, Z. Li, K.C. Ng, S.M. Moochhala, E.-A. Ling, M.H. Tan, and J. Lu. Low level primary blast injury in rodent brain. *Frontiers in Neurology*, 2, 2011.

[106] K. Rafaels, C.R. Bass, R.S. Salzar, M.B. Panzer, W. Woods, S. Feldman, T. Cummings, and B. Capehart. Survival risk assessment for primary blast exposures to the head. *Journal of Neurotrauma*, 28:2319–2328, 2011.

[107] K.A. Rafaels, C.R. Bass, M.P. Panzer, and R.S.Salzar. Pulmonary injury risk assessment for long-duration blasts: A meta-analysis. *The Journal of Trauma*, 69:368–374, 2010.

[108] V. Rao and C. Lyketsos. Neuropsychiatric sequelae of traumatic brain injury. *Psychosomatics*, 41(2):95–103, 2000.

[109] J.-S. Raul, D. Baumgartner, R. Willinger, and B. Ludes. Finite element modelling of human head injuries caused by a fall. *International Journal of Legal Medicine*, 120(4):212–218, 2006.

[110] M. Risling, S. Plantman, M. Angeria, E. Rostami, B.-M. Bellander, M. Kirkegaard, U. Arborelius, and J. Davidsson. Mechanism of blast induced brain injuries, experimental studies in rats. *NeuroImage*, 54(Suppl):S89–S97, 2011.

[111] J.C. Roberts, T.P. Harrigan, E.E. Ward, T.M. Taylor, M.S. Annett, and A.C. Merkle. Human head-neck computational model for assessing blast injury. *Journal of Biomechanics*, 2012.

[112] J.S. Ruan, T. Khalil, and A.I. King. Dynamic response of the human head to impact by three-dimensional finite element analysis. *Journal of Biomechanical Engineering*, 116(1):44–50, 1994.

[113] V. Rubovitch, M. Ten-Bosch, O. Zohar, C.R. Harrison, C. Tempel-Brami, E. Stein, B.J. Hoffer, C.D. Balaban, S. Schreiber, W.-T. Chiu, and C.G. Pick. A mouse model of blast-induced mild traumatic brain injury. *Experimental Neurology*, 232:280–9, 2011.

[114] R.L. Ruff, S.S. Ruff, and X.-F. Wang. Headaches among Operation Iraqi Freedom / Operation Enduring Freedom veterans with mild traumatic brain injury associated with exposures to explosions. *Journal of Rehabilitation Research and Development*, 45(7):941–952, 2008.

[115] K.E. Saatman, A.-C. Duhaime, R. Bullock, A.I.R. Maas, A. Valadka, and G.T. Manley. Classification of traumatic brain injury for targeted therapies. *Journal of Neurotrauma*, 25(7):719–738, 2008.

[116] A.I. Schneiderman, E.R. Braver, and H.K. Kang. Understanding sequelae of injury mechanisms and mild traumatic brain injury incurred during the conflicts in Iraq and Afghanistan: Persistent postconcussive symptoms and posttraumatic stress disorder. *American Journal of Epidemiology*, 167(12):1446–1452, 2008.

[117] S. Sharma and L. Zhang. Prediction of intracranial responses from blast induced neurotrauma using a validated finite element model of human head. In *Ohio State University Injury Biomechanics Symposium*, 2011.

[118] J.K. Shridharani, G.W. Wood, M.B. Panzer, B.P. Capeheart, M.K. Nyein, R.A. Radovitzky, and C.R. Bass. Porcine head response to blast. *Frontiers in Neurology*, 3:1–12, 2012.

[119] A. Suneson, H. Axelsson, H. Hjelmqvist, A. Medin, and J.K.E. Persson. Physiological changes in pigs exposed to a blast wave from a detonating high-explosive charge. *Military Medicine*, 165(2):119–126, 2000.

[120] S.I. Svetlov, S.F. Larner, D.R. Kirk, J. Atkinson, R.L. Hayes, and K.K.W. Wang. Biomarkers of blast-induced neurotrauma profiling molecular and cellular mechanisms of blast brain injury. *Journal of Neurotrauma*, 26(6):913–921, 2009.

[121] K.H. Taber, D.L. Warden, and R.A. Hurley. Blast-related traumatic brain injury: What is known? *Journal of Neuropsychiatry and Clinical Neuroscience*, 18:141–145, 2006.

[122] T. Tanielian. *Invisible Wounds of War: Psychological and Cognitive Injuries, Their Consequences, and Services to Assist Recovery.* RAND Corporation, Center for Military Health Policy Research, Santa Monica, CA, 2008.

[123] P.A. Taylor and C.C. Ford. Simulation of blast-induced early-time intracranial wave physics leading to traumatic brain injury. *Journal of Biomechanical Engineering*, 131(6):061007, 2009.

[124] J. Teland, A. Hamberger, M. Huseby, A. Saljo, and E. Svinsas. Numerical simulation of mechanisms of blast-induced traumatic brain injury. In *Proceedings of the 159th Meeting of the Acoustical Society of America*, 2010.

[125] H. Terrio, L.A. Brenner, B.J. Ivins, J.M. Cho, K. Helmick, K. Schwab, K. Scally, R. Bretthauer, and D. Warden. Traumatic brain injury screening: Preliminary findings in a U.S. Army brigade combat team. *Journal of Head Trauma Rehabilitation*, 24:14–23, 2009.

[126] P. Thompson. *Compressible-Fluid Dynamics.* McGraw-Hill, New York, 1972.

[127] D.J. Thurman, C. Alverson, K.A. Dunn, J. Guerrero, and J. Sniezek. Traumatic brain injury in the United States: A public health perspective. *Journal of Head Trauma Rehabilitation*, 14(6):602–615, 1999.

[128] D.J. Thurman, J.E. Sniezek, and D. Johnson. *Guidelines for Surveillance of Central Nervous System Injury.* Centers for Disease Control and Prevention, Atlanta, 1995.

[129] U.S. Government Accountability Office. Mild traumatic brain injury screening and evaluation implemented for OEF/OIF veterans, but challenges remain, 2008.

[130] R.D. Vanderploeg, H.G. Belanger, R.D. Horner, A.M. Spehar, G. Powell-Cope, S.L. Luther, and S.G. Scott. Health outcomes associated with military deployment: Mild traumatic brain injury, blast, trauma, and combat associations in the Florida National Guard. *Arch Phys Med Rehabil*, 93(11):1887–1895, 2012.

[131] J.M. Varas, M. Philippens, S.R. Meijer, A.C. van den Berg, P.C. Sibma, J.L.M.J. van Bree, and D.V.W.M. de Vries. Physics of IED blast shock tube simulations for mTBI research. *Frontiers in Neurology*, 2, 2011.

[132] T. Veenith, S.S.H. Goon, and R.M. Burnstein. Molecular mechanisms of traumatic brain injury: The missing link in management. *World Journal of Emergency Surgery*, 4:7, 2009.

[133] K.W. Wang. *Calpain and caspase in ischemic and traumatic brain injury*, chapter 8, pages 181–200. CRC Press, 2002.

[134] D. Warden. Military TBI during the Iraq and Afghanistan wars. *Journal of Head Trauma Rehabilitation*, 21:398–402, 2006.

[135] D.L. Warden, L.M Ryan, K. Schwab, L. French, W. Lu, W. Lux, G. Ling, and J. Ecklund. War neurotrauma: the Defense and Veterans Brain Injury Center(DVBIC) experience at Walter Reed Army Medical Center (WRAMC). *Journal of Neurotrauma*, 22:1178, 2005.

[136] C. Werner and K. Engelhard. Pathophysiology of traumatic brain injury. *British Journal of Anaesthesia*, 99(1):4–9, 2007.

[137] G.B. West, J.H. Brown, and B.J. Enquist. A general model for the origin of allometric scaling laws in biology. *Science*, 276(5309):122–6, 1997.

[138] R. Willinger and D. Baumgartner. Human head tolerance limits to specific injury mechanisms. *International Journal of Crashworthiness*, 8(6):605–617, 2003.

[139] B.E. Wojcik, C.R. Stein, K. Bagg, R.J. Humphrey, and J. Orosco. Traumatic brain injury hospitalizations of U.S. army soldiers deployed to Afghanistan and Iraq. *Am J Prev Med*, 38(18):5108–5116, 2010.

[140] Y.B. Zel'dovich and Y.P. Raizer. *Physics of shock waves and high-temperature hydrodynamic phenomena*, volume 2. Academic press, New York and London, 1967.

[141] L. Zhang, R. Makwana, and S. Sharma. Comparison of the head response in blast insult with and without combat helmet. In *HFM-207: A Survey of Blast Injury Across the Full Landscape of Military Science*, pages 33–1 – 33–18, 2011.

[142] L. Zhang, K.H. Yang, R. Dwarampudi, K. Omori, T. Li, K. Chang, W. Hardy, T. Khalil, and A.I. King. Recent advances in brain injury research: A new human head model development and validation. *Stapp Car Crash Journal*, 45:369–394, 2001.

[143] L. Zhang, K.H. Yang, and A.I. King. Comparison of brain responses between frontal and lateral impact by finite element modeling. *Journal of Neurotrauma*, 18:21–30, 2001.

[144] F. Zhu, H. Mao, A. Dal Cengio Leonardi, C. Wagner, C. Chou, X. Jin, C. Bir, P. VandeVord, K.H. Yang, and A.I. King. Development of an FE model of the rat head subjected to air shock loading. *Stapp Car Crash Journal*, 54:211–55, 2010.

[145] F. Zhu, P. Skelton, C.C. Chou, H. Mao, K.H. Yang, and A.I. King. Biomechanical responses of a pig head under blast loading: A computational simulation. *Int. J. Numer. Meth. Biomed. Engng.*, 2012.

[146] F. Zhu, C. Wagner, A.D.C. Leonardi, X. Jin, P. VandeVord, C. Chou, K.H. Yang, and A.I. King. Using a gel/plastic surrogate to study the biomechanical response of the head under air shock loading: A combined experimental and numerical investigation. *Biomech Model Mechanobiol*, 11:341–353, 2012.